A STUDY OF THE SINTERING BEHAVIOUR OF Ni-Ti POWDER COMPACTS USING DIFFERENTIAL SCANNING CALORIMETRY

by

Mark A. Whitney

A thesis
presented to the University of Waterloo
in fulfilment of the
thesis requirement for the degree of
Master of Applied Science
in
Mechanical Engineering

Waterloo, Ontario, Canada, 2007

Author's Declaration

I hereby declare that I am the sole author of this thesis. This is a true copy of the thesis, including any required final revisions, as accepted by my examiners.

I understand that my thesis may be made electronically available to the public.

Abstract

A primary purpose of the present work was to develop an experimental technique using Differential Scanning Calorimetry (DSC) capable of elucidating phase formation during sintering of a 50 atomic percent Ni and 50 atomic percent Ti powder compact in order to increase the understanding of the sintering mechanisms that take place during solid state and reactive sintering. Using a variety of Nickel and Titanium powder sizes, effects due to powder size, peak temperature and hold time were studied *in situ* using DSC, which allowed for a number of qualitative and quantitative relationships to be developed.

In studying the eutectoid decomposition of β-Ti using DSC, a simple model was developed (Eq. 4-7) to relate the measured enthalpy of this reaction to the area fraction observed microstructurally. This allowed for the determination of the standard enthalpy for the β-Ti eutectoid decomposition, which was found to be ΔH_f = 64.8 J/g. This value, coupled with the measured eutectoid enthalpy, allowed for the determination of the weight fraction of β-Ti present as a function of hold time at 900°C. It was found that the β-Ti removal followed a two-stage parabolic decay. The rate constant for stage I was found to be $k_I = -0.0347\ f_\beta / (mins)^{1/2}$ and that for stage II, $k_{II} = -0.0123\ f_\beta / (mins)^{1/2}$.

A relationship between the enthalpy observed for the combustion reaction versus the fraction of β-Ti present at the time of combustion was also developed (Eq. 4-15). This represents the first published evidence that combustion actually depends on the β-Ti content, which in turn precipitates a melting event significant enough to initiate combustion.

Acknowledgements

During my Undergraduate degree in Chemical Engineering, I was given the choice during my 3A school term to choose between one of two single course options: Biotechnology or Introduction to Materials Science. Can you guess what I chose? Had I known what was in store for me during the subsequent coop work term, I would have naturally chosen Introduction to Materials Science. Unfortunately, foresight is not a gift I possess; and as is likely apparent now, I chose Biotechnology.

That aforementioned work term brought me to the Mechanical Engineering department at the University of Waterloo. It is safe to say that my knowledge of Materials Science was in its infancy when beginning that work term (which is on par with some of my classmates that had chosen the Materials option). By the end of that work term, I couldn't tell you what a Bravais lattice was if you paid me, but an interest was sparked inside me that has grown, and continues to grow, to this very day. I have both Professor Stephen Corbin and Jeffrey McIsaac to thank for that. They opened a door to an area of research that is as complex, as challenging, as diverse, and exciting as one could only hope for.

Two URA's, another coop work term, and a 4th year project later, and I was hooked on Materials Science. After my BASc, the natural choice was to pursue a MASc in the Mechanical Engineering department. The choice of which supervisor I wanted to work for was made with similar ease. There is no doubt in my mind, that most of what I have learned in this field can be attributed to the guidance, mentorship and friendship of Professor Corbin. For that I am truly grateful.

As is customary it seems, I must thank those of Professor Corbin's graduate students that have come before me. This, in no way, is meant to diminish the contributions of those students to my graduate experience (of which there are many). The mere fact that each of these graduate students has acknowledged the contributions of previous ones is meant to emphasize what a tremendous judge of character Professor Corbin possesses. He fosters a research group which is highly interactive (whether socially or academically), and promotes both teaching and learning amongst his graduate students. Thus, the younger students not only learn from Professor Corbin, but also from those students their senior. For me specifically, those within our research group from whom I've learned so much are (in no specific order…OK, maybe alphabetically according to first name): Dennis Turriff, Douglas Jeffrey McIsaac, Ernest Ansah-Sam, Michael Kuntz, Ryan Clemmer, and Troy D'Hondt. All may not have contributed directly to my research topic, but all have contributed immensely to my knowledge of Materials Science principles and practices, as well as my graduate experience on the whole. I thank them for their friendship, their guidance and their ability to put up with somebody who evidently misspelt meCh on their undergraduate application (an accusation originating from students I have TA'd).

I would like to thank my co-supervisor Professor Rob Gorbet for his guidance and support throughout my MASc, and for exposing me to areas of shape memory alloy

research I was at first unfamiliar with, but came to appreciate. This helped me to grasp the “big picture”, and understand the larger scope of which my research topic belonged. I would also like to thank Professor Gorbet for playing video games while I worked on a presentation the night before the CanSmart conference in which I was giving said presentation. ☺

I am also grateful to Professor Ehsan Toyserkani and Professor Shahrzad Esmaeli for their comments, criticisms and insights relating to my MASc thesis. It is very much appreciated.

I would like to acknowledge the generous financial and resource support of Emerging Materials Knowledge (EMK), Materials Manufacturing Ontario (MMO), the National Science and Engineering Research Council (NSERC) and the International Nickel Company (INCO).

I can safely say there were times during my MASc I wanted nothing to do with my studies, as they were understandably furthest from my mind. Thankfully, my family, friends and colleagues were there to keep me headstrong and provide emotional support during those trying times. For that I am eternally grateful.

Lastly, and most importantly, I would like to my loving wife for her support. It is nigh impossible to put into words how much you have helped me through school, work, and life since I met you. You pretend I am right on occasion; you love me when I am wrong; you make me strive to become a better person, and you give my life meaning and purpose.

Table of Contents

List of Figures

List of Tables

1 Introduction

The Nickel and Titanium binary alloy system (Figure 1-1) is of interest partly because of its intermetallics, specifically the near equiatomic TiNi intermetallic. The TiNi intermetallic belongs to a group of functional materials known as shape memory alloys (SMA).

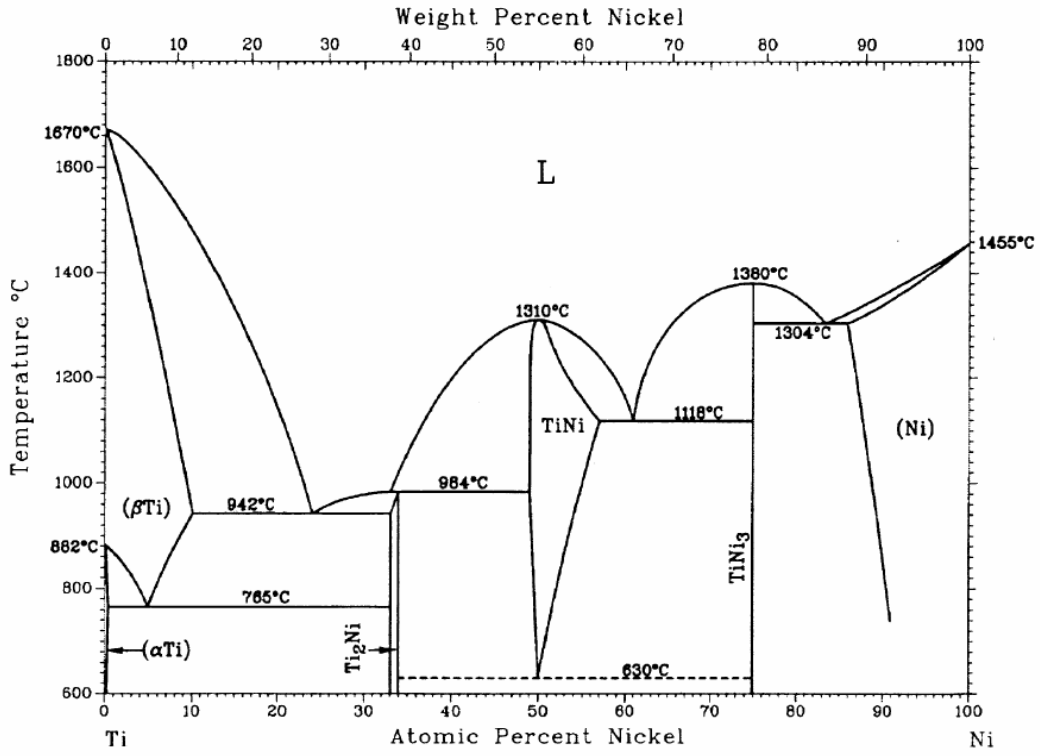

Figure 1-1: Ni/Ti binary alloy phase diagram [1]

These nickel-titanium SMAs were first developed in 1962-1963 by the Naval Ordnance Laboratory and commercialized under the trade name Nitinol. Using the "Web of Science" research database from ISI Web of Knowledge, a citation search of the relevant publications pertaining to the TiNi intermetallic, dating back to its discovery, indicates that experimental research in this area has grown at a seemingly exponential rate during the last five decades (Figure 1-2).

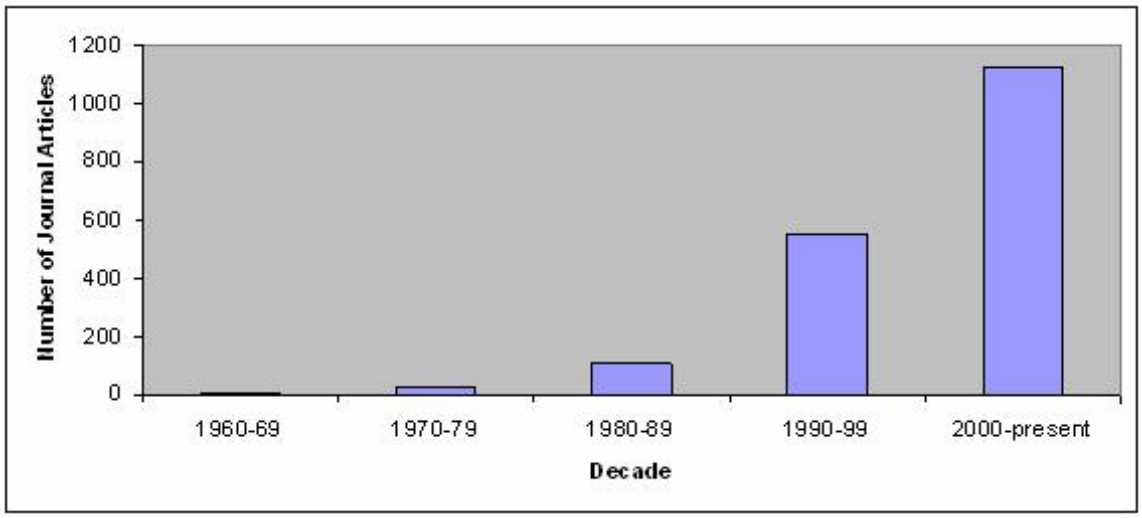

Figure 1-2: Research journal articles published on the subject of TiNi

Shape memory alloys are materials that can display both a shape memory effect (SME) and pseudo-elasticity (PE) depending on their temperature in service. The SME can occur as a one-way or two-way transformation, the latter of which requires training of the SMA. Typically, loading is required to induce deformation of the SMA. This loading induces a de-twinning of the low-temperature monoclinic B19' twinned martensite. Heating of the SMA (typically in the form of Joule heating) can cause a crystallographic change from de-twinned martensite to a cubic B2 austenite phase (CsCl type structure), which can recover some of the deformation of the SMA, and if the load is removed, can return the SMA to its original low-temperature shape. Figures 1-3 and 1-4 show a schematic representation of the SME using an SMA wire, and the corresponding crystallographic changes within the SMA, respectively.

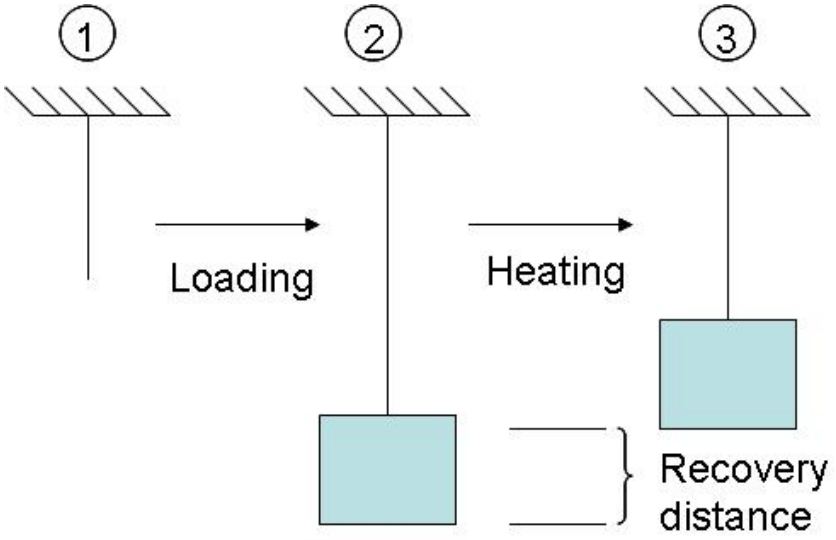

Figure 1-3: Schematic representing functional shape change of an SMA wire

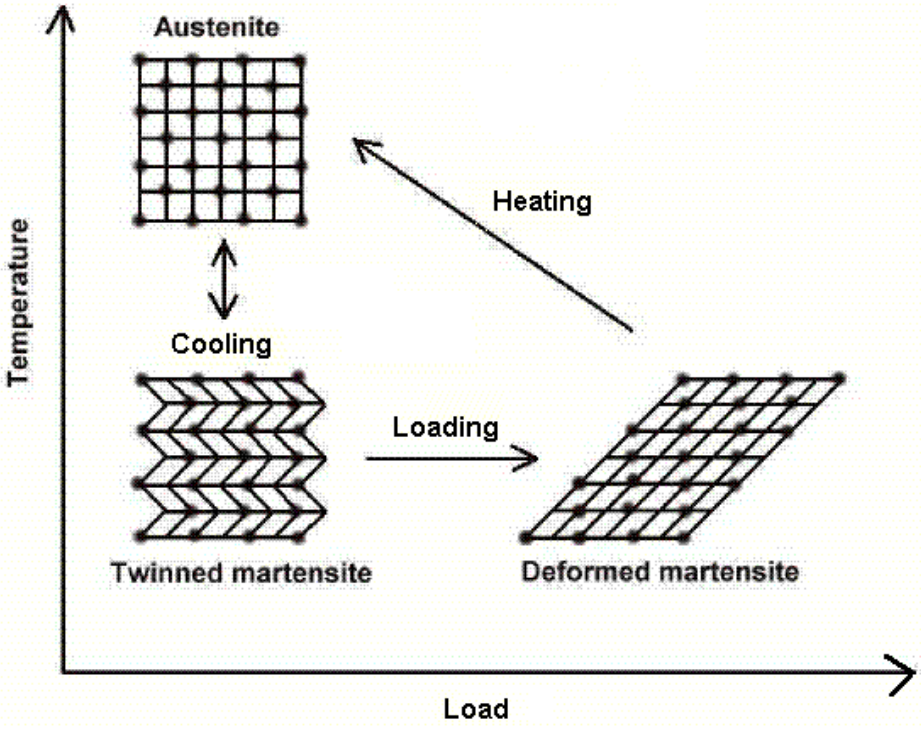

Figure 1-4: Schematic of the associated crystallographic changes in the shape memory effect of TiNi [2]

During cooling of a TiNi SMA, the transformation from austenite to martensite can occur in one or two stages. During a two-tage martensitic transformation, cubic B2 austenite transforms to a metastable R-phase structure differing only slightly from B2 by

rhombohedral distortion, with a subsequent transformation from the R-phase to B19' martensite. During one-stage martensitic transformation, cubic B2 austenite transforms directly to monoclinic B19' martensite

As a result of the wide compositional range over which the TiNi intermetallic can exist, it is possible to tailor the temperature at which the SME is displayed (in the range of -50^{o}C to 150^{o}C) by controlling the bulk composition (Figure 1-5). As an added benefit, TiNi SMAs can display the SME close to room temperature, which makes them particularly attractive from a commercial standpoint. At present, there are a number of current and potential medical and industrial applications that take advantage of both the shape memory effect of TiNi (vascular stents, arthroscopic cameras, micro-actuators, active dampeners) and its pseudo-elasticity (surgical instruments, porous bone implants, dental arch-wires, eyeglass wireframes, and passive dampeners) [3-5].

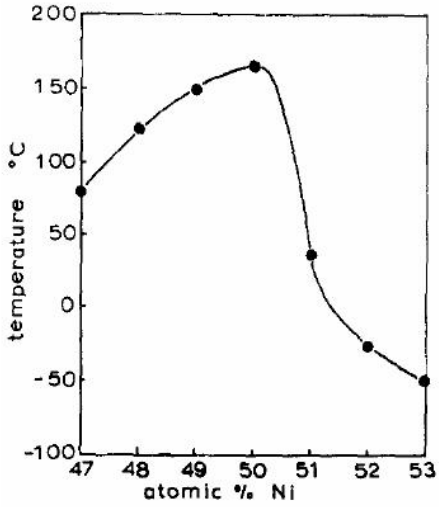

Figure 1-5: Temperature dependence of the SME in TiNi on composition **[6]**

1.1 Current TiNi Production

The current production route for TiNi intermetallic is very costly, and to tailor the SME to a specific temperature (or range of temperatures) requires a high degree of compositional control. Currently, production methods such as vacuum induction melting (VIM) and vacuum arc re-melting (VAR) are used to manufacture TiNi intermetallic in the form of ingots, and subsequent forming methods limit the commercial availability of TiNi to wire and sheet stock. Due to its pseudo-elasticity, TiNi is extremely wear resistant, and as a result, difficult to machine to a final desired shape. In addition, the high temperatures associated with the VIM and VAR production techniques further increase production costs (have to heat past the melting points of both Ni and Ti). All of the negative connotations associated with traditional fabrication of TiNi (high cost and machining difficulty) seem to point to Powder Metallurgy (PM) as a potential solution to the current limitations of TiNi production. Using PM to manufacture TiNi through a sintering route allows one to attain a desired bulk composition more readily, without the need for multiple re-melts as would be required using the VIM-VAR processes. Additionally, the need for machining would be greatly reduced, as PM fabrication of TiNi can be a near-net shape process. Production costs could further be reduced as no melting of the primary constituents (Ni and Ti) would be required in the formation of TiNi. This would mean that furnace temperatures could be reduced from above the melting point of pure Ti, 1668^{o}C, to temperatures potentially below 1000^{o}C. A decrease in furnace temperature greater than 400-500^{o}C can be quite significant in terms of cost savings, especially when multiple re-melts are not required.

Despite the obvious advantages in producing TiNi intermetallic via a PM route, there are some disadvantages in choosing a sintering route. The reactivity of titanium with oxygen, especially at high temperatures, makes the need for highly pure powders and a completely inert atmosphere essential. The use of high purity Ti powder can be costly, with some varieties costing as much as US $4 per gram [7]. The time required via sintering in the solid state is also a concern in using a PM production route to form TiNi; however the reactive sintering of Ni and Ti has the potential to dramatically reduce this time, and possibly aid in the overall densification of the final sintered microstructure through *in situ* liquid formation.

1.2 Solid State Sintering Fundamentals

Sintering can be thought of as a 'firing' process that is necessary for the bonding of particulate substances such as metals and ceramics. Typically, "…particles to be sintered are smaller than 1 *mm* in size and can possess a wide variety of geometries: spheres, cubes, wires, flakes, discs, snowflakes, or other small solids that flow and pack as a powder" [8]. The sintering process can be divided into two different methods of joining particulate substances: pressureless (excluding the initial compaction pressure required to form the compact) and pressure-assisted sintering. The advantage of pre-sintering compaction, when using ceramic and/or metal powders in the forming process, is that it allows for a near-net shape process. Additionally, a high degree of compositional control over the final product can be achieved. Once powders are formed, they must be bonded together to impart strength and various other physical and mechanical properties to the final part. This bonding is termed sintering, and can take place in the solid state (solid

state sintering), or with the aid of a liquid phase (liquid phase sintering). As particles bond during sintering there are significant changes in the pore structure [8], which is a result of a reduction in free energy through events at an atomistic level. These events can be thought of as the driving forces behind sintering, and can occur through active transport mechanisms. The two classes of mechanisms, surface transport and bulk transport, are comprised of several atomistic mechanisms which contribute to mass flow. The surface transport mechanisms include: surface diffusion, evaporation-condensation, and volume diffusion; whereas bulk transport includes the following mechanisms: grain boundary diffusion, plastic flow, and volume diffusion. Of the two transport mechanisms, only bulk transport can result in shrinkage as the particle centers are brought closer together [8].

Consider the solid state sintering of loose mono-sized spherical powders; the particles initially in point contact (Figure 1-6a). The driving force to sinter is a reduction in the surface energy of the particles, which results from a reduction in the free surface area. This is brought about by inter-particle bridging, also known as *necking* (Figure 1-7).

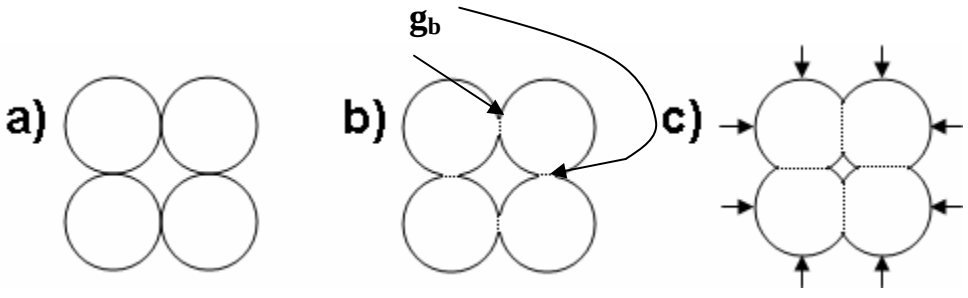

Figure 1-6: Schematic of mono-sized particle sintering showing: a) initial powders in point contact, b) neck growth as a result of surface transport, and c) pore elimination (shrinkage) due to bulk transport.

At early stages of sintering, necking occurs primarily by way of surface diffusion as its corresponding activation energy is typically lower than that of other transport

mechanisms [8]. This surface diffusion results in neck growth, which corresponds to grain boundary growth (Figure 1-6b). As temperature and grain boundary (g_b) area increase, bulk transport contributions to neck growth become important. Once bulk transport begins, densification and pore elimination can occur (Figure 1-6c).

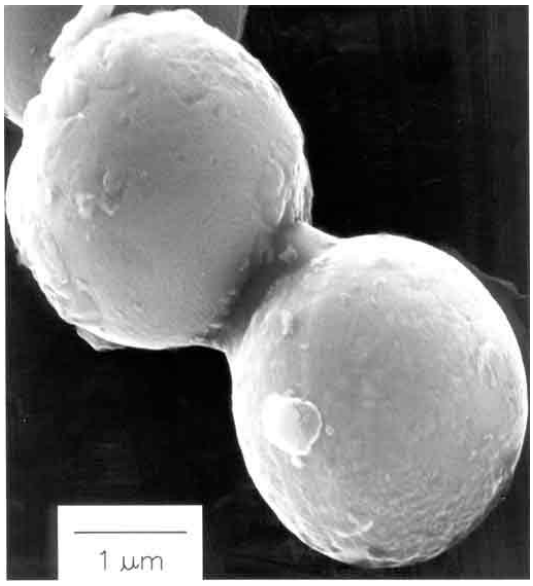

Figure 1-7: Inter-particle bridging (necking) between two Zinc particles **[9]**

The driving force for sintering continues until the free surface energy (γ_{sv}) is balanced by the grain boundary energy (γ_{gb}) as given by [8]:

$$\gamma_{gb} = 2\gamma_{sv}\cos\left(\frac{\phi}{2}\right) \qquad \textbf{(1-1)}$$

where ϕ is the dihedral angle which represents the angle of intersection at the pore and grain boundary interface as seen in Figure 1-8. It should be noted that the dihedral angle ϕ can never reach π radians, the case for a flat pore/surface interface. If it did, Equation (1-1) would predict a grain boundary energy of $\gamma_{gb} = 0$, which is not possible as γ_{gb} has a finite value.

Simple sintering models exist that provide an estimation of the relative rate of neck growth for the sintering of a powder species under any transport mechanism. These result in the following initial-stage growth model for the neck size ratio *X/D* as a function of sintering time under isothermal conditions [8]:

$$\left(\frac{X}{D}\right)^n = \frac{Bt}{D^m} \qquad \textbf{(1-2)}$$

where, as indicated in Figure 1-8, *X* is the neck diameter and *D* is the particle diameter. The variable *t* represents the sintering time, and the values of *B*, *n*, and *m* are material and geometric constants as specified in [8]. The initial stage ends when the necks begin to impinge at an approximate neck size ratio *X/D* of 0.3 [8].

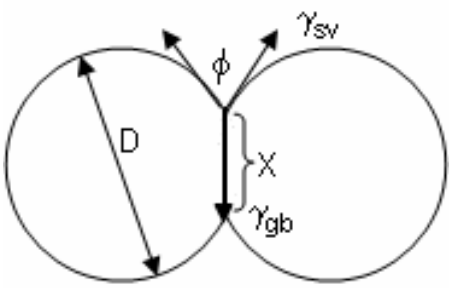

Figure 1-8: Surface and grain boundary energy during neck growth

1.2.1 Effects of Powder Size on Solid State Sintering

From Equation (1-2), it can be shown that there exists a particle size effect on the sintering of powder species, which was first shown by Herring [10]. His work assumed a single transport mechanism operating during sintering, and that the degree of sintering could be measured by the neck size ratio *X/D* [8]. If more than one size of powder is available for sintering, then the sintering time required to reach an equivalent degree of sintering could be represented by:

$$t_2 = t_1\left(\frac{D_2}{D_1}\right)^m \qquad \textbf{(1-3)}$$

which follows from a comparison of Equation (1-2) for differently sized powders. The exponent *m* is a constant dependant on the material transport mechanism [8]. For surface diffusion, which dominates during the initial stages of sintering for which Equation (1-2) was developed, $m = 4$ and a reduction in particle size by half can reduce the sintering time for an equivalent degree of sintering by a factor of 16. This shows that the particle size can have a dramatic effect on the sintering time.

Particle size can also have a dramatic effect on the green density of powder compacts. Consider a bimodal mixture of powders, having two distinctively different sizes designated *S* for small and *L* for large. According to Figure 1-8, a simple rule of mixtures predicts a linear relationship for packing density for the bimodal mixture of powders that falls between the packing density for mixtures containing all small particles (V_S), and all large ones (V_L). In actuality, ideal bimodal powder mixtures have improved packing density relative to the rule of mixtures prediction, as the finer powders will tend to fill the interstitial spaces between the larger particles. There are five different bimodal mixtures represented in Figure 1-9: (i) all small particles, (ii) majority small particles with some dispersed large particles, (iii) maximum packing density mixture, (iv) majority large particles with some small particles in the interstices, and (v) all large particles. The maximum packing density (V^*) possible will occur when the smaller particles fill the voids in between the densely packed larger particles. This will be dependant on the ratio of particle sizes, and the inherent packing density of the two different particles [11].

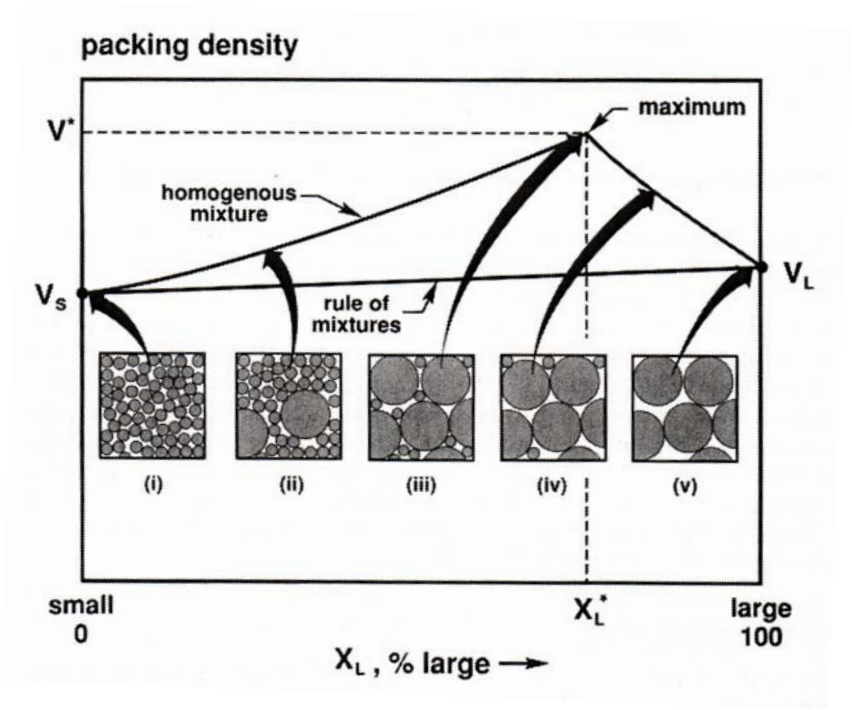

Figure 1-9: Packing density variation with composition for a bimodal mixture **[8]**

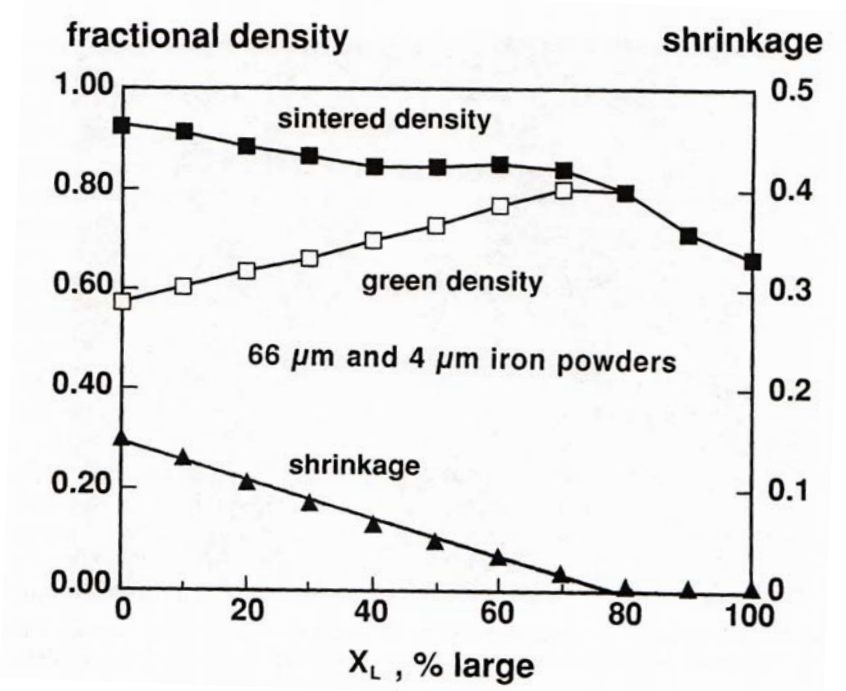

Figure 1-10: Fractional density and shrinkage plots for the sintering of bimodal mixtures of spherical iron powders **[12]**

While the green density of a powder compact improves up to V^* for a bimodal mixture, the sintered density and sintering shrinkage both decline with an increasing content of

large particles (Figure 1-10). The sintered density for a bimodal mixture falls in between that of each powder, while the sintering shrinkage slowly declines with composition until X_L^* is reached, at which point it falls to zero. The sintering shrinkage decreases with increased large particle content because large particles restrain densification by the small particles, causing the small particles to have a negligible effect on the sintering response [8]. This is because the system rigidity from large particle sinter bonds is far greater than the sintering stress [8].

1.3 Sintering of Compositionally Mixed Powders

In the solid state sintering of many compositionally mixed powder systems, the formation of new phases is possible through diffusion controlled reactions. In the Ni-Ti system, these new phases are intermetallic compounds (IMCs) of Ni and Ti, which according to Figure 1-1 are: Ti_2Ni, TiNi and $TiNi_3$. It should be noted that although these IMCs are identified by stoichiometric ratios of Ni and Ti, the IMCs themselves may not be stoichiometric in nature, and may possess a compositional range over which they may exist. For example, the TiNi intermetallic can exist over a compositional range from 49.6 at% to as high as 57 at% Nickel depending on the temperature.

Systems that form new phases as a result of mixing are considered chemically active, and can have a free energy of mixing hundreds of times greater than the surface energies associated with sintering [13]. The free energy of mixing (ΔG_{mix}) is given by the following equation [14]:

$$\Delta G_{mix} = \Delta H_{mix} - T\Delta S_{mix} \qquad \textbf{(1-4)}$$

where (ΔS_{mix}) is the entropy of mixing, T the temperature, and the enthalpy of mixing is defined as [14]:

$$\Delta H_{mix} = \Omega x_A x_B \quad \textbf{(1-5)}$$

The enthalpy of mixing represents the heat required/liberated as atoms of species A and B mix through solid solution alloying and the formation of new phases. The Ω term, known as the solution parameter [14], is a representation of the bond energy between A and B atoms, which statistically, can be expressed by the following four types: A-A, B-B, A-B, and B-A. This results in the following expression for Ω [14]:

$$\Omega = \varepsilon_{AA} + \varepsilon_{BB} - \varepsilon_{AB} - \varepsilon_{BA} \quad \textbf{(1-6)}$$

Since the energy associated with A-B and B-A bonds is the same ($\varepsilon_{AB} = \varepsilon_{BA}$), the solution parameter of Equation (1-6) can further be reduced to [14]:

$$\Omega = \varepsilon_{AA} + \varepsilon_{BB} - 2\varepsilon_{AB} \quad \textbf{(1-7)}$$

Since x_A and x_B of Equation (1-5) represent mass/mole fractions of species A and B, they cannot be negative numbers. Observing Equation (1-7), the solution parameter will take on a positive value when like bonds are favoured (A-A and B-B bonds), and a negative value if unlike bonds are favoured (A-B and B-A). This makes sense as a negative Ω leads to a negative ΔH_{mix}, which means that mixing is both exothermic and thermodynamically favoured.

The more chemically active a system is, the more sintering is controlled by the solubility and chemical reactions of the powders [15]. If the solubility of the mixed powders differs to a great extent, swelling and pore formation may occur [8]. Additionally, density changes of any new phases formed relative to that of the pure reacting species can contribute to swelling and pore formation, resulting in an overall decreased sintered density. Figure 1-11 shows the molar volumes for the intermetallic compounds of the chemically active Ni-Ti system. The dashed line represents the molar volume that would be predicted using Vegard's Law, which assumes a mixture of pure Ni and Ti at the specific composition of each intermetallic. The points for each intermetallic are the actual molar volumes calculated using lattice parameter data [16].

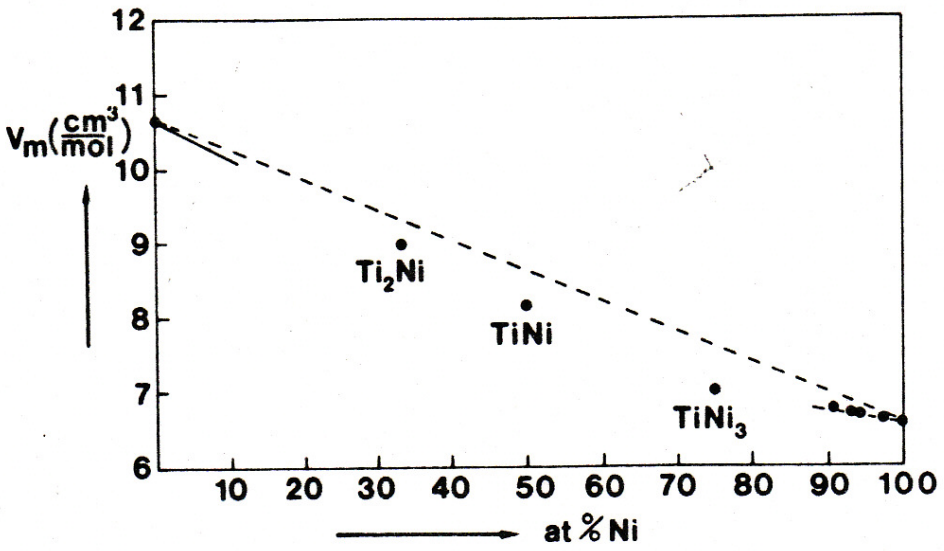

Figure 1-11: Molar volume as a function of composition for the Ni-Ti system **[16]**

These intermetallic phases will tend to form at the surface contacts of the powder species being sintered, and as a result will form a skeletal network of intermetallic (Figure 1-12). Once this network of intermetallic forms, it can act to inhibit further sintering shrinkage by the reacting powders. Since the molar volumes of the intermetallics are less than that predicted by Vegard's law, the densities of these phases will be greater than a simple

mixture of pure Ni and Ti at the same composition. With sintering shrinkage inhibited, the formation of the denser intermetallics can lead to porosity development throughout the microstructure (Figure 1-13).

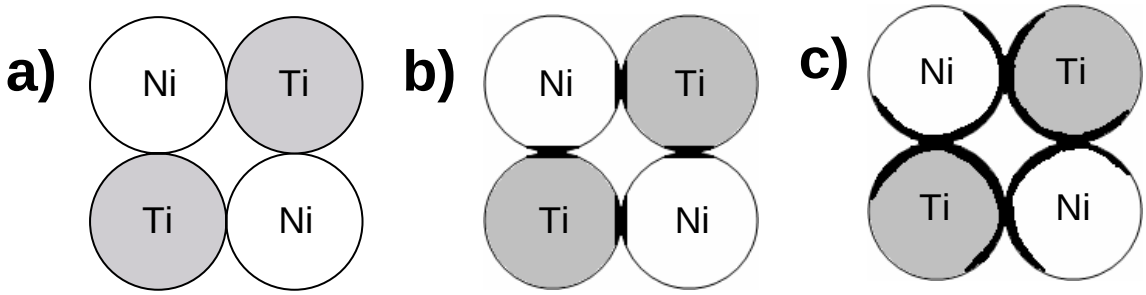

Figure 1-12: Schematic showing sintering mixed Ni/Ti powders: a) initial powders in point contact, b) phase growth at contact points, c) skeletal network formed as a result of intermetallic growth

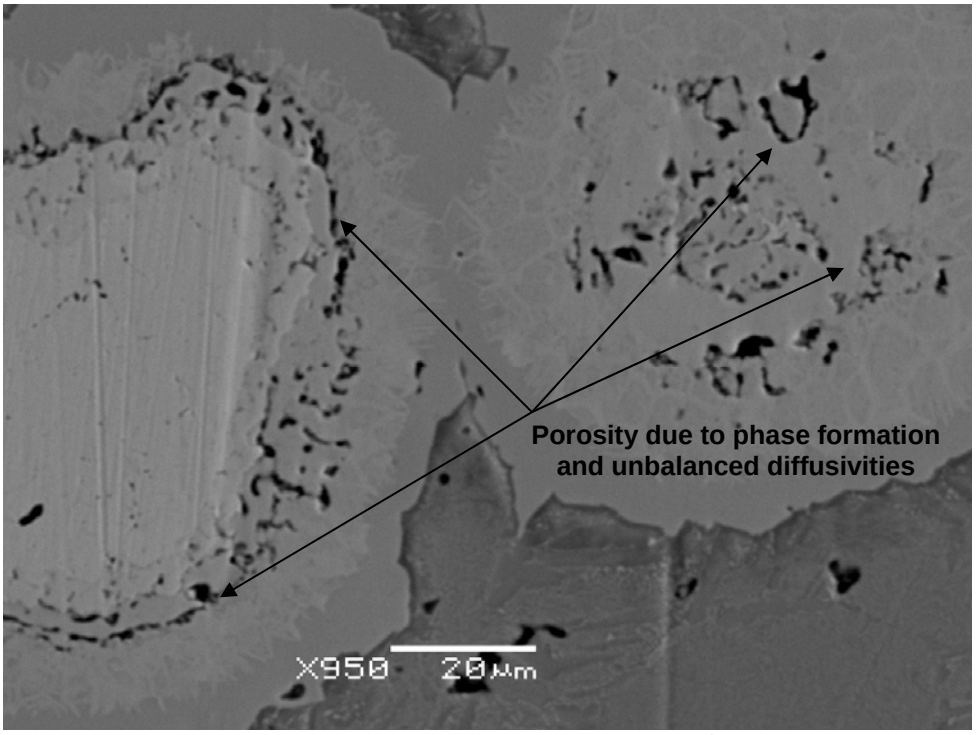

Figure 1-13: SEM backscatter image of a sample heated to 950°C and held for 10 hours

1.4 Reactive Sintering of Compositionally Mixed Powders

In some material systems, the sintering of mixed powders can lead to the formation of intermediate compounds directly, and in a reactive self-sustaining way. Some examples include borides, carbides, nitrides, sulfides, oxides, hydrides, aluminides, and silicides [17-22]. The formation of these intermediate compounds during the reactive sintering of mixed powders typically involves an exothermic reaction that is autocatalytic, which once initiated, proceeds spontaneously without external heat requirement [20]. In other words, these reactions provide the necessary heat to further the reaction throughout the sample. These types of reactions are also known as self-combustion, self-propagating high-temperature synthesis (SHS), gasless combustion, thermal explosion, or reactive sintering [8].

Reactive sintering can be considered a process whereby densification occurs in union with the combustion synthesis process [19, 23]. As a result of the exothermic nature of these types of reactions, the sample may see substantial temperature increases. Such increases in temperature can lead to in situ formation of a liquid phase, which aids in densification for the reactive sintering process [8]. The most important factor to densification during the exothermic reaction is the green compact microstructure [8]. The situation when the powder mixture is inhomogeneous can lead to pockets of liquid formation during reactive synthesis, which flows throughout the surrounding solid leaving behind pores [19]. A homogeneous mixture of the two reacting powder species can minimize this problem.

The extreme case of reactive sintering is characterized by the highly exothermic combustion reaction. The combustion reaction can occur in one of two modes: the thermal explosion (TE) mode of self-propagating high-temperature synthesis (SHS), and the plane wave propagation (PWP) mode. Since the TE mode of combustion synthesis is typically initiated through furnace heating of the reactants, the heating rates to ignition temperature are orders of magnitude lower than for the PWP mode. For a typical TE mode reaction, the rate is in the range of 10 to 500^{o}C/min, while PWP mode can have heating rates as high as 10^{4} to 10^{6} ^{o}C/min [24]. Due to the heating rate limitations of the DSC (accurate to ~40 ^{o}C/min), only the TE mode of SHS will be studied in the present work.

1.5 Sintering Production of TiNi

The fabrication of the Ti-50at%Ni intermetallic compound through sintering of pure Nickel (Ni) and Titanium (Ti) powder mixtures has been the subject of several research investigations, some of which date back over 20 years [25-33]. A number of studies have focused on the production of high density TiNi from sintering elemental powders [32, 34-42]. The sintering methods used to produce TiNi have included normal pressureless sintering in a vacuum or inert Ar gas [25-37, 41-47], sintering under pressure (i.e. hot isostatic pressing or HIPing) [38-40] and metal injection molding (MIM) [48]. A few studies have looked at alternative sintering processes using the application of current [41, 49], the use of reducing additives [50-51] and a two step sintering procedure [35, 52].

More recently an increased interest in the use of TiNi for biomedical applications has led to investigations of porous TiNi [43-47]. The need for high levels of porosity in biomedical areas has also led to an increase in the use of combustion synthesis or self-propagating high-temperature synthesis (SHS) to fabricate porous TiNi [43-45, 47].

References 47, 53, and 54 are examples where the thermal explosion (TE) mode of self-sustaining high-temperature synthesis (SHS) takes place during sintering. TE mode occurs when an exothermic reaction between Ni and Ti to form TiNi is initiated by heating during the sintering process (i.e. typically above 950^{o}C). Other studies represent the plane wave propagation (PWP) mode of SHS [42, 43, 55]. In this approach an exothermic reaction is initiated at one end of the sample using a local heat source such as electric current. This generates a self-propagating high-temperature reaction through the remaining sample. PWP-SHS differs from TE-SHS in that only part of the sample is heated high enough to initiate the exothermic reaction. In many cases PWP samples are also preheated to temperatures in the range of 200 to 500^{o}C prior to the ignition process.

From the literature, the thermal explosion mode of combustion synthesis and solid state sintering to form TiNi can be identified as two distinct processes. Unlike TE-SHS, where a strong exothermic reaction occurs during sintering, in solid state sintering, microstructural evolution is more gradual (diffusion-controlled) with the progressive formation of intermediate phases including Ti_2Ni, TiNi and Ni_3Ti during heating.

Evidence in the literature [32, 33, 36, 37, 46, 47, 53, 54, 56, 57] indicates that the TE-SHS sintering mode results in higher levels of porosity and a higher degree of TiNi

formation. Conversely, solid state sintering can lead to higher densities but lower fractions of TiNi formation. Consequently, obtaining high density, high volume fraction TiNi (without the use of external pressure such as HIPing) remains a challenge. Overcoming this challenge requires a more fundamental understanding of the mechanisms of solid state and reactive (self-combustion) sintering. In particular, despite the importance of phase formation during the sintering of Ni and Ti to form TiNi, reactive sintering is still not very well understood and detailed experimental analysis during sintering has been limited. For example, Yi and Moore [53] state that the ignition temperature for the TiNi synthesis reaction is a constant, intrinsic value of 910^{o}C. Looking at the Ni/Ti phase diagram, however, shows this temperature does not correspond to any significant thermal event, or melting event to which it is believed initiates the combustion synthesis reaction [8, 26]. As will be shown in this work, the ignition temperature is not constant and will typically lie between temperatures of 942^{o}C and 984^{o}C, which correspond to two distinct instances where liquid formation is possible.

Additionally, Dey [42] postulates that the synthesis reaction to form TiNi is triggered by the melting of Ni particles in the microstructure, which engulf the Ti particles and react accordingly. Conversely, Itin et al [26] indicate that once the melting point of the Ti-rich eutectic is attained, liquid appears at the contact between Ni and Ti and the two components dissolve into this, thus initiating the synthesis reaction to form TiNi.

1.6 Objectives

A study of the prior art shows that the only thermal analysis method used previously to study the sintering of Nickel and Titanium powders has been Differential Thermal Analysis (DTA). Additionally, DTA was only used to study the highly exothermic combustion reaction at elevated temperatures. DSC, as a thermal analysis method, has been used previously in the study of the Ni/Ti system, but solely to study the shape memory behaviour of the TiNi intermetallic, and not in the sintering of Nickel and Titanium powders. A great deal of information about the factors affecting the sintering behaviour of Ni and Ti powders can be obtained from using the DSC as an analysis tool, factors such as: powder size, peak temperature and hold time. Many past studies have looked at the effects of powder size, green density, heating rate and peak temperature; however none of these studies were performed *in situ* and relied on the observations of pre- and post-sintered microstructures and densities. Therefore, a primary purpose of this investigation was to develop an experimental technique using DSC capable of elucidating phase formation during sintering of a 50 atomic % Ni and 50 atomic % Ti powder compact in order to increase the understanding of the sintering mechanisms that take place during solid state and reactive sintering.

2 Experimental Methods

The primary experimental techniques used during this study are those of Differential Scanning Calorimetry, and microstructural characterization. These techniques are employed to study, both qualitatively and quantitatively, the effects of powder size, peak temperature, and hold time in the reactive sintering of Ni and Ti powder compacts. There are a number of sintering treatments utilized to study these effects using the DSC. Each thermal profile consists of one or more heating and cooling segments, some of which possess a hold segment at peak or intermediate temperatures. The purpose of the different thermal treatments is to study the effects of the various sintering parameters on the thermal transformations that can occur during the sintering of Ni and Ti powders.

2.1 Materials and Sample Preparation

Samples sintered in the DSC were prepared from pure powder mixtures of Nickel and Titanium, ranging in size from 1 to 90μm (Table 2-1 and Figure 2-1). The various size ranges used allowed for powder size effects on the thermally induced phase transformations to be studied using DSC. The powders were mixed (to a bulk composition of 50 at% Nickel) and milled in an inert Argon atmosphere. No effect of milling time was studied in this work.

Table 2-1: Nickel and Titanium powders used in this study

		Powder Type	Powder Size (μm)	Geometry	Supplier	Purity (metals basis)
Nickel	**Fine**	Inconel 110	1-2	spherical	Inco	N/A
		Inconel 123	11-14	spiky	Inco	N/A
	Medium	-325 mesh	<43	spherical	Alfa Aesar	99.8%
	Coarse	-170+200 mesh	75-90*	spherical	Alfa Aesar	99.8%
Titanium	**Fine**	-325 mesh	<43	angular	Alfa Aesar	99.5%
	Coarse	-170+200 mesh	75-90*	spherical	Alfa Aesar	99.9%

** indicates powders were sieved to this size range after receipt from supplier*

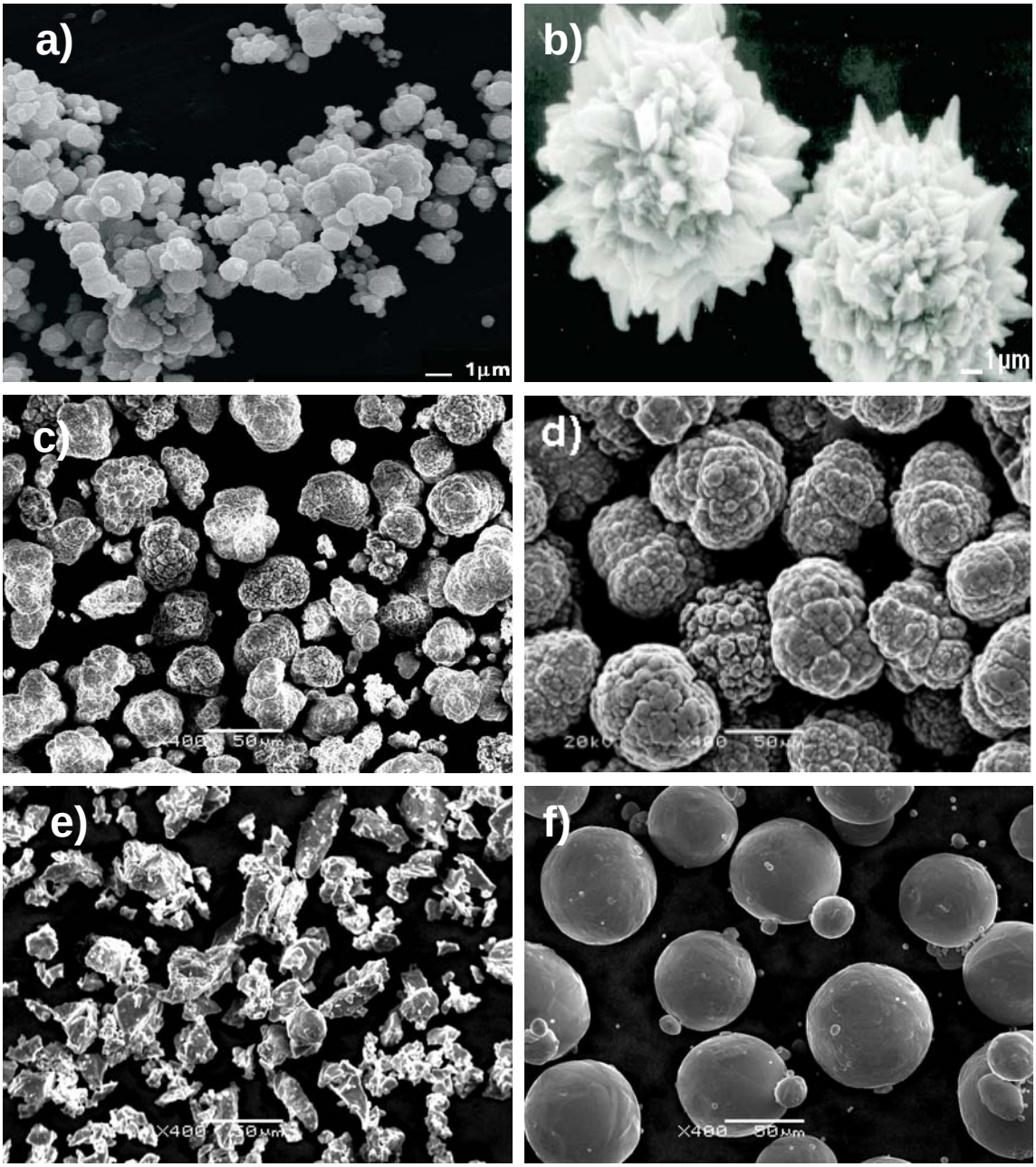

Figure 2-1: Starting Ni and Ti powders according to Table 2-1. a) Inconel 110 Ni [58], b) Inconel 123 Ni [58], c) -325 mesh Ni, d) -170+200 mesh Ni, e) -325 mesh Ti and f) -170+200 mesh Ti

Samples were uniaxially pressed to 535 MPa (1000 kg force) resulting in green densities ranging between 5.00 and 5.50 g/cm^3 (corresponding to theoretical densities of 81 to 89%). Pressed and sintered samples were in the shape of a disc, which allowed for both green and sintered densities to be determined by dimensional measurements of the sample diameter and thickness pre and post sintering. The average diameter of a green pressed disc was 4.83 mm, with the thickness varying between 0.5 – 0.6 mm depending on the mass of powder in the compact. During initial sintering studies, staining and discolouration of Alumina (Al_2O_3) crucibles would occur. Therefore, the crucible type was switched to Yttria (Y_2O_3) to prevent further staining. Yttrium was chosen as it has the highest affinity for oxygen of any element at temperatures below 1600^{o}C [59], making Y_2O_3 the most stable oxide in this temperature range.

After sintering in the DSC, samples were mounted in PolyFast phenolic resin with carbon filler obtained from Struers ™, and prepared for metallographic analysis by polishing to a mirror finish using a combination of diamond and colloidal silica polishing steps. The purpose of the carbon filler in the phenolic resin is to prevent a charge buildup on the sample surface in the SEM by making the entire sample and mount electrically conductive.

2.2 Sintering Treatments

A primary objective in completing the various sintering profiles of Table 2-2 was to determine the influence of peak sintering temperature and time on the microstructural evolution of the sintered compact. The specific peak temperatures used were designed to explore the sintering process under a wide range of conditions.

Table 2-2: Various DSC heating conditions

Heating Condition	Peak Temperature (^oC)	Hold Time (mins)
I	850	0, 60, 120, 300, 600
II	950	0, 60, 120, 300, 600
III	1020	0, 60, 120, 300, 600
IV	900	0, 30, 45, 60, 90, 120, 150, 180
V	*900-1020	0, 30, 45, 60, 90, 120, 150, 180

** samples were held at 900^oC, followed by heating to 1020^oC*

More specifically, sintering conditions I and IV represent solid state sintering. With reference to the Ni-Ti phase diagram, these two sintering treatments can be further distinguished. Both are above the eutectoid transformation at 765^{o}C. However the 850^{o}C and 900^{o}C treatments are below and above the α-Ti and β-Ti transformation for pure Ti respectively. Under heating condition I microstructural evolution during sintering may occur when the Ti-rich phases are a combination of α-Ti and β-Ti; whereas under heating condition IV, sintering will occur with only β-Ti.

Conditions II and III (i.e. Peak temperatures of 950^{o}C and 1020^{o}C) represent sintering conditions where a liquid phase (or transient liquid phase) may be present during sintering. Again, reference to the Ni-Ti phase diagram can distinguish these two sintering conditions further. Condition II has the potential to form liquid under the eutectic reaction:

$$\beta - Ti + Ti_2Ni \rightarrow L \qquad \textbf{(2-1)}$$

Condition III can create additional liquid through the melting of the Ti_2Ni phase and dissolution of some of the β-Ti and TiNi phases. Reports in the literature [47, 53, 54] indicate that a TE-SHS reaction can initiate during sintering above 950^{o}C. Therefore, in conjunction with liquid phase formation, conditions II and III may also represent sintering conditions where combustion synthesis occurs.

Finally, condition V was designed to study the influence that prior microstructural evolution in the solid state (i.e. 900^{o}C) has on the subsequent liquid phase/TE-SHS sintering process at higher temperatures (i.e. 1020^{o}C). Samples were heated to 1020^{o}C to fully resolve the TE-SHS exotherm on the DSC to allow for enthalpy measurements of this exothermic reaction. The energy associated with the TE-SHS reaction of Ni and Ti to form the TiNi intermetallic is found in literature to be 67 kJ/mol [60].

It should be noted that the phase transformations discussed above are not guaranteed to occur during sintering. In all cases, the formation of these phases relies on the metallurgical interaction between the elemental Ni and Ti powders in the green, pressed compact. In addition, the extent to which these phase transformations occur will depend on the degree to which the metallurgical reactions between Ni and Ti powders occur. In turn, this will strongly depend on the initial Ni and Ti powder size.

As indicated in Table 2-1, the coarse Nickel and Titanium powders received from Alfa Aesar were subsequently sieved to the range used in this study (74-89μm). The powders were, however, received in the size ranges of -100+325 mesh (43-150μm) and -150 mesh (<99μm) respectively. Sieve analysis for the coarse Nickel and Titanium powders was performed according to ASTM Standard B 214, which specifies that there be a mass loss no greater than 1% of starting material. The initial mass of each powder sieved was 100g, and from Tables 2-3 and 2-4 it can be seen that the mass recovered for coarse Nickel and Titanium powder was 99.8g and 99.6g, which corresponds to a mass loss of 0.2% and 0.4%, respectively.

Table 2-3: Results of seiving commercial -100+325 mesh (99.8% purity) spherical Nickel powder

Mesh Range	Size Range (μm)	Particle Diameter Upper Limit (μm)	Mass Retained (mg)	Particle Distribution (%)
-100+120	125-150	150	0.2	0.2
-120+140	104-125	125	0.1	0.1
-140+170	89-104	104	0.2	0.2
-170+200	74-89	89	81.8	81.9
-200+230	64-74	74	14.5	14.5
-230+270	53-64	64	2.7	2.7
-270+325	43-53	53	0.2	0.2
-325	38-43	43	0.2	0.2
		Total mass =	99.8	

Table 2-4: Results of seiving commercial -150 mesh (99.9% purity) spherical Titanium powder

Mesh Range	Size Range (μm)	Particle Diameter Upper Limit (μm)	Mass Retained (mg)	Particle Distribution (%)
+170	>89	99	33.8	34.0
-170+200	74-89	89	40.0	40.2
-200+230	64-74	74	10.0	10.0
-230+270	53-64	64	11.5	11.5
-270+325	43-53	53	3.4	3.4
-325+400	38-43	43	0.9	0.9
-400+450	32-38	38	0.1	0.1
		Total mass =	99.6	

The different powder size combinations and the corresponding sintering treatments used can be found in Table 2-5.

Table 2-5: Nickel and Titanium powder size combinations with corresponding heating conditions

Combination	Heating Condition	Nickel Type		Titanium Type	
1	I, II, III	coarse	-170+200 mesh	medium	-325 mesh
2	II, III	medium	-325 mesh	medium	-325 mesh
3	II, III	fine	Inconel 123	medium	-325 mesh
4	II, III	fine	Inconel 110	medium	-325 mesh
5	IV, V	fine	Inconel 123	coarse	-170+200 mesh

2.3 Differential Scanning Calorimeter Instrumentation

There are two types of DSC instruments available: power compensated differential scanning calorimeter and heat flux differential scanning calorimeter. Despite operating differently, the underlying principle behind the function of either type of instrument remains the same. In a differential scanning calorimeter, there are usually two specimens: the sample of interest and a suitable reference material (can be an empty reference crucible). The basic principle of DSC operation is that as a sample undergoes a heating cycle, it may undergo both exothermic and/or endothermic phase transformations. These phase transformations either require or liberate energy (in the form of heat) as they occur. An exothermic reaction is one in which heat is liberated by the sample, and an endothermic reaction is the opposite, heat is required by the sample in order for the reaction to take place. The DSC can quantify this liberation/requirement of heat, which allows one to determine the nature and extent of the reaction taking place. An example of an endothermic and exothermic phase transformation are, respectively, the melting and solidification of a metal.

A power compensation differential scanning calorimeter operates under the principle that the heat flow to both the sample and reference side should be maintained the same (within allowable tolerances). Therefore, any variation in heat flow between the sample and reference side due to a thermal event, is recorded as a temperature difference (ΔT).

A heat flux differential scanning calorimeter operates differently than a power compensated differential scanning calorimeter in that the sample and reference side of the

instrument should be maintained at the same temperature (within allowable tolerances). As a thermal event occurs, more or less heat is required (depending on the nature of the thermal event) by the sample side to maintain its temperature with the reference. This variation in heat requirement to maintain a minimal temperature difference between both sample and reference is recorded as heat flow (mW/mg) as a function of sample temperature. The experimental work of this research was performed using a heat flux differential scanning calorimeter: DSC 404C Pegasus purchased from Netzsch Instruments. This instrument possesses a high-temperature furnace that operates in the temperature range of room temperature up to 1500^{o}C. It uses a DSC-Cp type measuring head and a type S (Pt10%/Pt-Rh) thermocouple.

2.3.1 Principles of DSC Measurement

Differential Scanning Calorimetry is a thermal analysis technique that can be used to determine thermally induced phase transformations within a sample. When coupled with the appropriate software, a differential scanning calorimeter can allow one to experimentally determine the specific heat of a sample, or determine the enthalpy of transition (ΔH) for a variety of phase transformations. This is accomplished by obtaining heating and cooling curves (Figure 2-2) for the sample using thermal analysis software. The combination of these curves is known as a thermal cycle (or thermal profile).

Before a sample can be run in the differential scanning calorimeter, a correction file must be run to account for any thermal changes of the sample and reference crucibles that can occur over the temperature range of interest. This correction file is subsequently

subtracted from the sample file after it is run (which happens automatically with the thermal analysis software used in this study). One advantage of having a correction file is that it can be used to subtract out background noise due to machine effects or sample carrier and crucible effects, which could otherwise affect the peaks detected for the thermal events of interest (by affecting their onset/finish temperatures, or the area under their corresponding transformation peaks). Taking the correction file into account also provides for relatively smooth (and horizontal) baselines, and good baseline stability (minimal noise).

Recorded energy of phase transformations show up on a DSC thermal profile as a deviation from the baseline, which typically resembles a peak in either the exothermic or endothermic direction (depending on the nature of the phase transformation). Using the thermal profile, one can determine the enthalpy of transition for a specific phase transformation simply by integrating the area under the peak obtained in the experimentally-determined heating or cooling curve (Figure 2-3). For Figure 2-3, T_i and T_f represent the actual initial and final temperatures of the thermal event, respectively. T_{ei} and T_{ef} represent the estimated initial and final temperatures of the thermal event, which are calculated by taking the intersection between an extrapolated baseline, and a line tangent to the peak on either side. Lastly, T_p represents the temperature when the thermal event has attained its highest energy value.

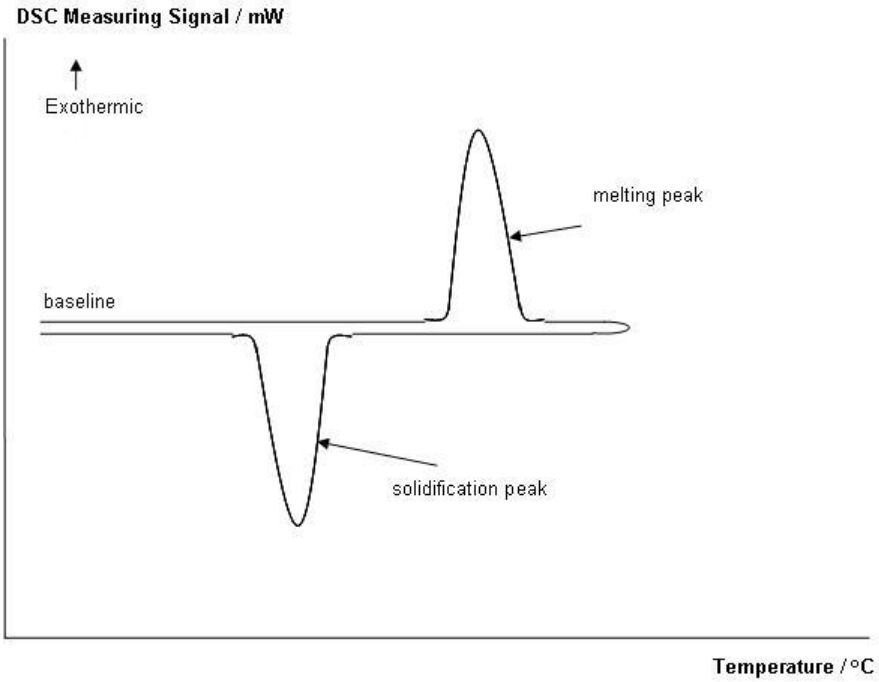

Figure 2-2: Schematic of a DSC thermal profile

The area under the desired phase transformation peak (F) is known to be proportional to the actual enthalpy of transition (ΔH) for that specific phase transformation [61]. This is given as:

$$F = K \cdot m \cdot \Delta H \qquad \textbf{(2-3)}$$

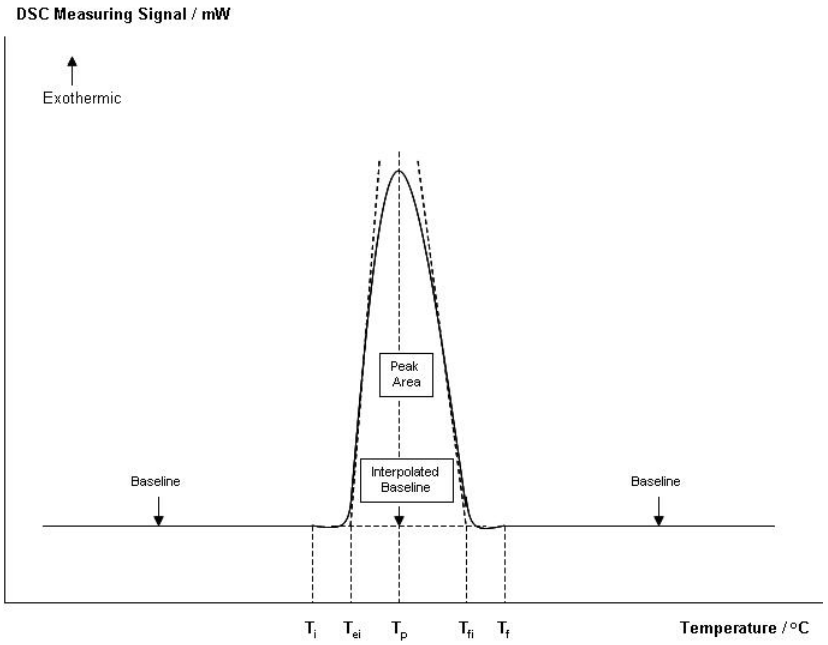

Figure 2-3: Example of an Ideal Peak on a DSC Thermal Profile **[61]**

Thus, if ΔH for a phase transformation were desired, it could be calculated using a rearrangement of Equation (2-3), such that:

$$\Delta H = \frac{F}{K \cdot m} \qquad \textbf{(2-4)}$$

The calibration factor K is an experimentally determined constant, using a set of standard reference materials. It will be different from one machine to the next, and must be predetermined before any quantitative experimentation can be performed. The m term represents the mass of the sample.

The purpose for calibrating an instrument is to ensure accurate measurements from the measuring head of the calorimeter. To do this, pure reference materials are run separately through multiple heating cycles, each cycle consisting of one heat up and one cool down. From this, the melting temperature of the reference material, and enthalpy of melting are recorded, and averaged over the number of cycles. These values are compared to standard theoretical values from literature for this material, and the results are considered acceptable if they are within ±3% of theoretical values.

2.3.2 Peak Area Calculations

In the idealized case of Figure 2-3, the thermal profile returns to the same baseline value as before the thermal transformation occurred. This allows for a linear baseline interpolation to be assumed for peak area calculation. Another type of thermal profile can occur when the baseline does not return to the same value (Figure 2-4). To calculate the area under this transformation peak, a number of methods could be employed. A

straight linear interpolation of the baseline across the entire peak area could be used as an approximation; or a straight line horizontal interpolation could be used that splits the peak area in half, and uses the left baseline as an interpolation for the left half of the peak area, and a similar procedure for the right half of the peak area. Lastly, a spline interpolation of the baseline across the entire peak could be used. If the onset and finish temperatures of a thermal event are relatively symmetric with respect to the peak intensity temperature (T_p), then both a linear and spline interpolation across the baseline of the peak will result in similar values.

Since the peak areas measured for the thermal events that are observed in the present work all return to the same, or similar, baseline values, only linear interpolation was used for peak area measurements. Only the actual initial (T_i) and final (T_f) temperatures of each peak were used in calculating the integration range.

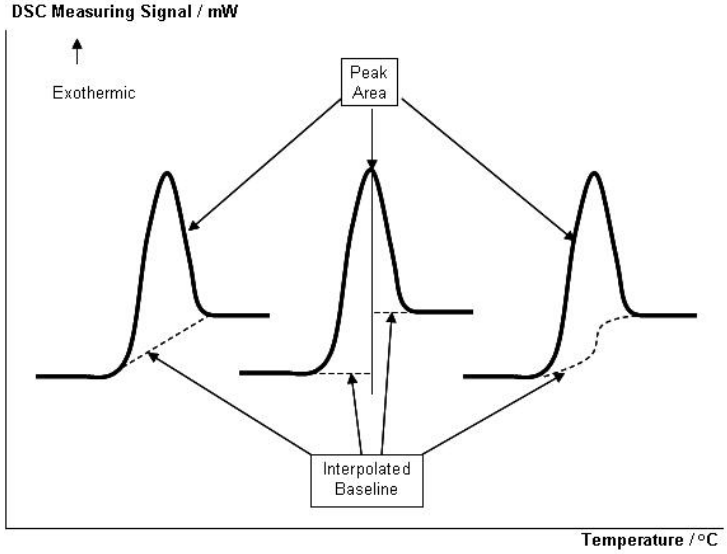

Figure 2-4: Schematic representation of peak area calculation for baseline with differing values before and after transformation peak

2.4 DSC Analysis of the Shape Memory Effect

The SME was studied for samples consisting of the same powder combination as used in heating conditions IV and V (cf. Table 2-5). This allowed for the microstructural effects of these heating conditions to be related to the SME displayed at low temperature. Since the same powder combination is used for both heating conditions, the only difference between heating conditions IV and V is the quick heat up to 1020^{o}C to initiate the combustion reaction (condition V). Therefore, the effects of combustion on the low temperature SME can be discerned.

In studying the SME of TiNi, samples were heated to 150^{o}C peak temperature at 3 K/min, and cooled to room temperature, in order to resolve the martensite to austenite phase transformation, as well as the reverse phase transformation of austenite to martensite, on the DSC. If the R → B19' transformation is above room temperature, it is possible to determine if one-stage (B2 → B19') or two-stage (B2 → R → B19') martensitic transformation is occurring from the SME on cooling. A two-stage transformation will appear as a doublet peak on the DSC, whereas a one-stage transformation will consist only of a single peak on cooling. If however, the R → B19' transformation is below room temperature (and thus not recordable by the DSC used in the present work), then it is not possible to determine if a single peak observed on cooling is due to either the B2 → R or B2 → B19' martensitic transformation.

3 Experimental Results

Figure 3-1 represents the DSC thermal profiles obtained when heating pure Nickel and Titanium powder separately to a peak temperature of 950^{o}C. The purpose for heating samples of the pure powders is to ascertain any thermal events that might be recorded by the DSC as a result of transformations in either metal. These transformations are recorded by the DSC as endothermic/exothermic events which appear as 'peaks' on the heating and cooling segments. In the DSC profile for pure Titanium powder, an endothermic peak is recorded during the heating segment which has an onset temperature of 883^{o}C, reaching peak intensity above 900^{o}C. This corresponds to the α-Ti to β-Ti transformation for pure Ti. In the DSC profile for pure Nickel powder, a smaller endothermic event is recorded between 300^{o}C and 400^{o}C.

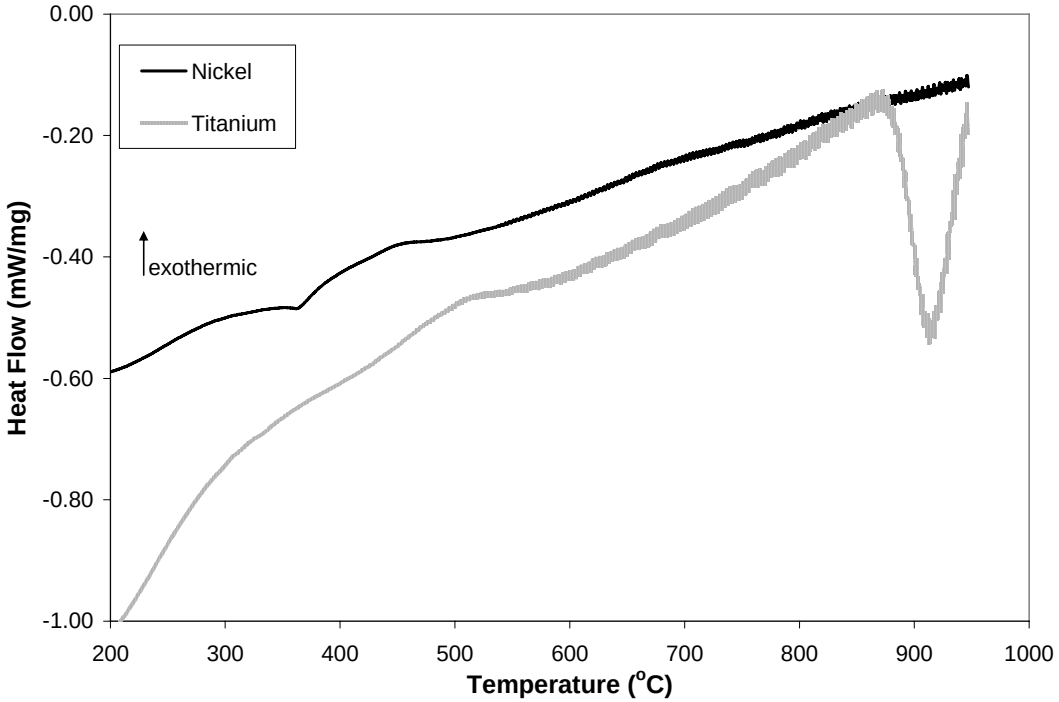

Figure 3-1: DSC heating curves for pure Nickel and Titanium powder

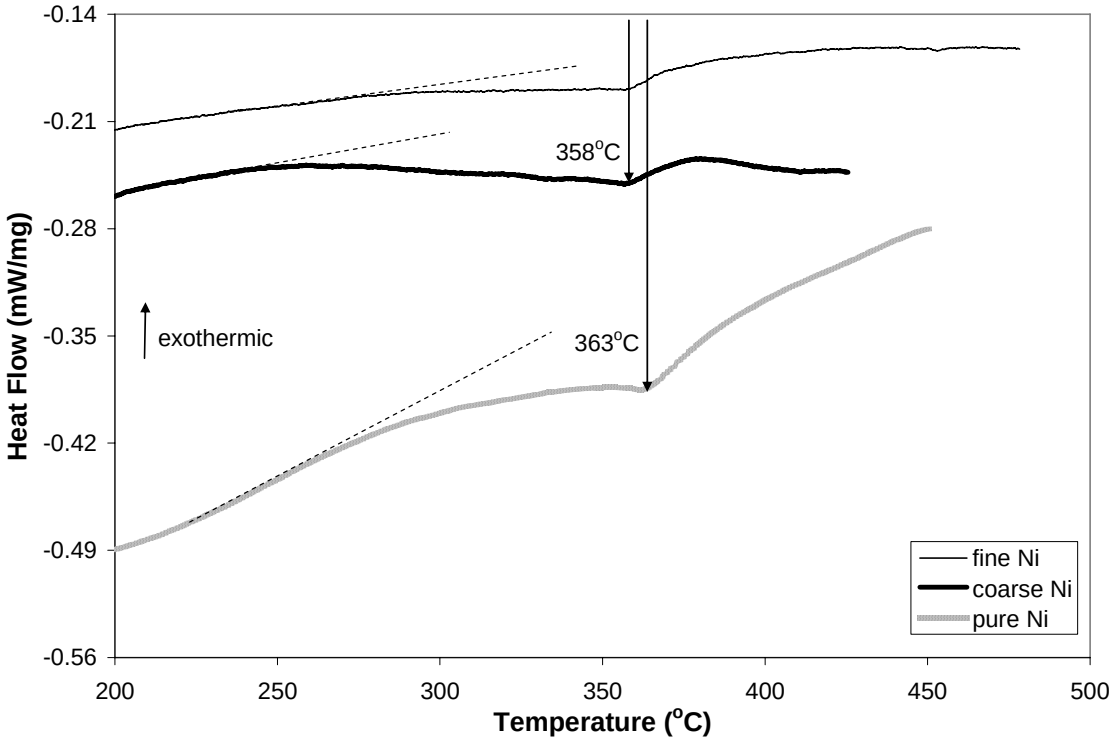

Figure 3-2: Endothermic event recorded during the heating of Ni/Ti powder mixtures containing fine (Inconel 123) and coarse Ni (-170+200 mesh) with medium Ti (-325 mesh) powder

The low temperature thermal event seen in Fig. 3-1 for pure Ni powder can also be seen during the heating of Ni and Ti powder mixtures, as evidenced in Fig. 3-2. This thermal event is measured by the DSC as an abrupt change in the thermal profiles for the Ni/Ti samples during heating. The temperature of this thermal event corresponds closely to the Curie point for Ni. No correction file was run prior to running the pure Ni and Ti sample files, which is the cause for the observed noise and non-horizontal baseline. The heating curves for both powder mixtures appear to possess a relatively horizontal baseline when compared to the pure Ni curve, as they do incorporate correction files.

3.1 General Thermal Behaviour of Ni and Ti Powder Mixtures

The general thermal behaviour for mixed Ni and Ti powder compacts heated to peak temperatures of 1020^{o}C is represented by the DSC heating and cooling curves of Figures 3-3 and 3-4. These samples contain medium Titanium powder (-325 mesh) with various indicated Nickel powder sizes. It is apparent that there are a number of different thermal events occurring within the samples as they are sintered to, and cooled from, peak temperature. It is also evident that powder size has an effect on the predominance of any one thermal event.

Figure 3-3 indicates a slightly exothermic reaction occurring between the Ni and Ti powders during heating from 650^{o}C to 900^{o}C for all powder combinations with the exception of the sample containing coarse Ni (-170+200 mesh, 74-89μm). For the sample containing Inconel 110 Ni powder, an endothermic event is observed to occur during this exothermic region, which has an onset temperature of 765^{o}C and ends at 883^{o}C.

At temperatures above 940^{o}C, a highly exothermic reaction is recorded by the DSC, the magnitude of which has a dependence on the specific powder size combination. In this case, a larger Ni powder results in an increased magnitude of this exothermic reaction. When a medium Ni powder (-325mesh) is used, the magnitude of this exothermic reaction is greatly reduced, albeit still present. For samples containing fine Ni powder (Inconel 110 and 123), this reaction does not appear. This result indicates this reaction has a dependence on the powder size used, or more specifically, the overall surface contact area between the Ni and Ti powders.

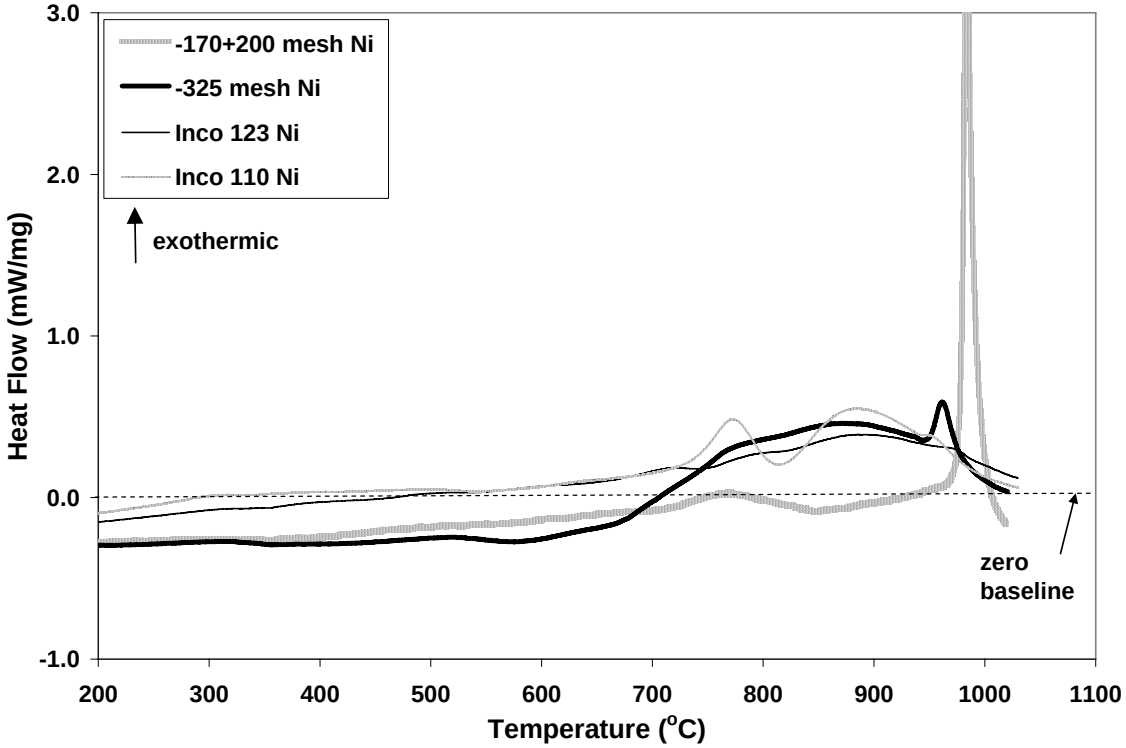

Figure 3-3: DSC heating curves for compositionally mixed Ni (various sizes) and Ti (-325 mesh) powders

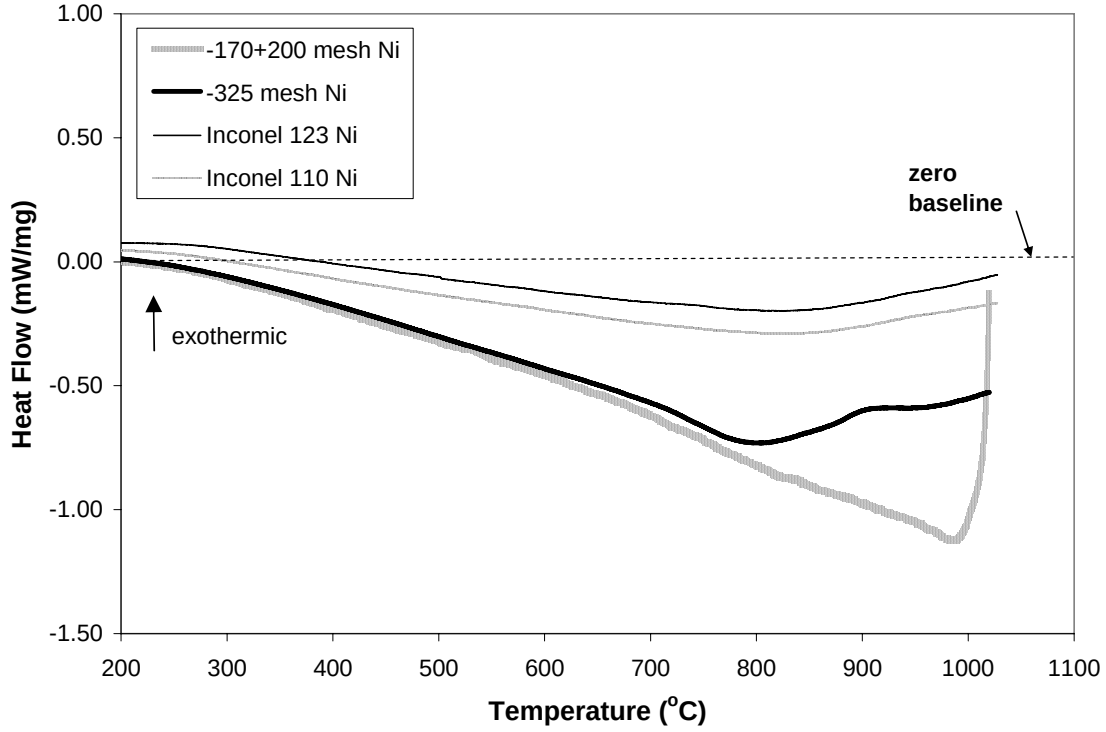

Figure 3-4: DSC cooling curves for compositionally mixed Ni (various sizes) and Ti (-325 mesh) powders

There are no significant thermal events observed during cooling from a peak temperature of 1020^{o}C, for any of the powder combinations used. This does not necessarily mean that these powder combinations will never display thermal events during cooling, just that they do not appear to for this specific heating/cooling condition.

Figure 3-5 shows the microstructural evolution and bulk density that results from sintering for 2 hours at 950^{o}C, for the powder combinations of -325 mesh Ti with (a) -170+200 mesh Ni, (b) -325 mesh Ni, (c) Inconel 110 Ni and (d) Inconel 123 Ni powder. Density improves with a decrease in Ni powder size, and in the finer Ni powder mixtures phase evolution is more rapid. This supports the conclusion that the exothermic shift in the DSC baselines (ie. 600^{o}C to 900^{o}C) for finer Ni powders is the result of metallurgical reactions between the pure Ni and Ti powders. With the exception of the coarse Ni sample, all samples appear relatively homogeneous with no un-reacted Ni powder evident, making microstructural features hard to distinguish. From a microstructural perspective, it would be ideal to study samples consisting of coarse Ni, so that phase formation and evolution during sintering to form TiNi is easily distinguishable.

With this in mind, compacts consisting of coarse Ni (-170+200 mesh) and medium Ti (-325 mesh) were pressed and sintered according to heating conditions I, II and III. Figure 3-6 shows the microstructure of these pressed powder compacts in the unheated state. Packing density variation near the periphery of the powder compact is evident (left side of picture).

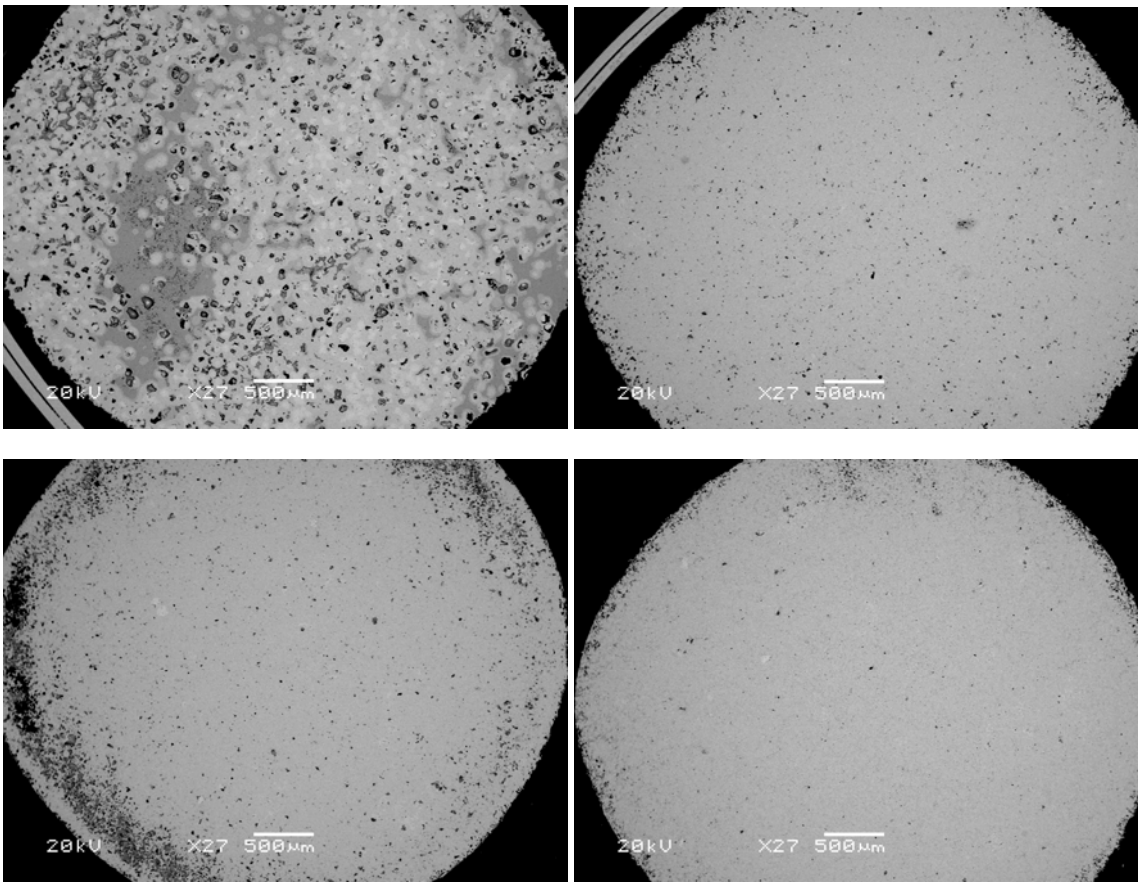

Figure 3-5: SEM backscatter images showing microstructural evolution and bulk density for samples consisting of -325 mesh Ti powder with a) -170+200 mesh, b) -325 mesh, c) Inconel 110 and d) Inconel 123 Ni powder sintered at 950^{o}C for 2 hours

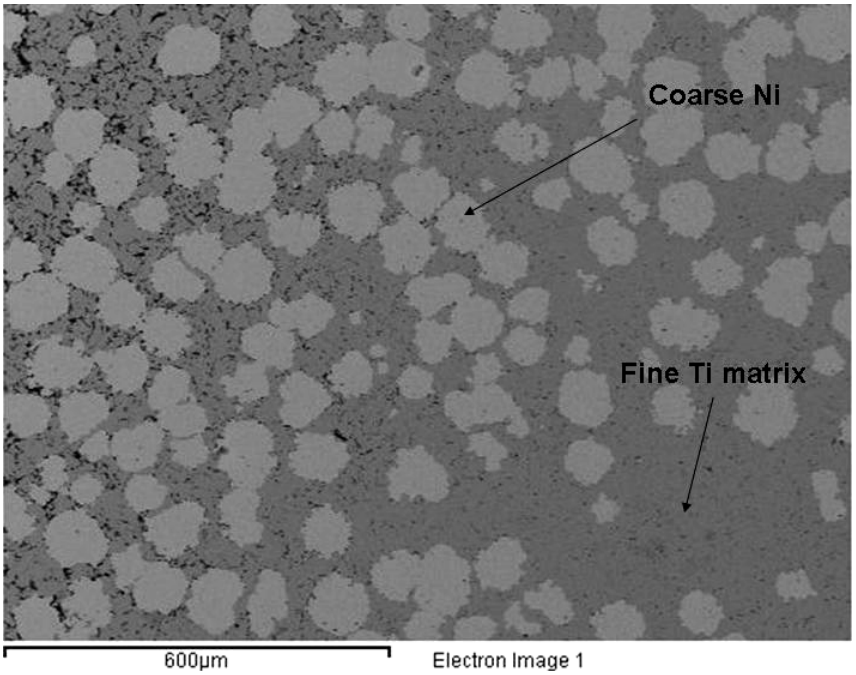

Figure 3-6: Unheated pressed compact containing an equi-atomic mixture of coarse Ni (-170+200 mesh) and medium Ti (-325 mesh)

3.2 Heating Condition I – Peak Temperature 850^{o}C

Figure 3-7 shows the microstructural evolution for powder compacts containing coarse Ni (-170+200 mesh) and medium Ti (-325 mesh) sintered to a peak temperature of 850^{o}C, and held at peak temperature for various times. The effect of hold time at peak temperature on microstructural evolution and sintered density is evident. As hold time is increased, the density decreases, with porosity developing at the sites of the coarse Ni particles. Rings of porosity appear around the Ni rich cores starting at 120 minute hold time at 850^{o}C, with large pores (black spots) evident in the microstructure of the 600 minute hold sample. These large pores appear where existing Ni rich cores were located, and are likely introduced during polishing as Ni rich cores surrounded by a great deal of porosity are pulled from the sample. The Ti-rich matrix changes with increasing hold time, while the sintered density of the matrix remains relatively constant. As will be shown in more detail later, the changing contrast around the Ni cores is an indication of intermetallic phase formation.

As Figure 3-3 indicates the heating segments of coarse Ni mixtures up to 850^{o}C show no major thermal events. Figure 3-8 shows the DSC cooling segments for the samples sintered under heating condition I. The exothermic event at 745^{o}C is observed for all samples held at this peak temperature. This reaction increases in magnitude up to a hold time of 300 minutes, after which the magnitude decreases for the 600 minute hold sample. This would suggest an optimal time to maximize this reaction at this temperature, should that be desired. The dashed lines represent the linear baseline used in calculating the peak areas.

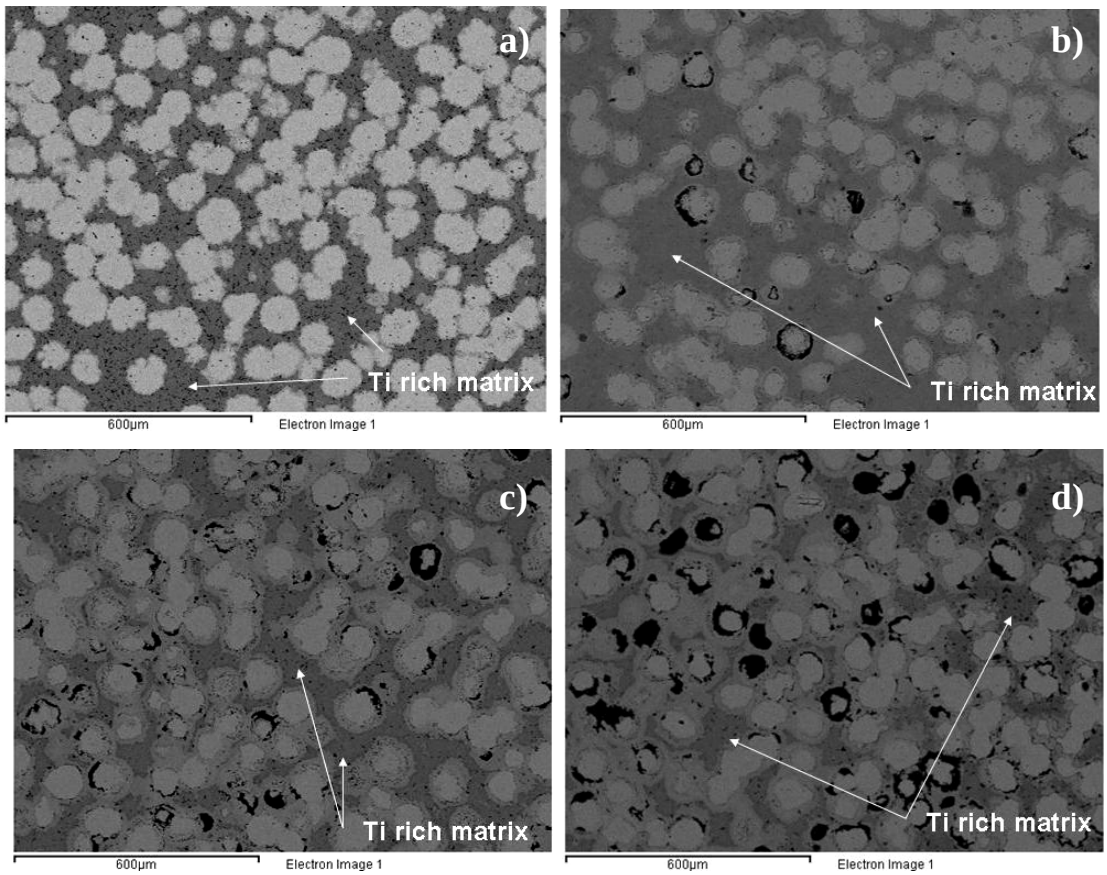

Figure 3-7: SEM backscatter images of coarse Ni, medium Ti samples held for a) 60, b) 120, c) 300 and d) 600 minutes at 850°C peak temperature

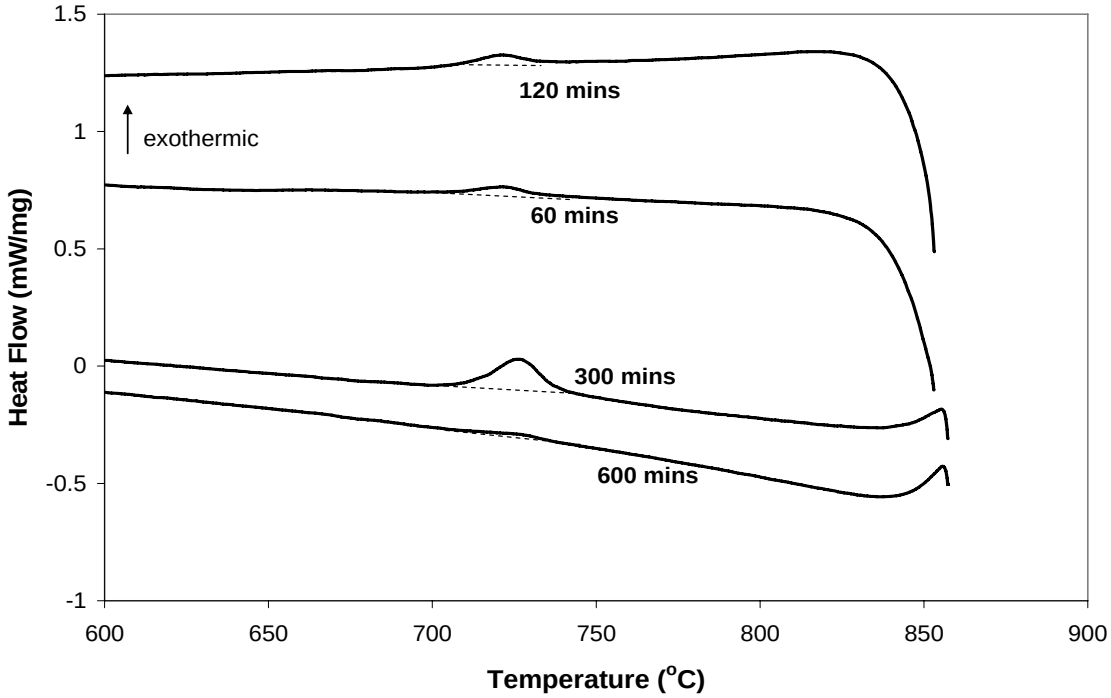

Figure 3-8: DSC cooling curves for samples consisting of -170+200 mesh Ni and -325 mesh Ti powder, held at 850°C for varying times

3.3 Heating Condition II – Peak Temperature 950°C

Figure 3-9 shows the microstructural evolution for powder compacts containing coarse Ni (-170+200 mesh) and medium Ti (-325 mesh) sintered to a peak temperature of 950°C, and held at peak temperature for 60, 120, 300 and 600 minutes. There is still porosity development in the Ni rich cores similar to the samples heated to 850°C; however there is also a noticeable decrease in the sintered density of the Ti-rich matrix surrounding the coarse Ni particles as hold time is increased.

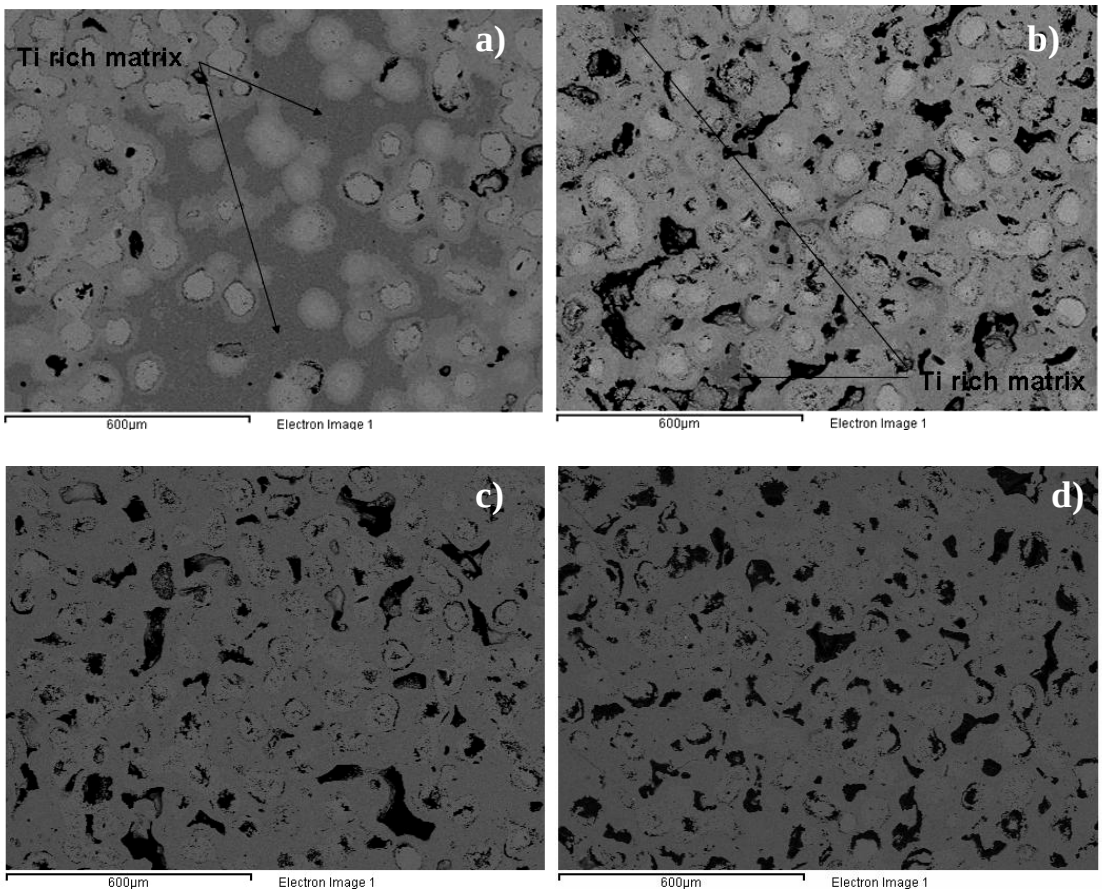

Figure 3-9: SEM backscatter image of a sample held for a) 60, b) 120, c) 300 and d) 600 minutes at 950°C peak temperature

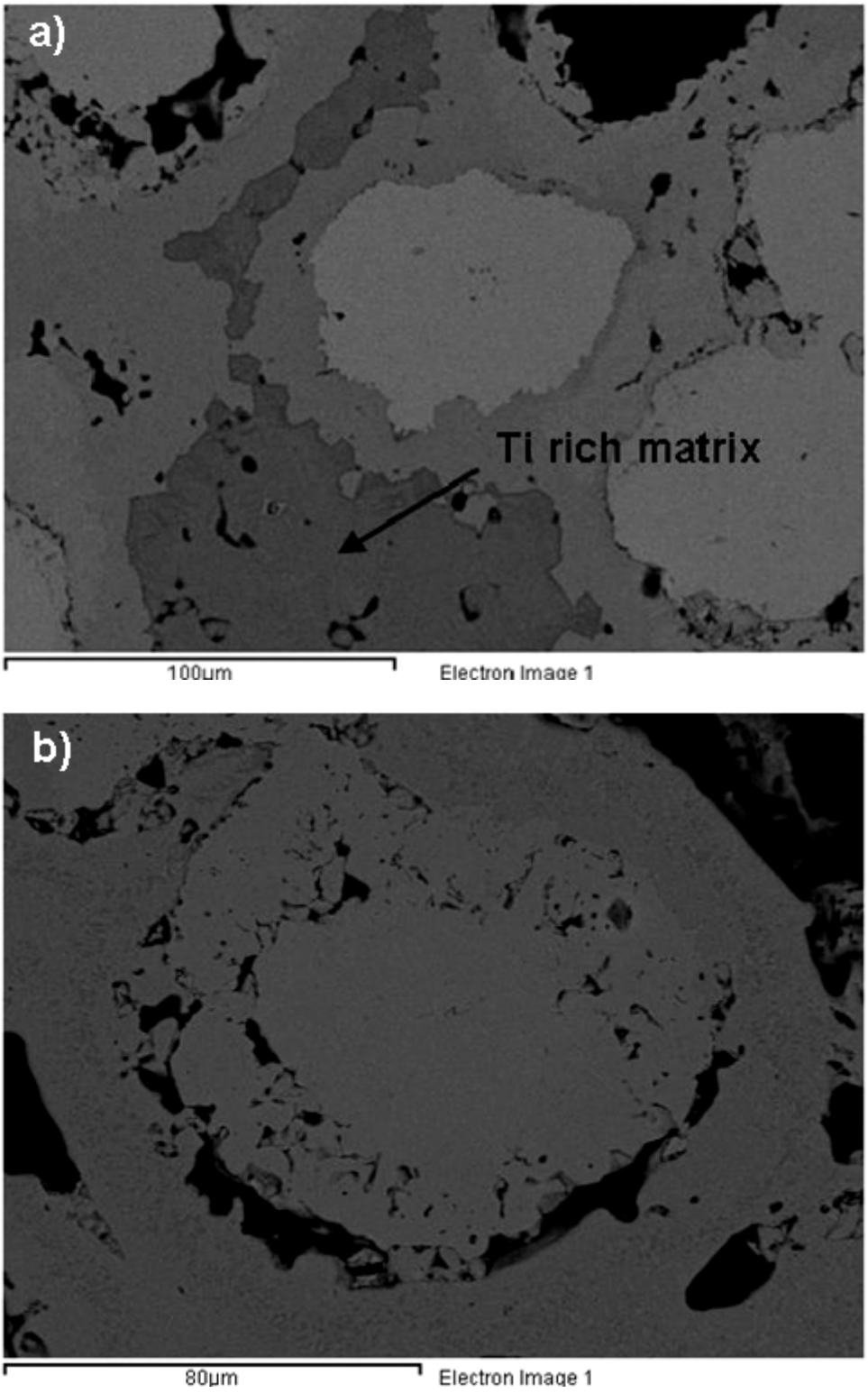

Figure 3-10: High magnification SEM backscatter image of sample held for a) 600 minutes at 850^{o}C and b) 300 minutes at 950^{o}C peak temperature

Phase evolution occurs much more quickly in the samples held at 950°C when compared with those heated to 850°C and held. The Ti-rich matrix is completely converted to intermediate phases of Ni and Ti by 300 minutes (Fig 3-9c), whereas in the samples heated to 850°C, Ti-rich matrix surrounding the coarse Ni particles was very much evident up to 600 minutes hold at peak temperature (Fig 3-7d). This is evidenced by the higher magnification SEM images of Figure 3-10.

The DSC cooling segments for the samples sintered under heating condition II (Figure 3-11) show the exothermic event at 745°C is observed only for samples held at peak temperature for 60 and 120 minutes with a decrease in magnitude for increased hold time. This would suggest that the phase present within the microstructures that causes this observed exothermic reaction at 745°C, is no longer present for the samples held at 950°C for 300 and 600 minutes.

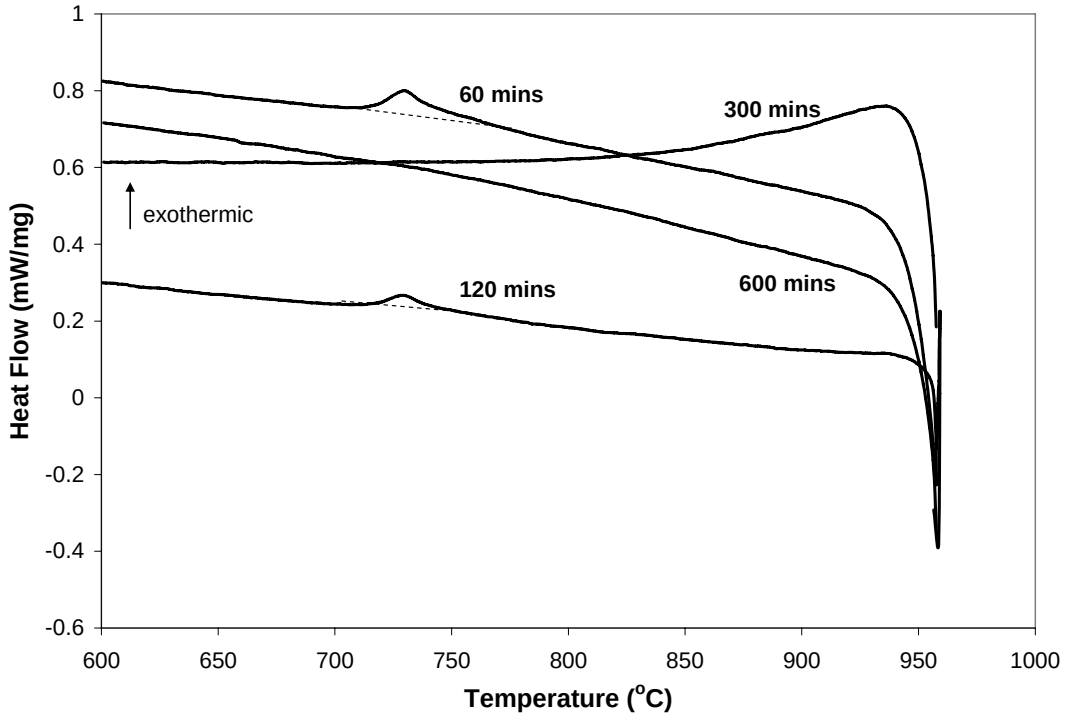

Figure 3-11: DSC cooling curves for samples consisting of -170+200 mesh Ni and -325 mesh Ti powder, held at 950°C for varying times

Table 3-1 shows the enthalpy values obtained when measuring the exothermic peaks observed to onset below 765^{o}C during cooling for the samples consisting of coarse Ni and medium Ti powder heated to 850^{o}C and 950^{o}C peak temperature (Figures 3-8 and 3-11). Observing the Ni/Ti phase diagram of Figure 1-1, it can be deduced that the exothermic event occurring at 745^{o}C observed during cooling on the DSC is the result of a eutectoid decomposition of β-Ti into α-Ti and the Ti_2Ni intermetallic.

Table 3-1: Enthalpy measurements for exothermic reactions observed on cooling in Figures 3-8 and 3-11

time (mins)	Enthalpy (J/g)	
	850 ^{o}C	950 ^{o}C
0	3.173	8.125
60	4.064	3.406
120	7.299	1.87
300	6.18	0
600	5.712	0

3.4 Heating Condition III – Peak Temperature 1020^{o}C

Figure 3-12 shows the DSC heating and cooling curves for a coarse Ni (-170+200 mesh) sample with medium Ti (-325 mesh) powder heated to 1020^{o}C and cooled. There is a highly exothermic reaction observed to onset at 984^{o}C during heating, and nothing observed during cooling.

Figure 3-13 shows the microstructure obtained for a sample of coarse Ni with medium Ti, heated to 1020^{o}C according to heating condition III. There is a great deal of porosity evident from this microstructure (appears as dark area with light flecks), which is located in the Ti matrix surrounding the coarse Ni particles. Moreover, phase formation within this microstructure has progressed to a much larger extent when compared with a sample heated to 950^{o}C (Figure 3-9a).

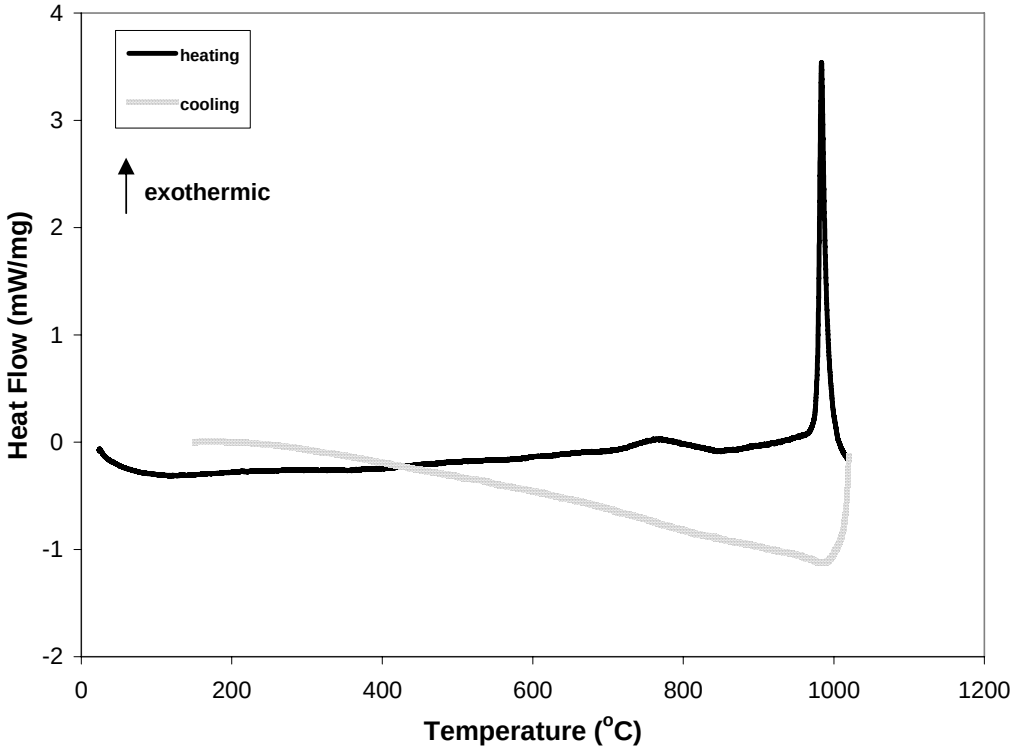

Figure 3-12: DSC heating and cooling curves for a sample with coarse Ni heated to 1020°C

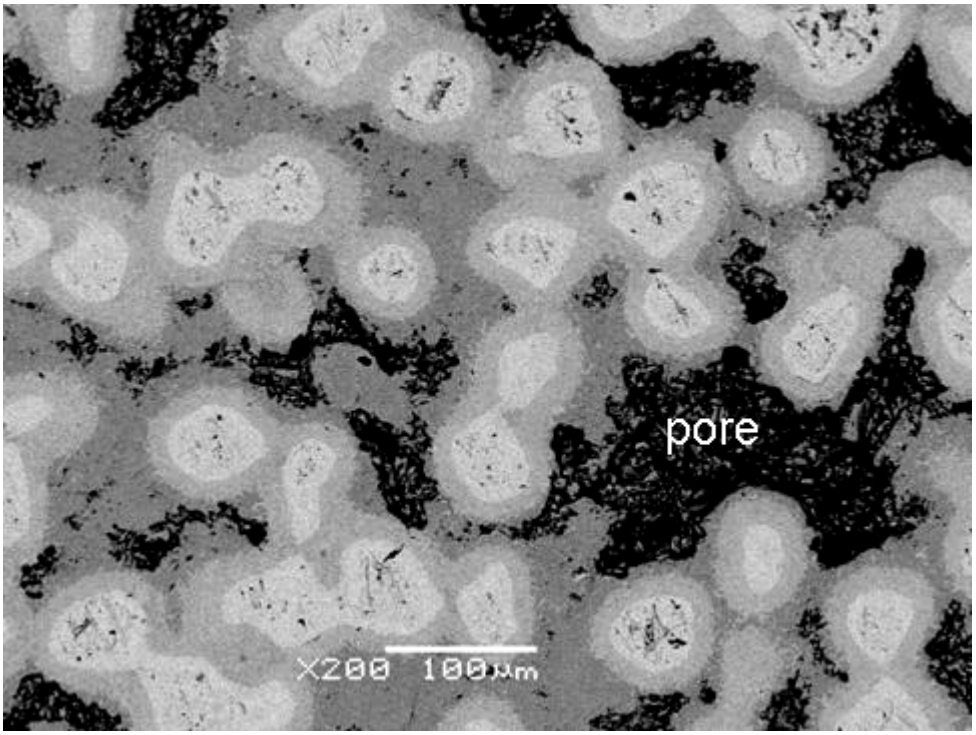

Figure 3-13: SEM backscatter image of a coarse Ni, medium Ti sample heated to 1020°C and cooled

3.5 Heating Condition IV – Peak Temperature 900°C

It was desired to study the Ti-rich eutectoid reaction using a coarse Ti powder so as to develop a correlation between microstructural evolution and the observed DSC thermal behaviour of this reaction. A temperature of 900°C was chosen because it is above the α-Ti to β-Ti transformation for pure Ti at 883°C. To this end, samples consisting of coarse Ti (-170+200 mesh) and fine Ni (Inconel 123) powder were pressed and sintered according to heating condition IV. Figure 3-14 shows a powder compact consisting of coarse Ti (-170+200 mesh) and fine Ni (Inconel 123) powder in the unheated green state.

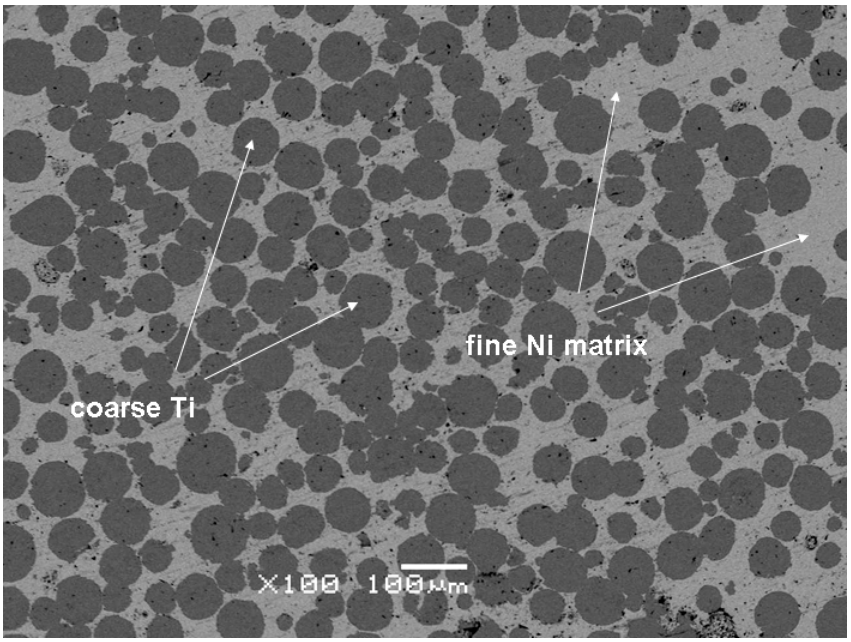

Figure 3-14: Pressed powder compact consisting of fine Ni (Inconel 123) and coarse Ti (-170+200 mesh) in the unheated green state

The DSC cooling results after sintering at 900°C for varying time (Figure 3-15) show this eutectoid decomposition is transient in nature, and has a dependence on the sintering time at peak temperature. This is evidenced microstructurally in the SEM backscatter images of samples sintered to 900°C (Figure 3-16) and held for (a) 0, (b) 30 and (c) 120 minutes respectively. The area fraction of Ti-rich eutectoid core decreases with an increased hold

time at 900°C sintering temperature. This can be seen more clearly in the higher magnification SEM backscatter images of samples sintered at 900°C for varying time (Figure 3-17).

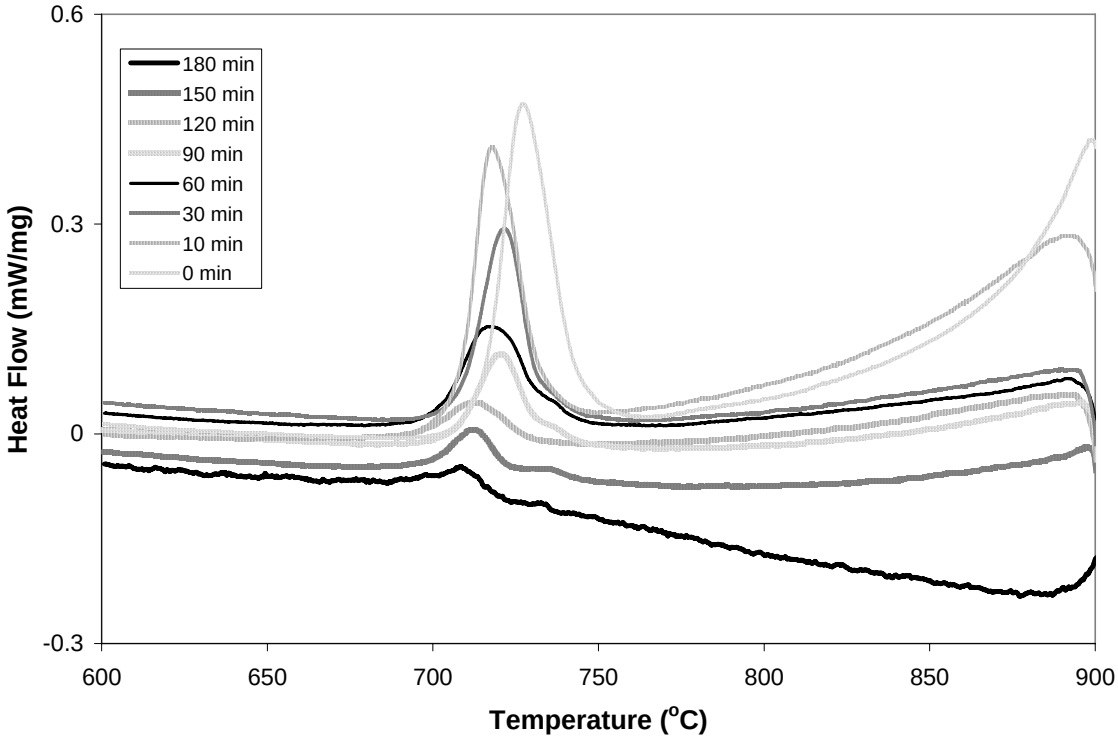

Figure 3-15: DSC cooling curves after sintering at 900°C for varying time

Table 3-2 shows the enthalpy values obtained when measuring the exothermic peaks observed to onset below 765°C during cooling for the samples consisting of Inconel 123 Ni and coarse Ti powder heated to 900°C peak temperature (Figure 3-15).

Table 3-2: Enthalpy measurements for exothermic reaction on cooling observed in Figure 3-15

Time at 900°C (min)	**Enthalpy of Exotherm** (J/g)
0	26
30	13.6
60	10.1
90	7.7
120	3.2
150	2.35
180	1.48

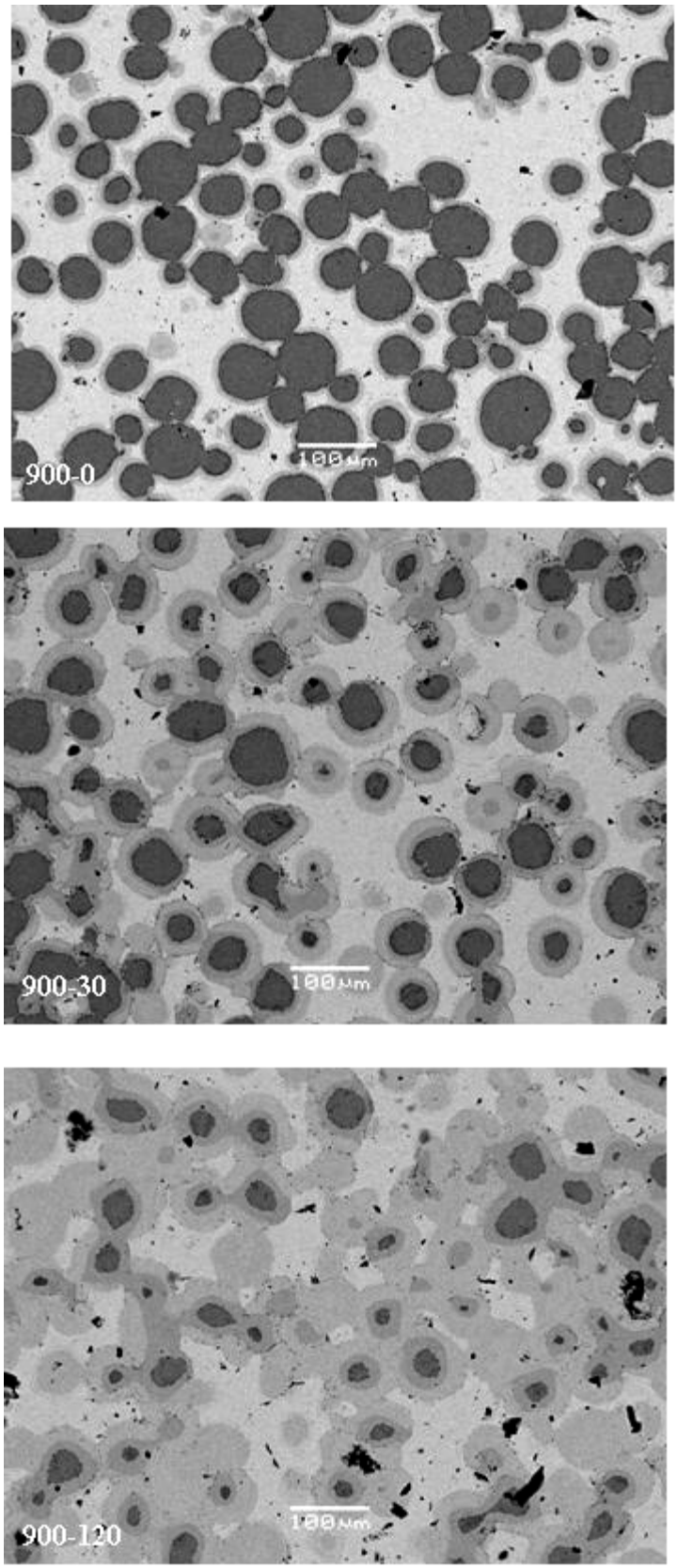

Figure 3-16: SEM backscatter images of TiNi samples heated to 900°C and held for a) 0, b) 30 and c) 120 minutes

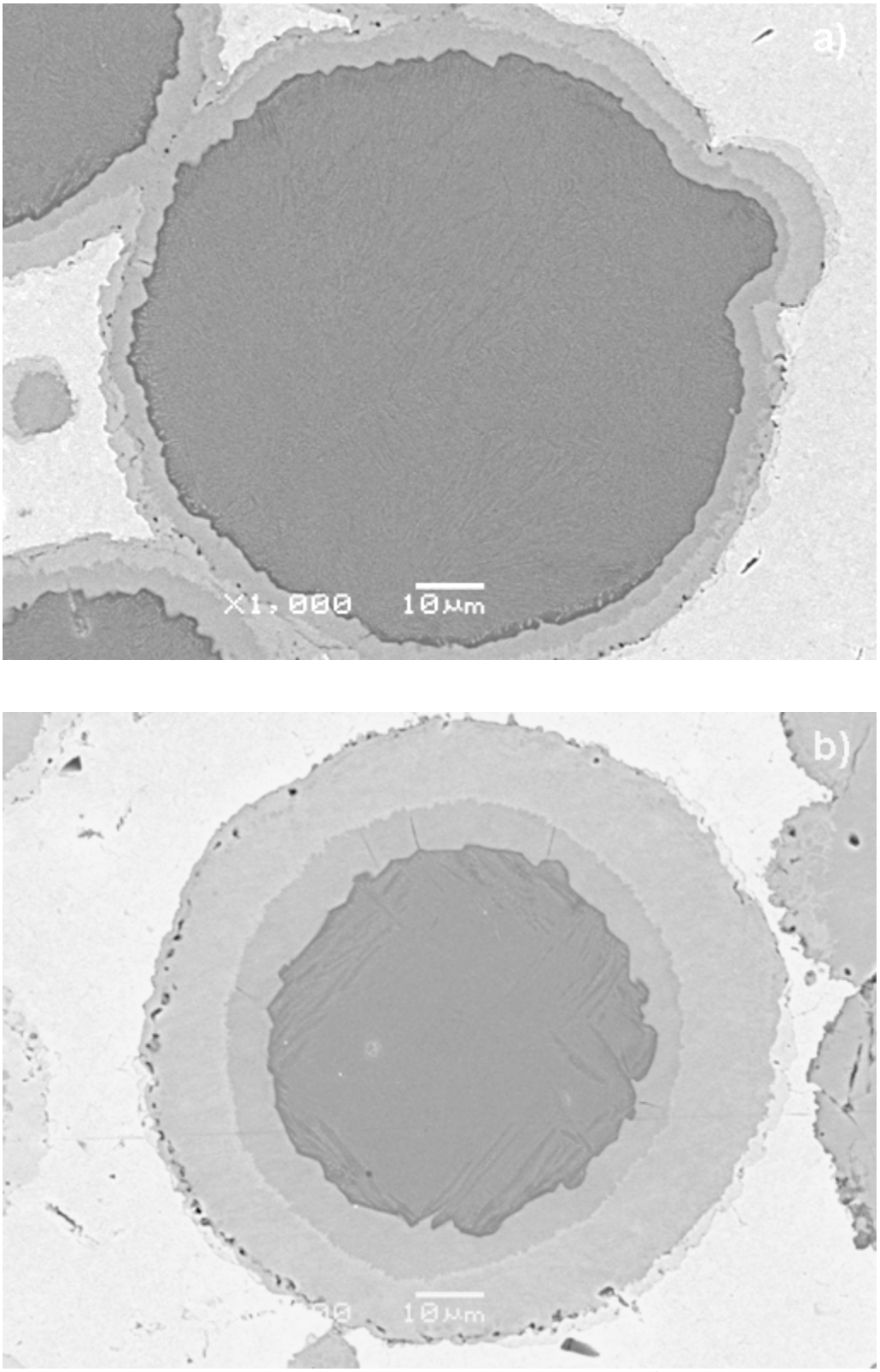

Figure 3-17: SEM backscatter image of a Ti-rich core after sintering to 900°C with a) 0 and b) 30 minute hold

3.6 Heating Condition V – Hold at 900°C, Heat to 1020°C

As aforementioned, heating condition VI was designed to study the influence that prior microstructural evolution in the solid state (i.e. 900°C) has on the subsequent liquid phase/TE-SHS sintering process at higher temperatures (i.e. 1020°C). Samples were heated to 1020°C to fully resolve the TE-SHS exotherm on the DSC to allow for enthalpy measurements of this exothermic reaction.

Figure 3-18(a) shows the DSC heating curves for coarse Ti (-170+200 mesh) and fine Ni (Inconel 123) samples heated to 1020°C after various hold times at 900°C. An endothermic peak is observed to onset at 944°C, which is followed immediately by a strong exothermic reaction, the magnitude of which decreases with increasing hold time at 900°C. At 984°C, another endothermic event onsets which, similar to the exothermic reaction preceding it, decreases in magnitude with increasing hold time at 900°C.

Figure 3-18(b) shows the DSC cooling curves for the coarse Ti samples cooled from 1020°C to room temperature. Two exothermic events are evident upon cooling, one immediately upon cooling from 1020°C, and a second that has an onset at 984°C. The second exothermic event decreases in magnitude with an increase in hold time at 900°C before heating to 1020°C. No quantitative measurement was performed on the peaks observed during cooling from 1020°C. Only qualitative conclusions were drawn. However, if the peaks were to be measured, the most accurate method would be spline interpolation, as discussed in Section 2.3.2.

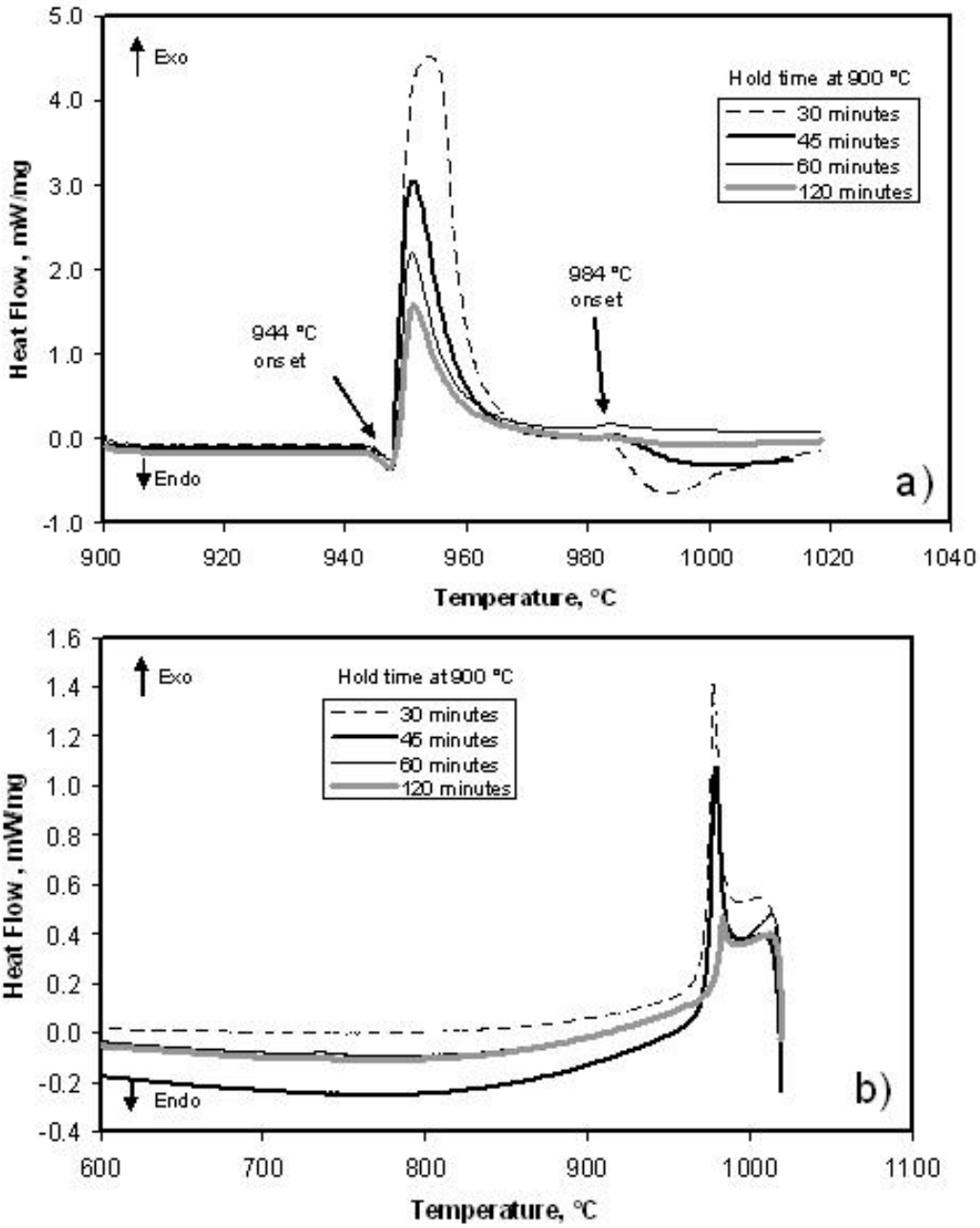

Figure 3-18: DSC trace of Ni/Ti samples heated to 900°C, held for indicated times and then a) heated to 1020°C and b) cooled to room temperature

Figure 3-19 shows the measured densities obtained for coarse Ti (-170+200 mesh) and fine Ni (Inconel 123) samples a) in the green pressed state, b) sintered to 900^{o}C and held for various times, and c) heated to 1020^{o}C after a hold at 900^{o}C to initiate the combustion reaction.

The optical microscopy images of Figure 3-20 compare samples sintered to 900^{o}C, and further heated to 1020^{o}C. These images represent sample microstructures before and after the highly exothermic reaction observed in the DSC (ie. separate samples that underwent heating conditions IV and V respectively). Large scale porosity is evident for samples in which the highly exothermic reaction has occurred. This porosity appears at the site of prior Ti cores.

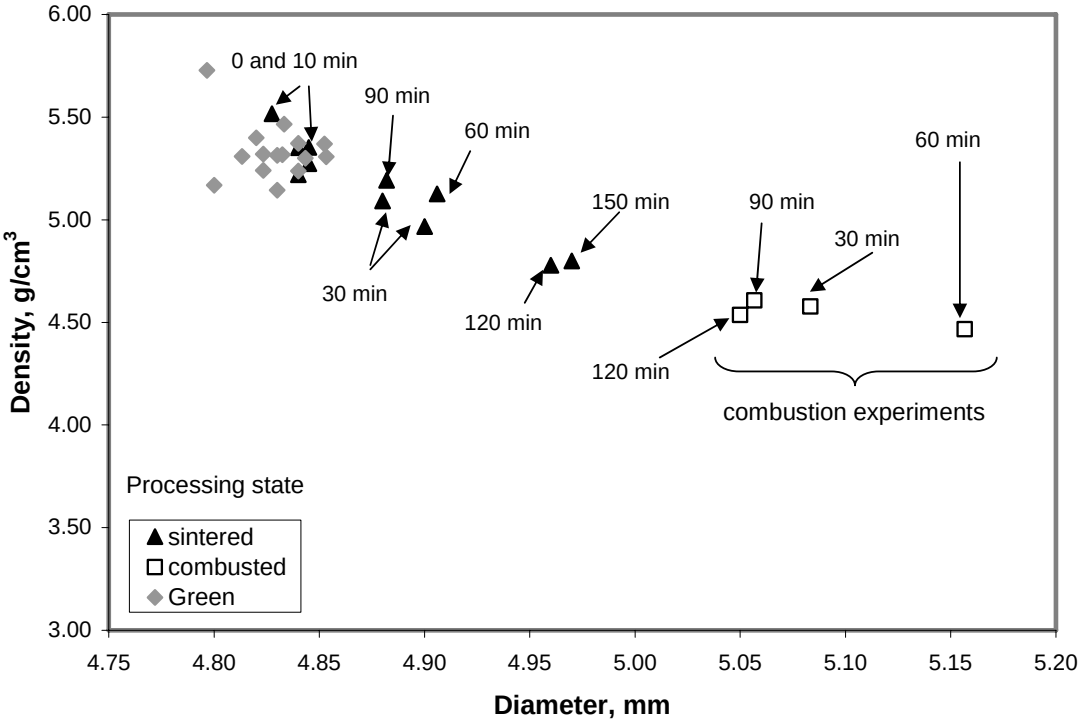

Figure 3-19: Density versus diameter of coarse Ti (-170+200 mesh) and fine Ni (Inconel 123) compacts in the pressed green state, after sintering at 900°C and following combustion at 1020°C

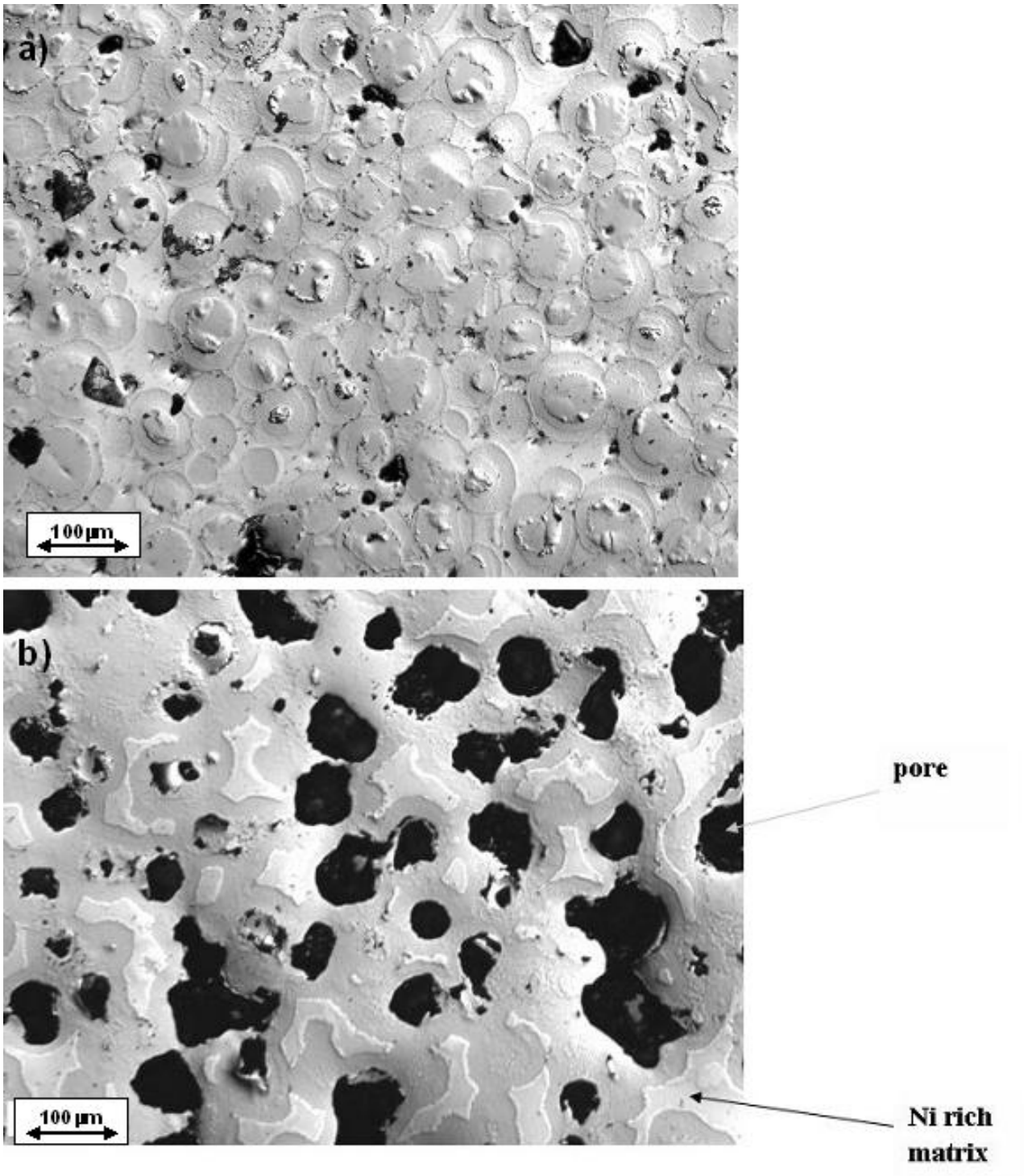

Figure 3-20: Optical images of coarse Ti (-170+200 mesh) and fine Ni (Inconel 123) compacts sintered at 900°C for; a) 60 minutes and b) further heated to 1020°C

4 Discussion

It is evident from observing the DSC thermal analysis results that a number of thermal events and phase transformations can occur when sintering pure Ni and Ti powders to elevated temperatures. These thermal events are recorded by the DSC as either an endothermic/exothermic shift in the baseline value, or as endothermic/exothermic peaks. These results will be explained using conceptual unit cell models similar to Figure 4-1. The unit cell below is representative of a sample that contains coarse Ni (-170+200 mesh) surrounded by a matrix of finer Ti (-325 mesh) powder.

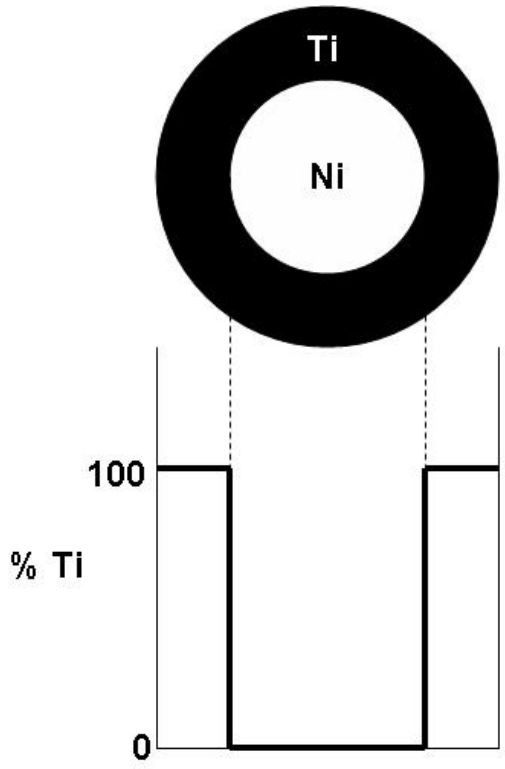

Figure 4-1: Conceptual unit cell for a Ni particle surrounded by Ti in the unheated state

During heating to temperatures below 765^{o}C, interdiffusion between Ti and Ni may occur and the slow growth of intermetallic phases is possible. The unit cell of Figure 4-2

highlights the microstructural progression during heating to this peak temperature. The three possible intermetallic phases (Ti_2Ni, TiNi, $TiNi_3$) are grouped as one phase (for simplification) and labeled IMC.

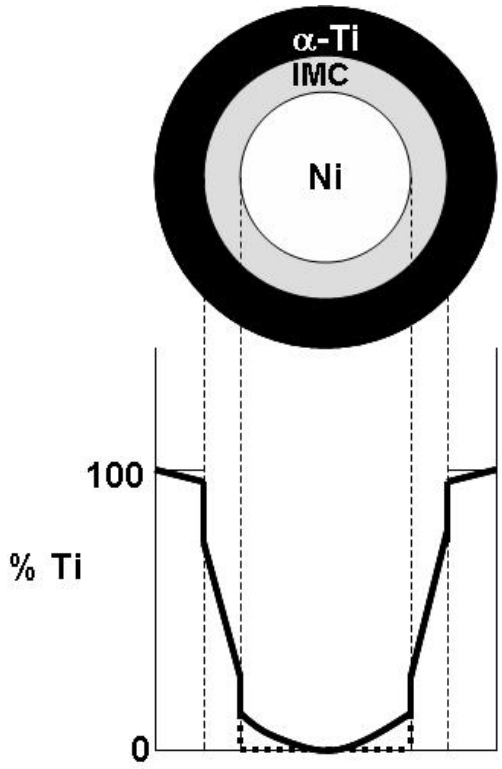

Figure 4-2: Conceptual unit cell heated to 765°C

For the Ni particle, if interdiffusion occurs the Ti concentration profile throughout it will decrease from the maximum solid solubility of Ti at the Ni/IMC interface (~10wt% at 765°C), to 0wt% at the center of the particle (according to the solid curve). Likewise, if little interdiffusion has occurred, then the concentration profile through the Ni particle will be zero, representing minimal solid solution alloying with Ti and relatively pure Ni (according to the dashed line).

In the experimental results for the heating of pure Ni powders to 950°C, an abrupt change in the thermal profiles is measured by the DSC at 363°C. At first glance the DSC curve

of Figure 4-3 might be interpreted as a broad endothermic peak onsetting at approximately 210^{o}C and ending around 450^{o}C; however, there are no phase transformations in the Ni-Ti system that would correspond to such a temperature range. To understand the possible cause of the measured thermal effect during heating of pure Ni, the specific heat of Nickel is plotted versus temperature (Figure 4-4) according to [62].

4.1 Curie Transformation on Heating

From Figure 4-4, it can be seen that the specific heat of Ni changes dramatically up to 358^{o}C, after which there is an abrupt drop in the specific heat which coincides with the Curie point [63]. Considering that the distance of the baseline from zero on a DSC thermal profile represents the specific heat of the sample (Figure 4-5), a deviation from this baseline would therefore be representative of a change in the specific heat from C_{p1} to C_{p2}. The deviation (in the endothermic direction) of the thermal profile increases as temperature is increased to the Curie point of Nickel. This endothermic deviation is the result of the specific heat of Nickel increasing with temperature. As the specific heat increases, the amount of heat that can be accommodated by Nickel also increases which is represented by an endothermic deviation in the thermal profile. Additionally, the abrupt change at 358^{o}C in the thermal profile (Figure 4-3) is in the exothermic direction, indicating that the sample specific heat has suddenly decreased, which according to Figure 4-3, should happen once the Curie point of Nickel is reached.

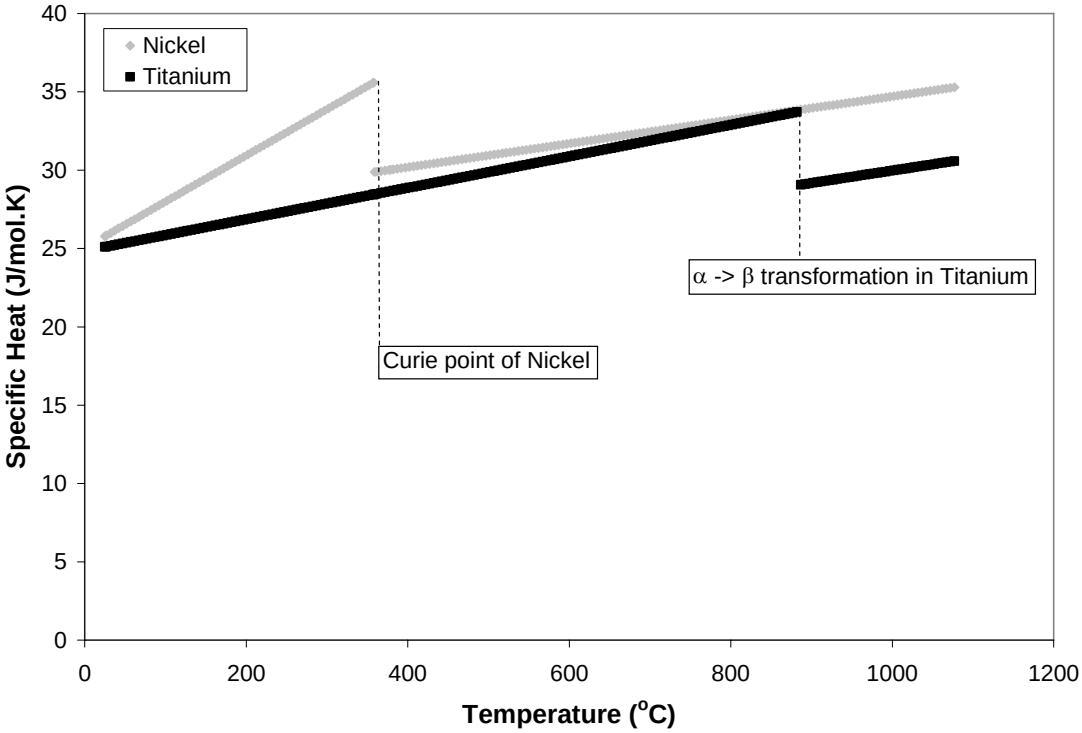

Figure 4-3: Specific heats of Nickel and Titanium plotted versus temperature

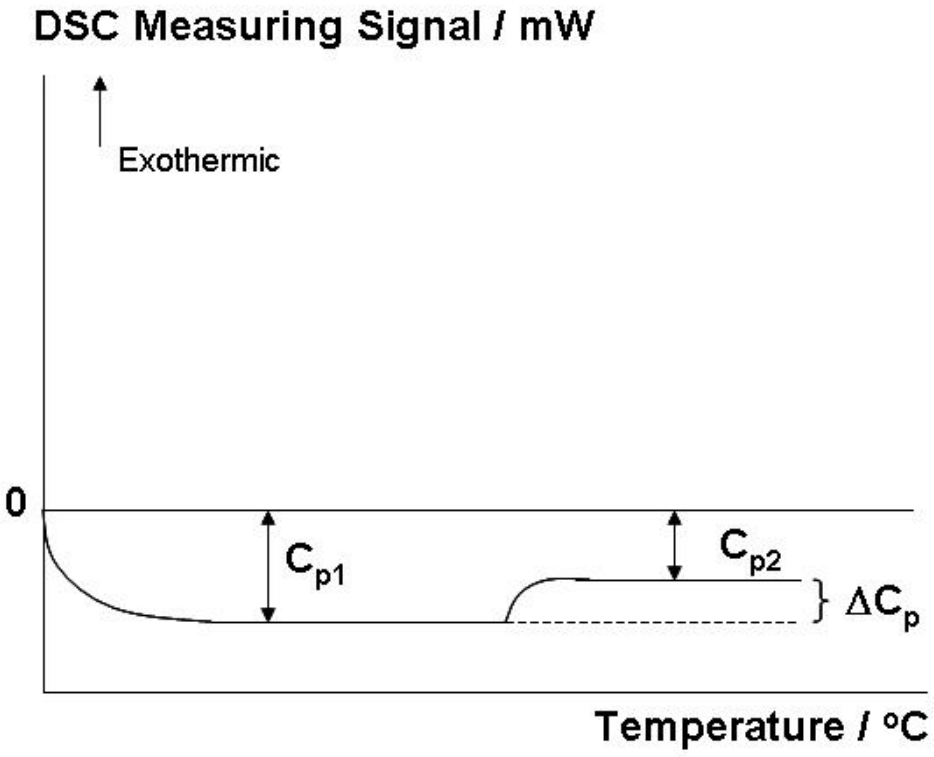

Figure 4-4: Schematic representation of a sudden heat capacity change as indicated on a DSC thermal profile

This sudden decrease in the value of the specific heat means that less energy is needed to raise the temperature of Ni per degree Celsius of furnace temperature increase. There is no associated crystallographic change in the structure of Ni at 358^{o}C to account for this change in specific heat. There is, however, a loss of the magnetic properties of Ni at the Curie point. According to [64], the observed specific heat (c_{obs}) is comprised of a number of factors:

$$c_{obs} = c_q + \left(c_p - c_v\right) + c_i + S \quad \textbf{(4-1)}$$

where c_q is the specific heat at constant volume according to the Debye theory; $(c_p - c_v)$ is the correction for dilatation; c_i represents the excess over the Debye value common to most metals; and the "excess term" S includes effects due to magnetization and other causes. Once the Curie point is reached for Nickel it loses its magnetic properties, the contribution to specific heat due to magnetization disappears, which results in a sudden change in the observed specific heat for Ni.

Figure 4-6 shows the effect of solid solution alloying of Ti on the observed Curie transformation in Ni [65]. This figure shows that even at very dilute concentrations of Ti, the Curie transformation can be significantly lowered in temperature. Considering the first evidence of a change in sample specific heat occurs at 358^{o}C (indicated by the exothermic shift in Figure 4-3), it can be concluded that little to no solid state interdiffusion of Ti into the Ni powder core to create a Ni rich solid solution has occurred up to this temperature, as there has been only a 5^{o}C depression of the Curie point in the Ni/Ti mixtures containing fine and coarse Ni. Referring to the conceptual unit cell of

Figure 4-2, this result would indicate the Ti concentration profile across the Ni particle to be close to zero (ie. relatively flat), indicative of minimal solid solution alloying.

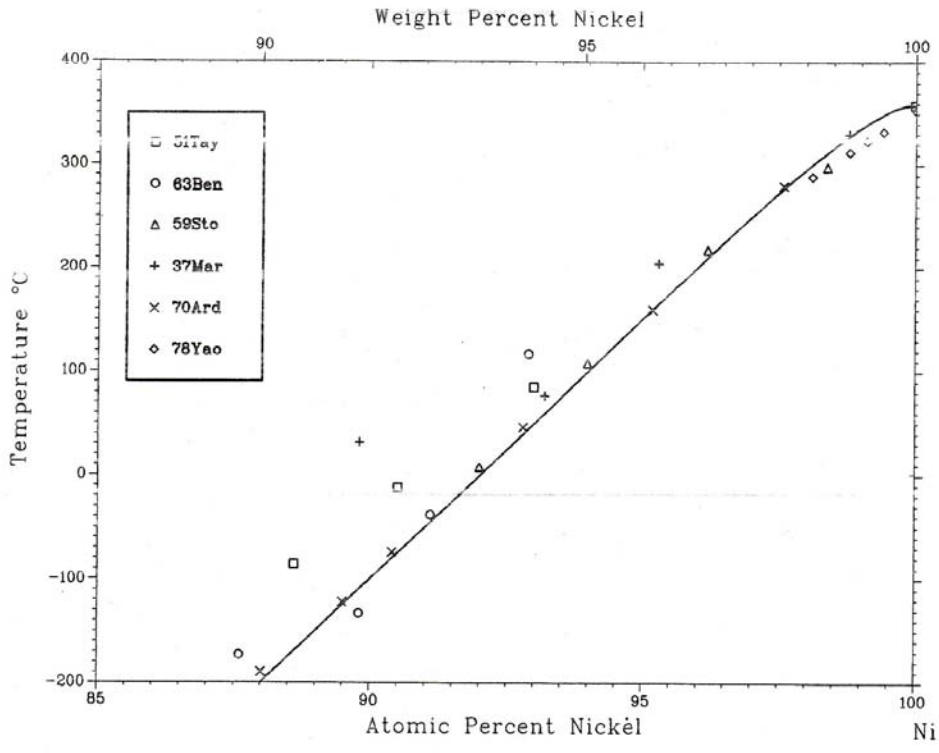

Figure 4-5: Effect of Titanium content on the Curie point of Nickel **[65]**

The use of DSC to measure the Curie transformation in the Ni/Ti powder compacts is useful in making a qualitative determination on the presence of pure Ni within the samples, or the degree to which solid solution alloying of the Nickel has occurred. The scale of Figure 4-3, however, indicates this thermal event to be comparatively negligible to those occurring at elevated sintering temperatures, and as a result was not studied further.

4.2 α-Ti to β-Ti Transformation during Heating

During the heating of mixed Ni and Ti powders, the Ni/Ti phase diagram shows the potential for a reaction to occur between α-Ti and the Ti_2Ni intermetallic at 765°C. This reaction is a eutectoid reaction, and can be expressed by:

$$\alpha - Ti + Ti_2Ni \rightarrow \beta - Ti \qquad \textbf{(4-2)}$$

With reference to the unit cell of Figure 4-2, closer inspection of the Ti/IMC interface (Figure 4-7) reveals that if enough interdiffusion in the α-Ti occurs during heating, then this phase will reach its maximum solid solubility for Ni (~0.3wt%) when a peak temperature of 765°C is reached. At this temperature, the concentration profile through the α-Ti layer will be such that the Ti concentration drops from 100wt% to 99.7wt% (as per the dashed curved line). Provided a well developed interface exists between the α-Ti and Ti_2Ni intermetallic, this concentration profile means that a majority of the α-Ti layer will undergo the eutectoid reaction upon heating past 765°C. If minimal interdiffusion has occurred, then the concentration profile through the α-Ti layer will follow the solid curved line, which means a minimal amount of the α-Ti layer will undergo the eutectoid reaction upon heating past 765°C. With further heating, the remaining α-Ti will transform gradually as the Ni concentration decreases through the layer, until 883°C is reached, at which point any remaining pure α-Ti will transform to β-Ti.

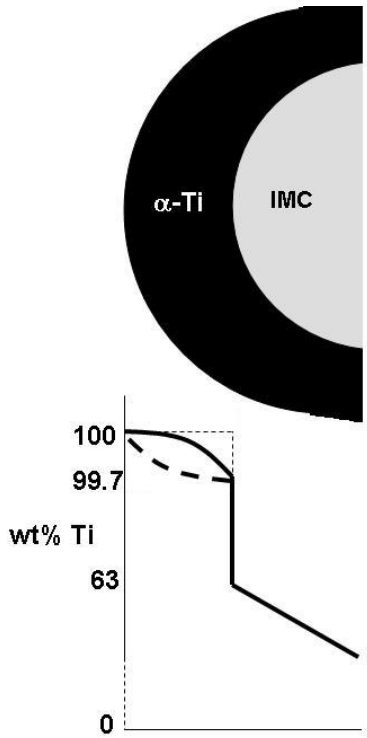

Figure 4-6: Conceptual unit cell showing Ti concentration profile through a-Ti at 765°C

From the DSC results of Figure 4-8, both exo- and endo-thermic thermal events can be seen during heating. The slightly exothermic reaction between Ni and Ti causes an exothermic deviation from baseline above temperatures of 650°C, and represents the formation of intermetallic compounds (as shown in Chapter 1.3). An example of this exothermic deviation on the DSC can be seen in Figure 4-9.

On the other hand the endothermic events observed are the result of the gradual conversion of α-Ti to β-Ti above 765°C. Not only does this endothermic transformation act opposite the exothermic intermetallic formation, but according to diffusion couple studies by Bastin and Rieck [66], the presence of β-Ti also acts to decrease the growth rate (k) of both the Ti_2Ni and TiNi intermetallics; as shown in Figure 4-10 and 4-11 respectively.

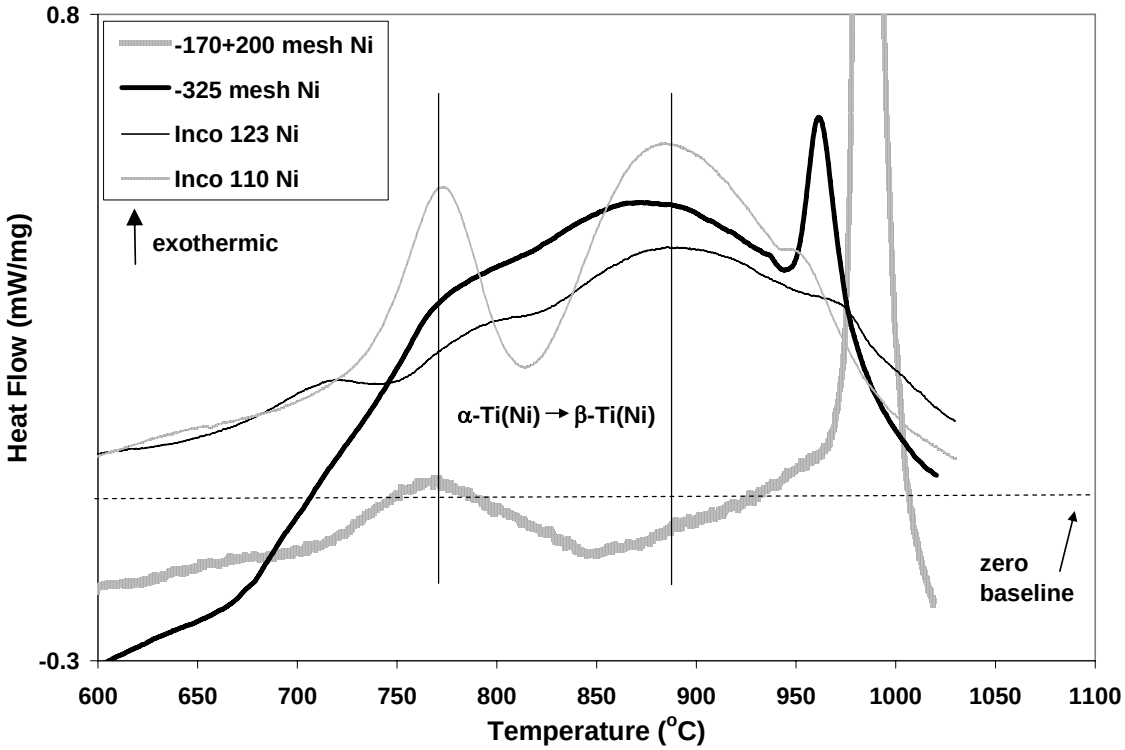

Figure 4-7: DSC heating curves showing changes in the observed exothermic intermetallic formation

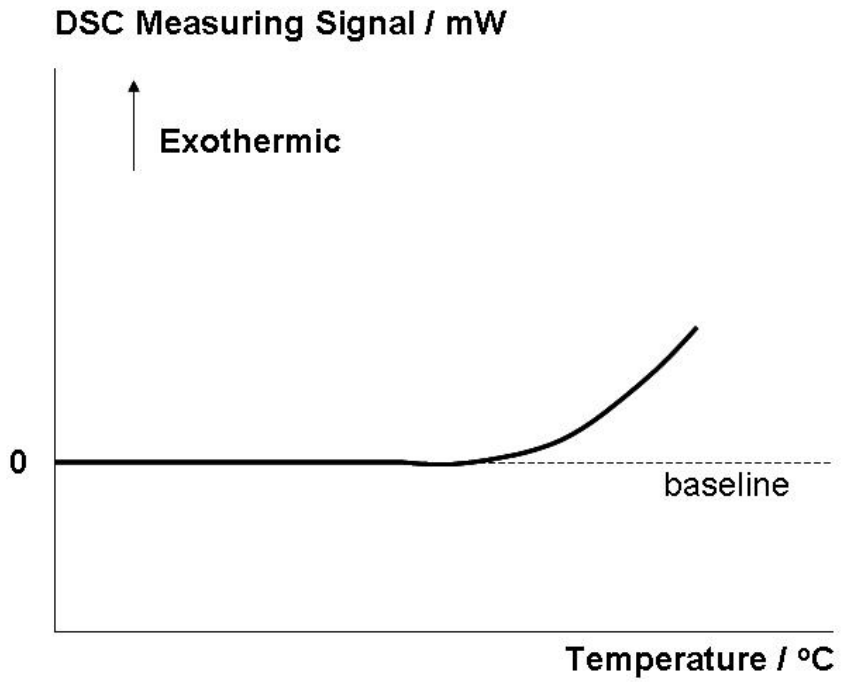

Figure 4-8: Schematic representation of an exothermic deviation due to intermetallic formation on a DSC thermal profile

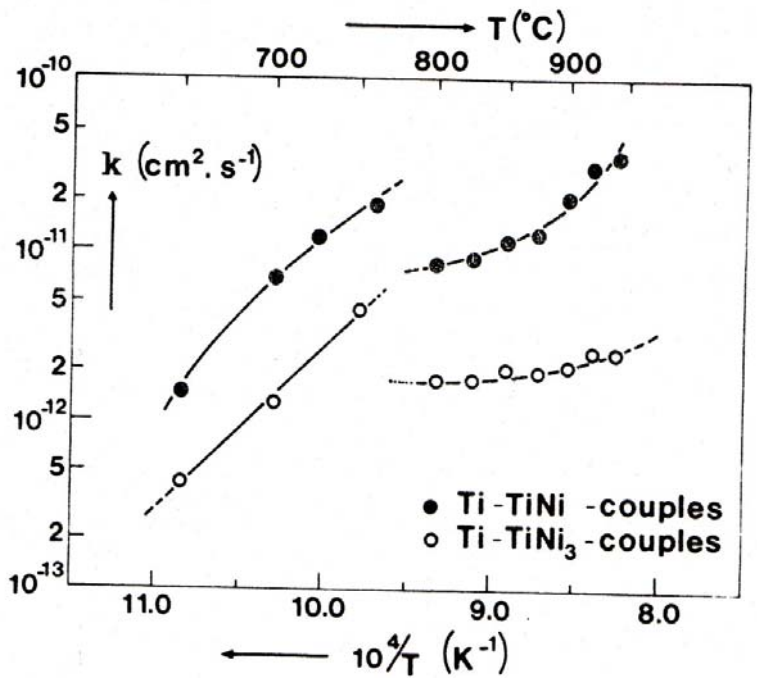

Figure 4-9: Plot of log *k* versus 1/*T* for the Ti_2Ni layer in Ti-TiNi and Ti-$TiNi_3$ diffusion couples **[66]**

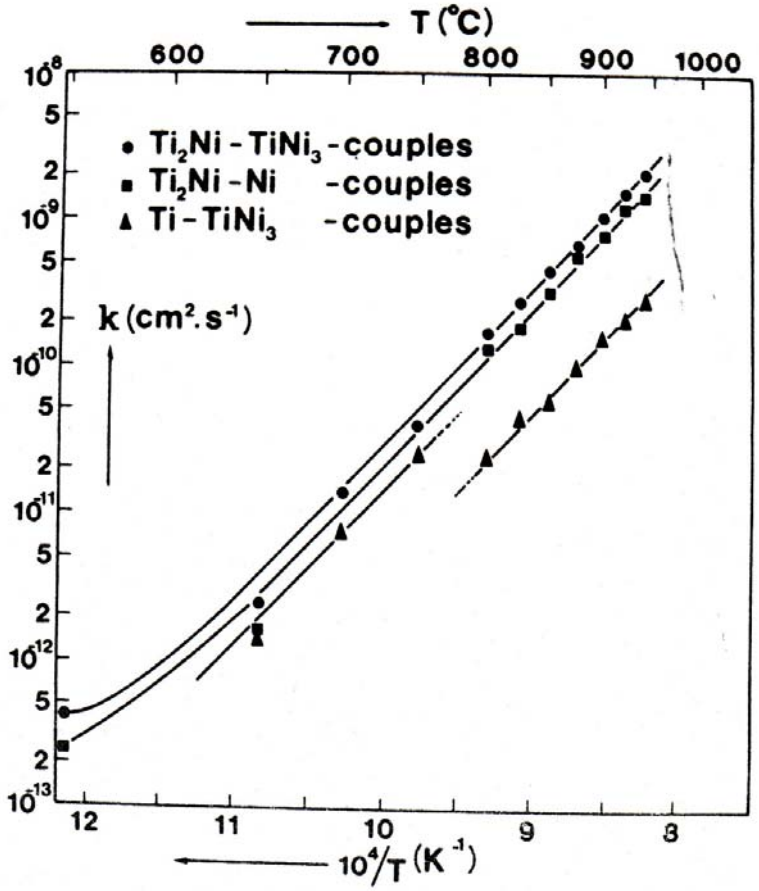

Figure 4-10: Plot of log *k* versus 1/*T* for the TiNi layer in various diffusion couples **[66]**

The Inconel 110 sample shows a definite endothermic peak during heating which onsets at 765^{o}C. Looking at the Ti-rich side of the Ni-Ti phase diagram, this corresponds to the temperature at which α-Ti(Ni) can begin to transform into β-Ti(Ni). This endothermic transformation appears over the temperature range of 765^{o}C to 883^{o}C. This same endothermic reaction is observed for the Inconel 123, -325 mesh, and -170+200 mesh Ni samples, however it is less apparent.

The effect of Ni powder size on the observed endotherm for α-Ti to β-Ti transformation can be explained conceptually using Figure 4-12. As the Ni powder size decreases, the overall surface area of contact between Ti and Ni increases. As the contact area between Ti and Ni increases, so does the interdiffusion between them. This is represented by the changing concentration profiles throughout the Ti surrounded by different sized Ni particles (Fig. 4-12 a to c). It should be noted that the presence of any intermetallic formation has been omitted from Figure 4-12 for the sake of clarity.

The minimal interdiffusion between Ti with coarse and medium Ni powders means that the α-Ti to β-Ti transformation observed on the DSC upon heating past 765^{o}C will be nominal. As a result, the concentration profiles that develop because of this slower interdiffusion will cause the α-Ti to gradually transform to β-Ti throughout the temperature range 765^{o}C to 883^{o}C. The greater amount of interdiffusion that occurs with finer powders, translates to more α-Ti present with a composition of 0.3wt% Ni at 765^{o}C. This will result in a much larger portion of Ti undergoing the α-Ti to β-Ti transformation once 765^{o}C is reached (as observed in Figure 4-8 for Inconel 110). Figure 4-13 shows

SEM microstructures for Inconel 110 Ni powder samples heated to a temperature a) below, and b) above 765^{o}C respectively. It is evident from the eutectoid structure of the Ti-rich cores in figure 4-13b that these cores must have been β-Ti at peak temperature.

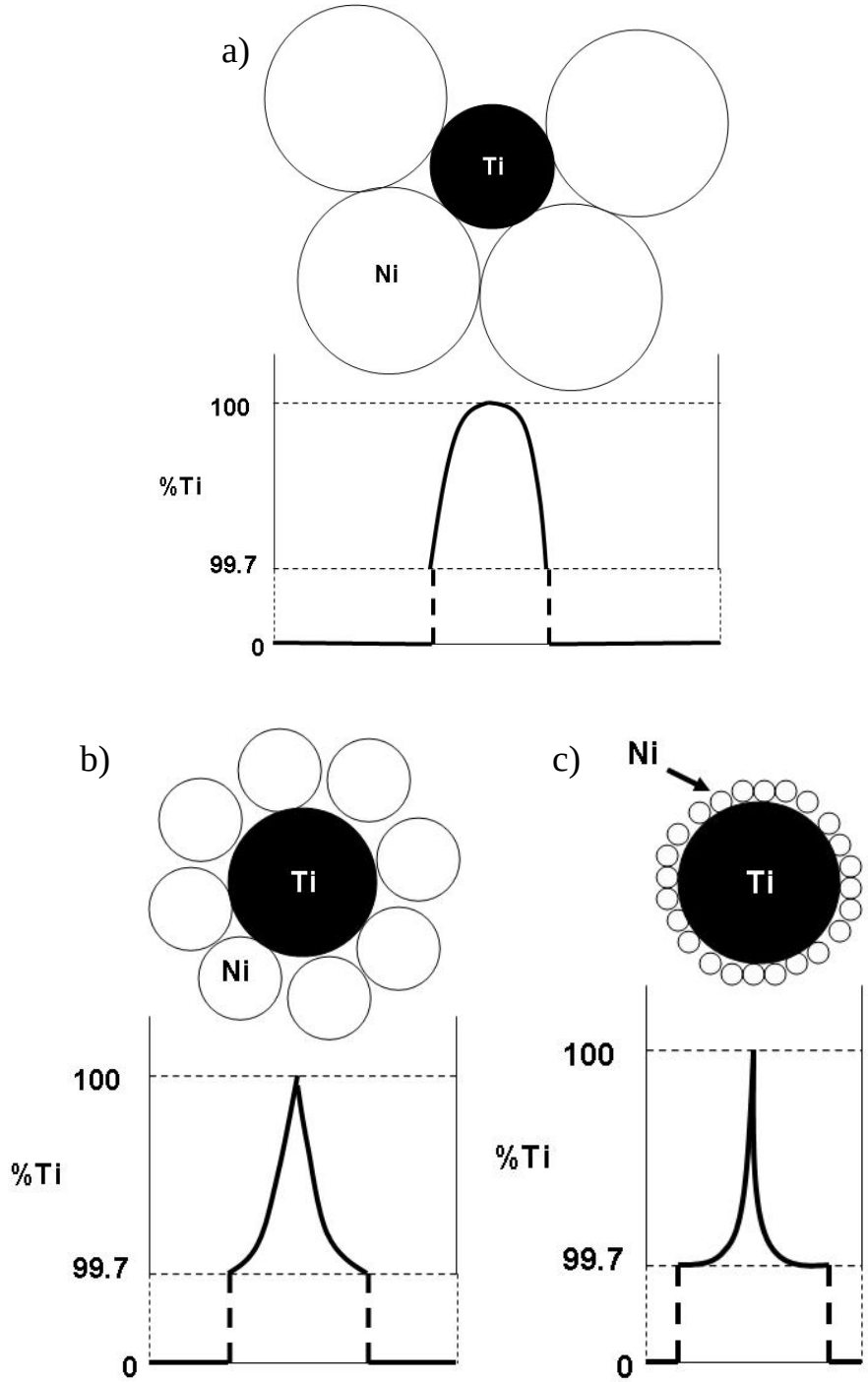

Figure 4-11: Schematic representation of concentration profiles throughout medium sized Ti surrounded by a) coarse Ni, b) medium Ni and c) fine Ni

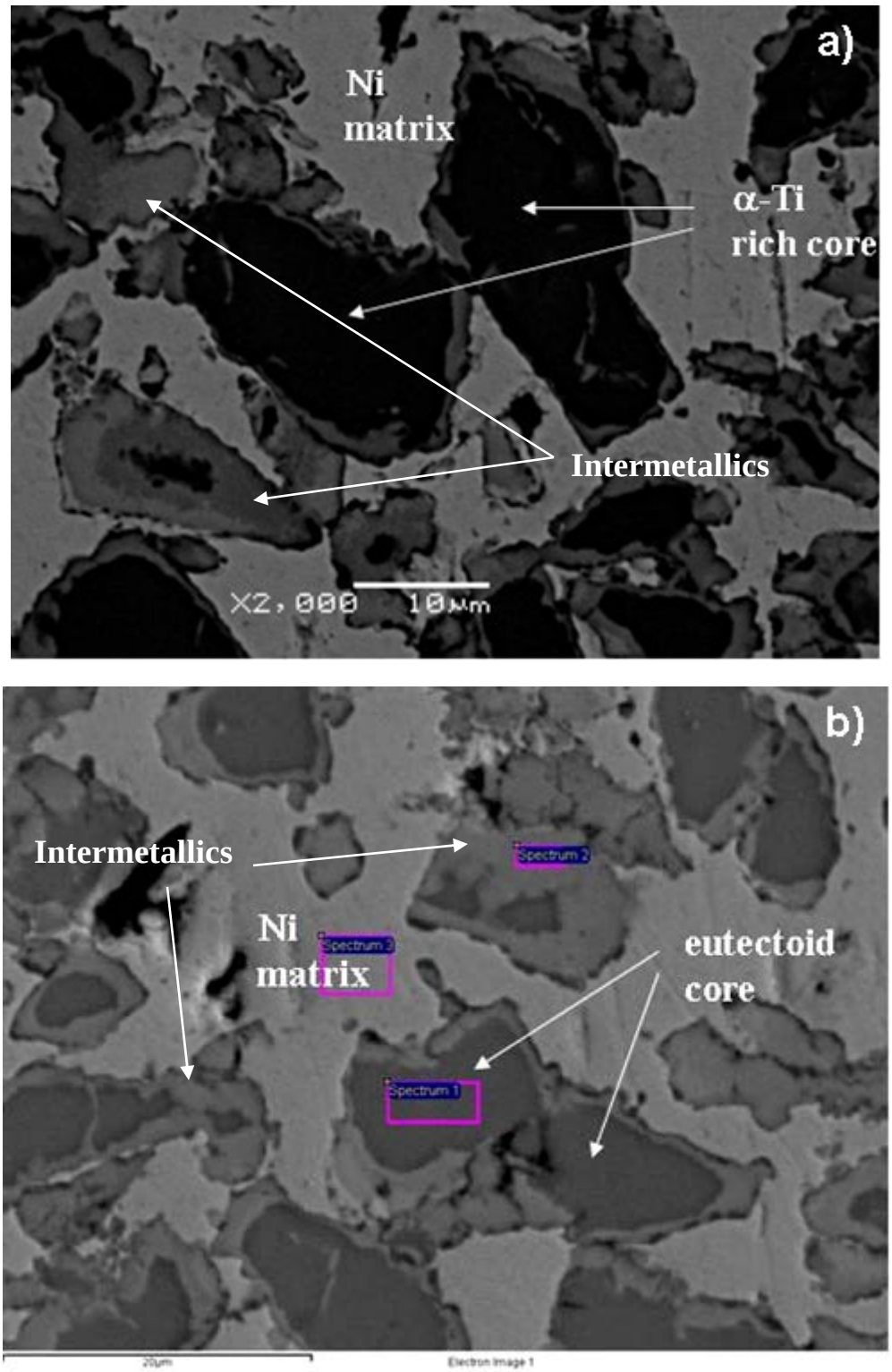

Figure 4-12: SEM backscatter image of Inco 110 Ni sample heated to a) T < 765°C, b) T > 765°C, and subsequently cooled

The endothermic thermal event observed to onset at 883°C during the heating of Ni and Ti powder mixtures (Figure 4-8) is the result of any remaining pure α-Ti transforming into β-Ti. This same transformation was observed during the heating of pure Ti powder (Figure 3-1). In the pure Ti, this transformation occurs over the temperature range 883°C to 950°C. Looking at the Ti-O phase diagram of Figure 4-14, it is observed that Oxygen is an alpha stabilizer in Ti. Therefore, even the slightest oxidation of the as-received powder can result in a dramatic increase in the observed temperature for α-Ti to β-Ti transformation.

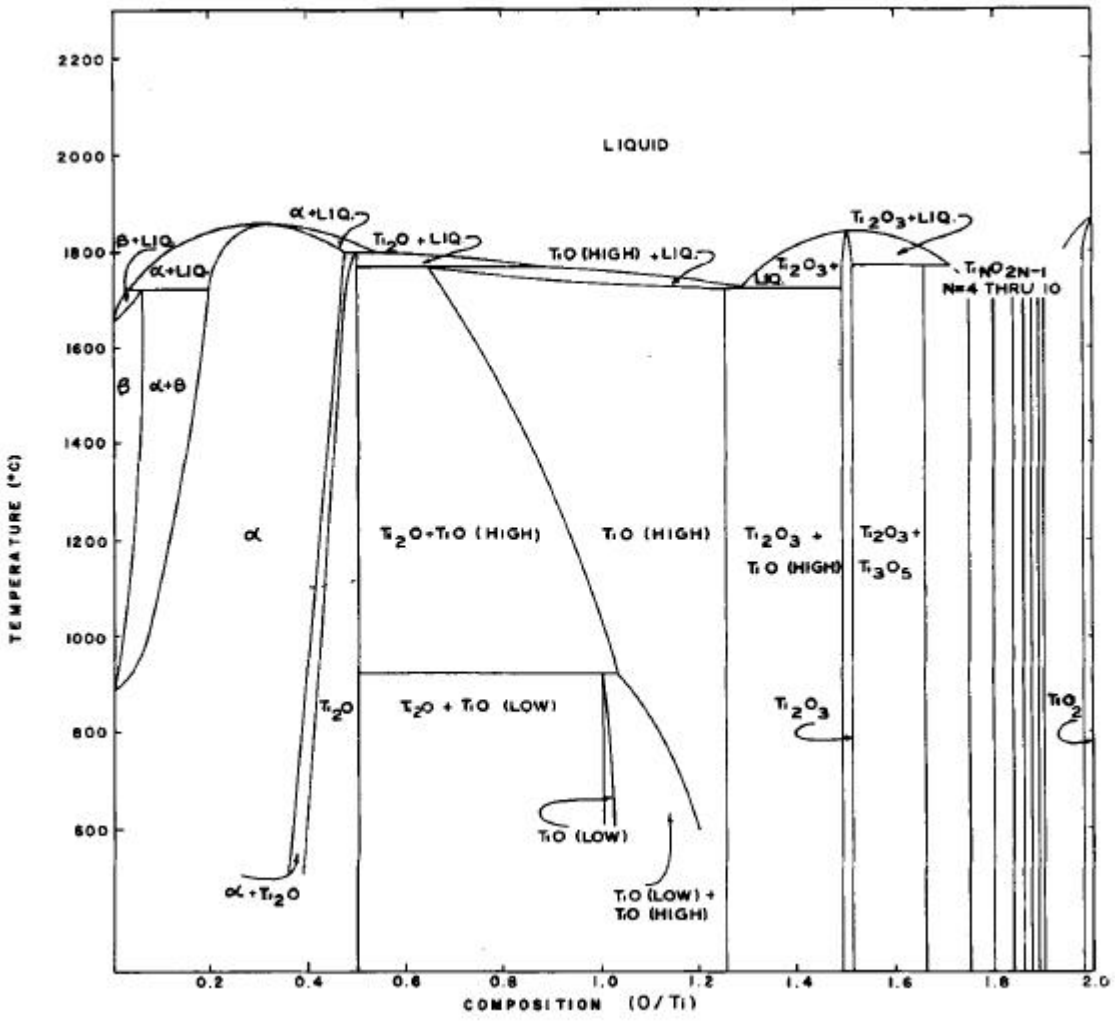

Figure 4-13: Ti-O phase diagram **[67]**

Considering the α-Ti to β-Ti transformation observed on the DSC for the starting Ti powder begins near 883°C, the Oxygen content of this powder must be minimal. Noting the transformation range observed (883°C to 950°C), it is estimated from Figure 4-14 that the Oxygen content of the starting Ti powder is less than 0.02wt%. It should be noted that the actual Oxygen content of the Ti powders used in this investigation was not measured to confirm this estimation.

It is uncertain why there is no observed transformation of any remaining pure Ti once 883°C is reached for the coarse Ni sample. Due to minimal interdiffusion that would result from this powder combination (as represented by Figure 4-12a), it is expected that this sample should show such a transformation once 883°C is reached.

4.3 Peak Temperatures 850°C, 950°C (Heating Conditions I, II)

For samples consisting of coarse Ni (-170+200 mesh) and medium Ti (-325 mesh) sintered according to heating conditions I and II, the respective DSC curves (Figures 3-8 & 3-11) show a number of exothermic events during cooling. These exothermic events are the result of the eutectoid decomposition of β-Ti present within the microstructure. The eutectoid decomposition of β-Ti into α-Ti and Ti_2Ni is observed for all samples sintered to 850°C and held for as long as 10 hours at peak temperature.

The conceptual unit cell of Figure 4-15 shows the concentration profile that develops through a Ti particle mixed with coarse Ni powder at 850°C (ignoring any intermetallic formation for the sake of clarity). Looking at the Ti-rich portion of the Ni/Ti phase

diagram (Figure 4-16), it is evident that heating to a peak temperature of 850°C can result in both α-Ti and β-Ti being present within the microstructure. Only the α-Ti possessing a Ni concentration above C_{s1} (according to Figure 4-15) will transform to β-Ti (C_{s2}) during sintering at 850°C. Therefore, only this fraction of Ti should undergo the eutectoid decomposition during cooling. This results in a microstructure that is a mixture of α-Ti and eutectoid regions (as evidenced in Figure 4-17). The concentration, C_{s3}, represents the maximum solubility of Ni in Ti at 850°C (~7at%).

If there was no alloying of Ni with Ti during sintering, then there would be no conversion of α-Ti to β-Ti at 850°C, and no eutectoid exotherm would be visible on the DSC during cooling.

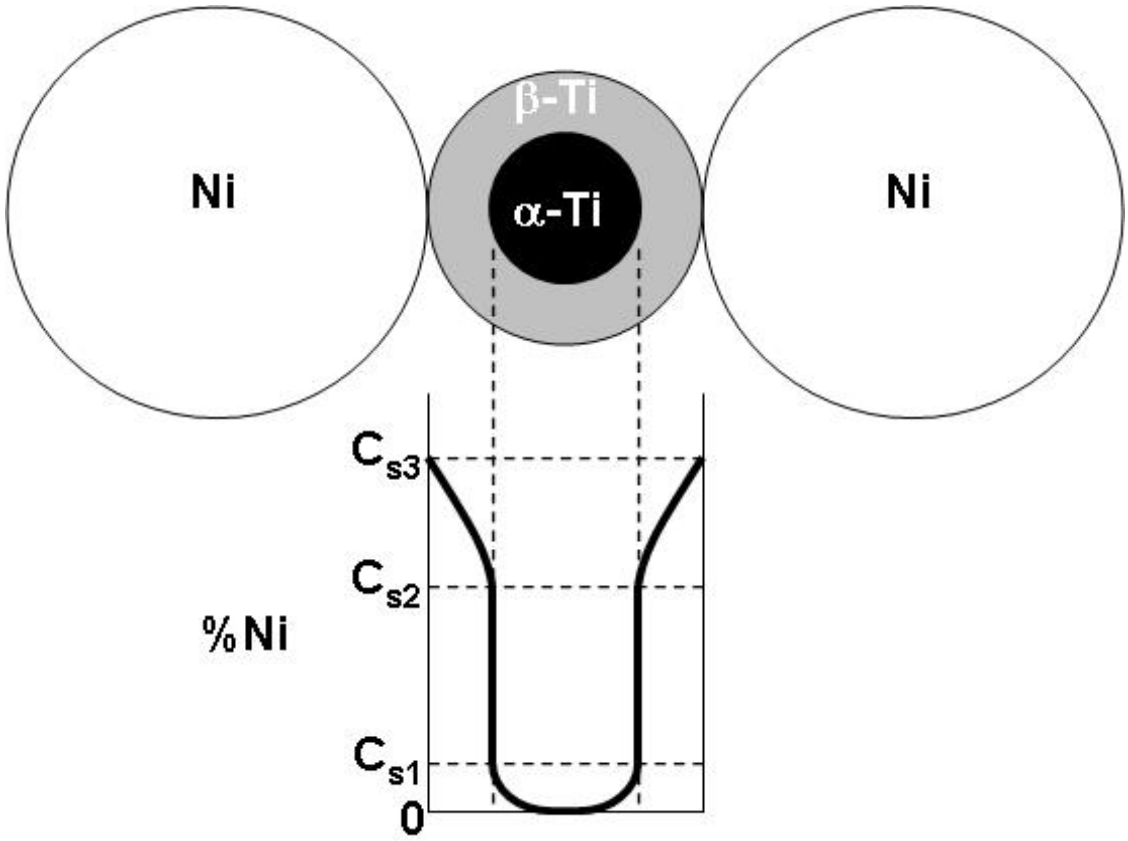

Figure 4-14: Concentration profile through Ti mixed with coarse Ni powder at 850°C

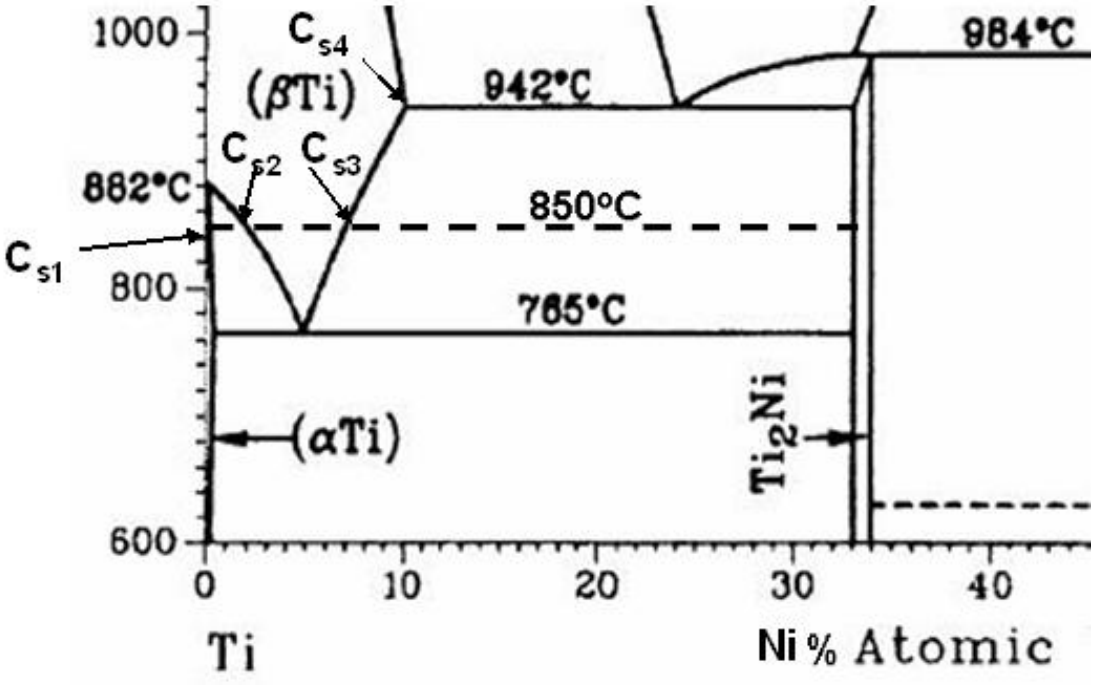

Figure 4-15: Titanium rich side of the Ni/Ti phase diagram **[1]**

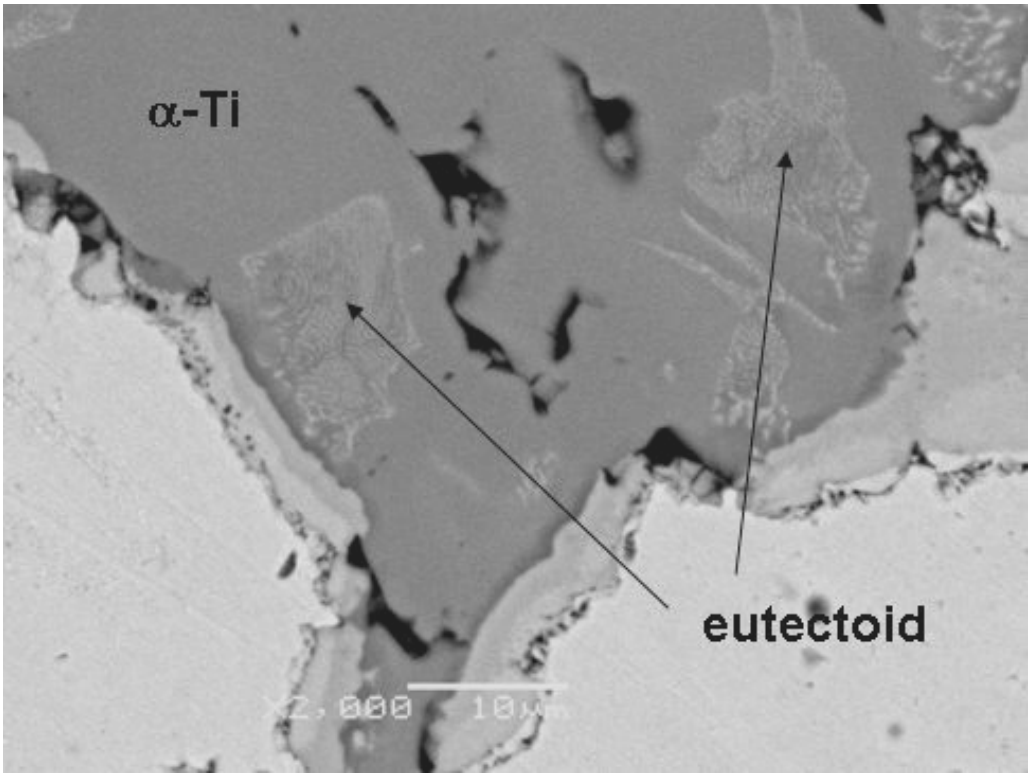

Figure 4-16: SEM backscatter image of Ti-rich matrix showing minimal eutectoid regions

For samples sintered to 950°C, all of the α-Ti will have transformed to β-Ti (as per the phase diagram), and can have a concentration profile according to Figure 4-18.

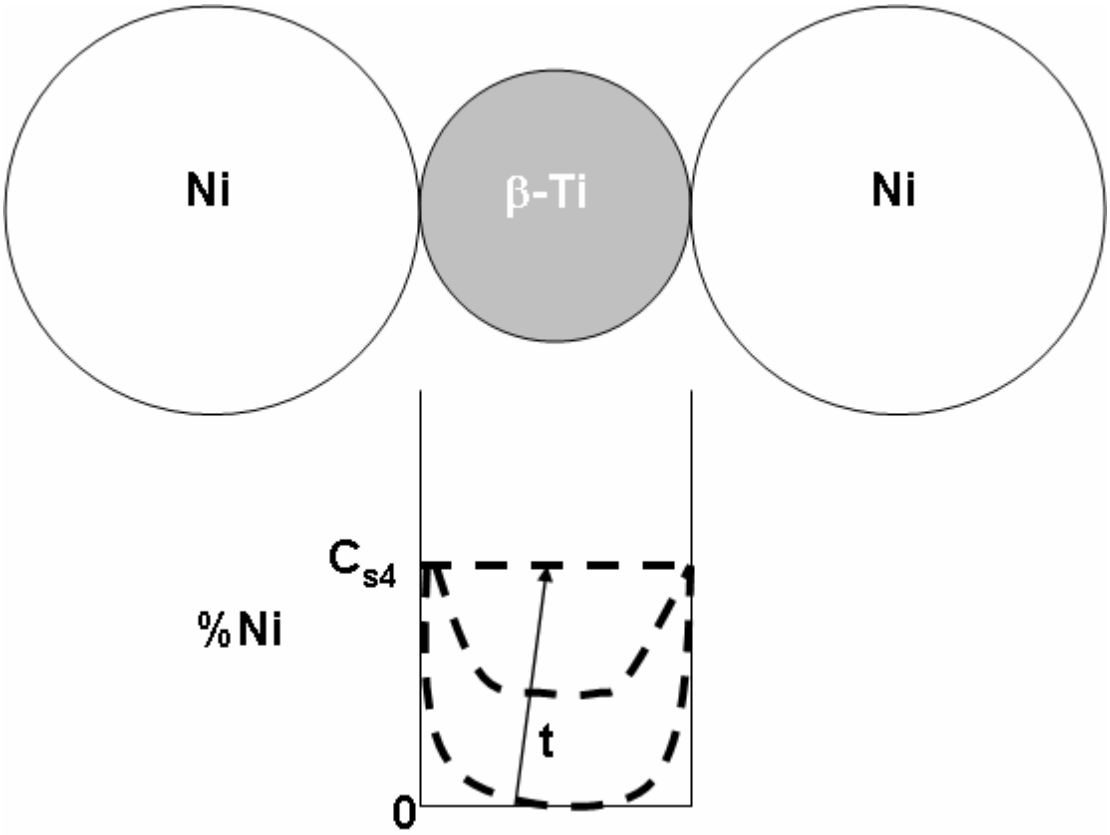

Figure 4-17: Concentration profile through Ti mixed with coarse Ni powder at 950°C

When the sintering time at 950°C is low, the concentration through the Ti will be akin to one of the dashed curved lines. Such a concentration profile will result in portions of Ti being hypo-eutectoid in composition, and portions being hyper-eutectoid. Any hypo-eutectoid regions can result in the nucleation of α-Ti regions before the eutectoid reaction takes place (as shown in Figure 4-19). With increased sintering time at 950°C, the Ni concentration through Ti will approach the solubility limit as predicted by the phase diagram, and the concentration profile will become a horizontal line of a single composition, C_{s4} (~10at%).

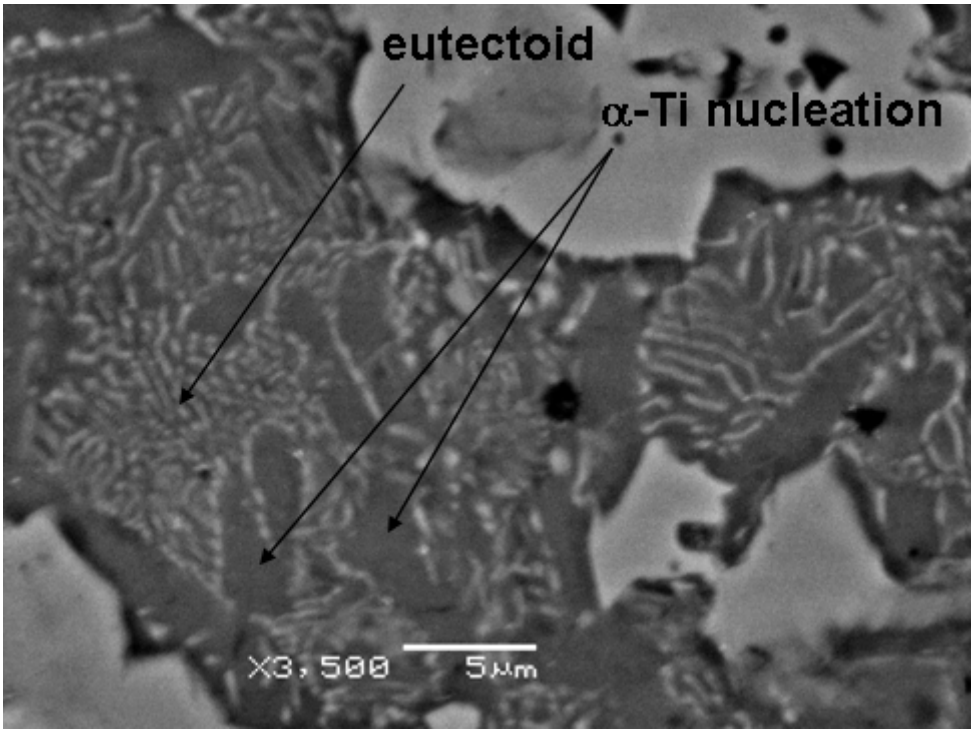

Figure 4-18: SEM backscatter image of a sample heated to 950°C and cooled, showing α-Ti nucleation

As shown in the DSC results of Figure 3-11, eutectoid decomposition reaction is observed for samples heated to 950°C, but only for samples held for 1 and 2 hours at peak temperature. This means that for the 5 and 10 hour hold samples sintered to 950°C, β-Ti must not have been present within the microstructure in any appreciable amount (see Figure 3-10b), as the eutectoid reaction would be observed during cooling on the DSC.

Porosity is evident in the microstructures of Figure 3-9 for samples sintered at 950°C for as little as 2 hours, and this porosity exists at the sites of the prior Ti-rich matrix. This can be attributed to dissolution of this Ti-rich matrix through the eutectic melting according to

$$(\beta - Ti) + Ti_2Ni \rightarrow L \qquad \textbf{(4-3)}$$

No melting is observed during the heating curves for samples sintered to 950°C; therefore this likely occurs during the hold segments at 950°C. It is unexpected that some eutectic melting does not occur (or is not detected in the DSC trace) immediately upon heating past 942°C. It is argued that this is due to the fact that eutectic melting requires a well developed equilibrium interface between (β-Ti) and Ti_2Ni. It is only after some hold time at 950°C that this occurs in the coarse Ni samples.

4.4 Peak Temperature of 1020°C (Heating Condition III)

Figure 3-3 highlights the effects of solid-state diffusion prior to ignition of the combustion reaction. This figure shows the variation due to powder size in the extent of the combustion reaction. As expected, the sample containing the coarsest Ni powder has the largest exotherm due to combustion, which results from less solid-state diffusion prior to ignition relative to samples with finer Ni powders. The DSC traces for samples containing both Inconel 123 and Inconel 110 Ni powder show virtually no combustion upon heating to 1020°C. This can be attributed to a lack of Ti-rich or Ni-rich regions present within the microstructure upon heating past the ignition temperature, which would be required to initiate and sustain the combustion reaction according to:

$$Ni + Ti \rightarrow NiTi \qquad 67 \text{ kJ/mol [28]} \qquad \textbf{(4-3)}$$

At the peak temperature of heating condition III (1020°C), both Ti_2Ni and Ti-rich β-Ti should be in the liquid state. The conceptual unit cell of Figure 4-20 shows the concentration profile attained throughout the liquid and remaining solid phases: TiNi,

$TiNi_3$ and (Ni). Any liquid that forms will wet existing solid surfaces throughout the microstructure, and as a result, any prior liquid rich regions within the microstructure will show up as porosity once the sample is cooled. Figure 3-12 shows evidence of the formation of such porous regions, as well as the higher magnification SEM image of Figure 4-21.

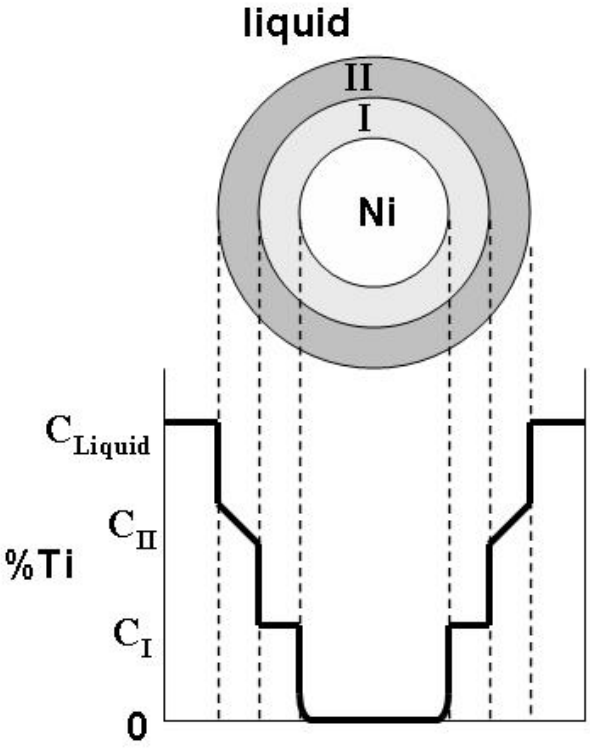

Figure 4-19: Concentration profile through a conceptual unit cell at 1020°C

The dashed curves of Figure 4-21 highlight where the existing solid surface would have been located after liquid formation. The Ti-rich liquid will have wet the solid surfaces and promoted Ni dissolution from the solid phase in contact with the liquid. From the phase diagram, it can be determined that the solid phase in contact with the liquid will be TiNi. As can be seen from Figure 4-21, liquid motion (and subsequent solidification) causes the formation of large scale porosity.

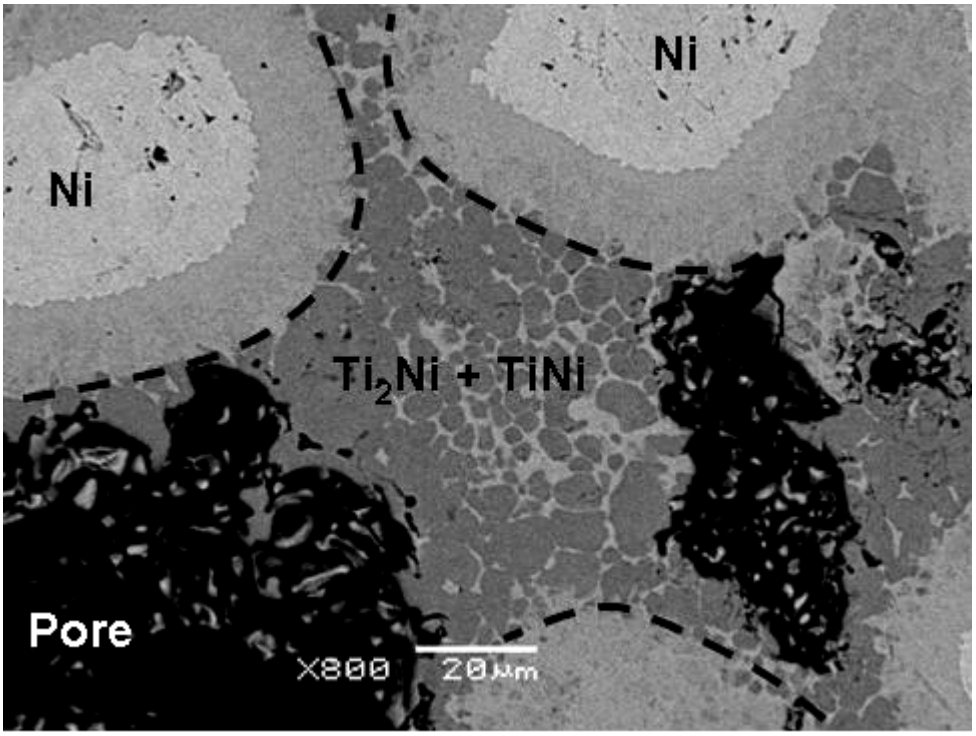

Figure 4-20: High magnification SEM backscatter image of a coarse Ni sample heated to 1020°C and cooled

This Ni dissolution will enrich the liquid phase, raising its bulk composition such that it falls above the two-phase region of Ti_2Ni and TiNi in the phase diagram. As a result, when cooling through this two-phase region, the TiNi intermetallic will nucleate at the existing TiNi/liquid interface, and in any Ni rich liquid regions. This will cause the bulk composition of the remaining liquid to become richer in Ti until 984°C is reached. According to the equilibrium phase diagram, this is the temperature at which Ti_2Ni can solidify according to the peritectic reaction:

$$TiNi + L \rightarrow Ti_2Ni \qquad \textbf{(4-4)}$$

From the DSC results (Figure 3-12), it can be seen that Ti_2Ni nucleation/solidification actually occurs at a temperature below 984°C. The reason for this observed undercooling

is that there is not any pre-existing solid phase Ti_2Ni to act as a nucleation site for further Ti_2Ni to solidify. If there was, solidification would have taken place as soon as 984^oC was reached.

4.5 Effect of Hold Time at 900^{o}C (Heating Condition IV)

As mentioned in the experimental results, it was desired to study the transient nature of the eutectoid reaction using a coarse Ti powder, so as to develop a correlation between microstructural evolution and the observed DSC thermal behaviour of this reaction. Figure 4-22 shows a conceptual unit cell before cooling from 900^oC for a coarse Ti particle surrounded by the different intermetallic phases and Ni. Both TiNi and $TiNi_3$ intermetallics have been grouped into one single phase for sake of clarity in this figure. C_β represents the Ti concentration at the maximum solid solubility of Ni at 900^oC (Figure 4-23).

Since the peak sintering temperature is above 765^oC, it is possible for the sample to undergo the eutectoid reaction upon cooling (which is just the reverse reaction of Eqn 4-2):

$$\beta - Ti \rightarrow \alpha - Ti + Ti_2Ni \qquad \textbf{(4-5)}$$

As aforementioned, the reason for the occurrence of this reaction has to do with the fact that at a temperature of 765^oC, β-Ti decomposes into α-Ti and the Ti_2Ni intermetallic. This reversion of β-Ti to α-Ti is the result of an allotropic transformation, whereby high temperature FCC Titanium allotropically transforms to low temperature HCP Titanium. Since the maximum solid solubility of Nickel in α-Ti is significantly smaller (<1 at%)

than that of β-Ti at the eutectoid temperature (~5 at%), the HCP Titanium can no longer accommodate Nickel atoms within its lattice structure to the same extent as FCC Titanium. This excess of Nickel atoms is removed by way of the co-precipitation of two new phases. This process will leave a eutectoid microconstituent that consists of a mixture of α-Ti, and the precipitated phase Ti_2Ni; evidenced on the right side of Figure 4-24.

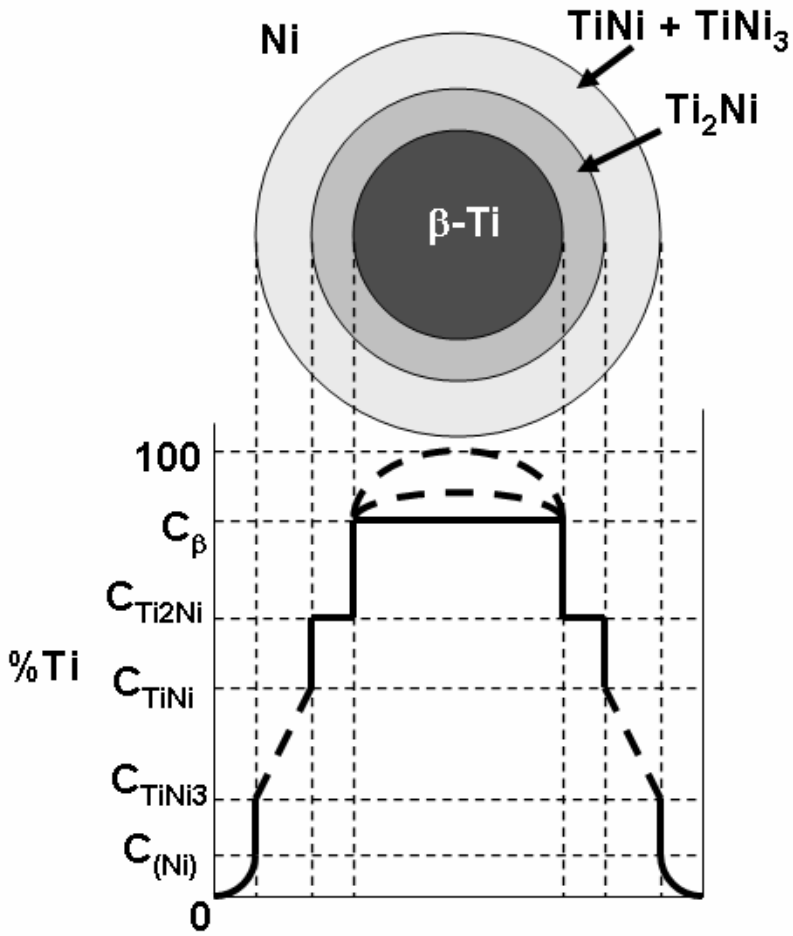

Figure 4-21: Conceptual unit cell of a b-Ti core surrounded by the equilibrium phases of the Ni/Ti system at 900°C

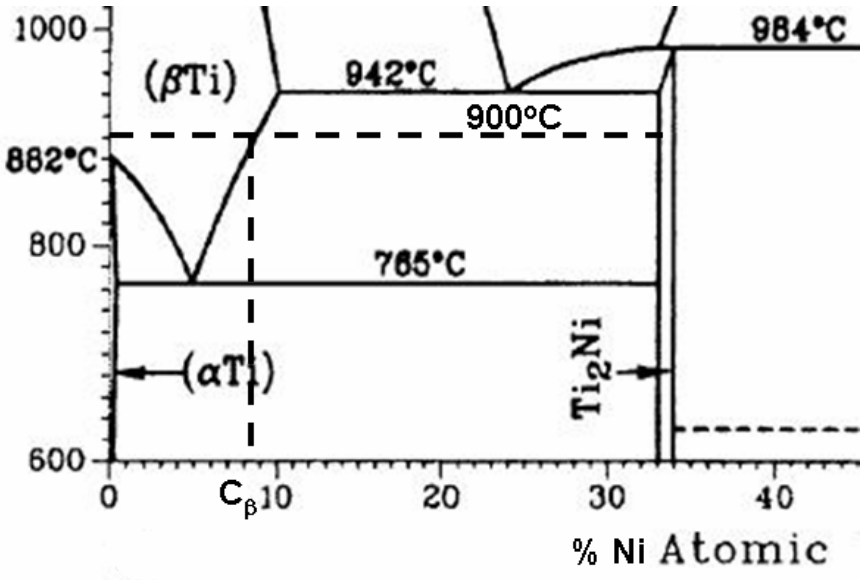

Figure 4-22: Ti-rich side of phase diagram at 900°C [1]

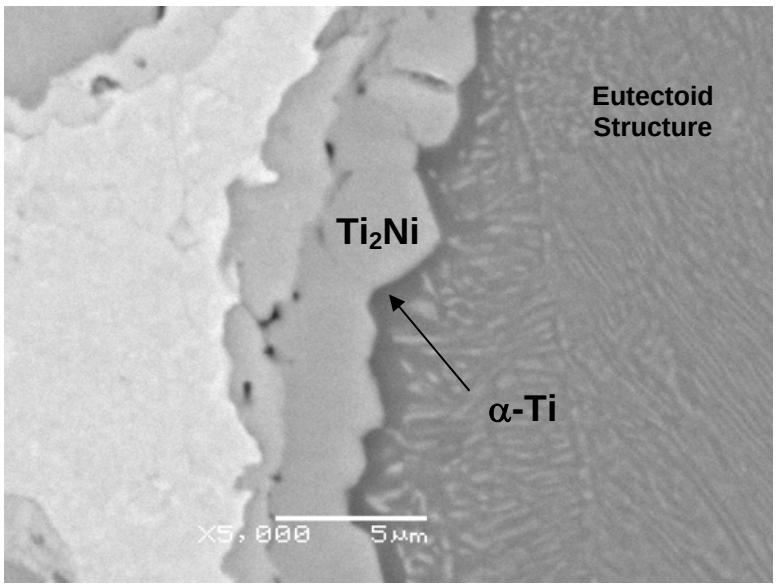

Figure 4-23: SEM backscatter image of a microstructure showing the eutectoid structure in a Ti particle

On the DSC, this exothermic reaction was observed to occur at temperatures between 720-750°C. The difference between the observed and theoretical temperatures for this reaction can be attributed to undercooling. Similar to the pearlite reaction, it can be seen that the nucleation of the eutectoid structure requires the establishment of cooperative growth of the two phases [44], in this case α-Ti and Ti_2Ni. In general, for a eutectoid

reaction to proceed on an existing hyper-eutectoid interface, a hypo-eutectoid phase must first form to allow for cooperative growth between the two eutectoid phases. Figure 4-25 shows the nucleation of a hypo-eutectoid phase (black) on an existing hyper-eutectoid interface (white). If there is no α-Ti present at the existing Ti_2Ni interface, then it must nucleate at this interface before cooperative growth of α-Ti and Ti_2Ni can occur. Looking at the microstructure of Figure 4-24, a dark region of α-Ti is observed to have nucleated along the Ti_2Ni interface. It is the nucleation of this α-Ti that causes the observed undercooling of the eutectoid reaction on the DSC cooling curves.

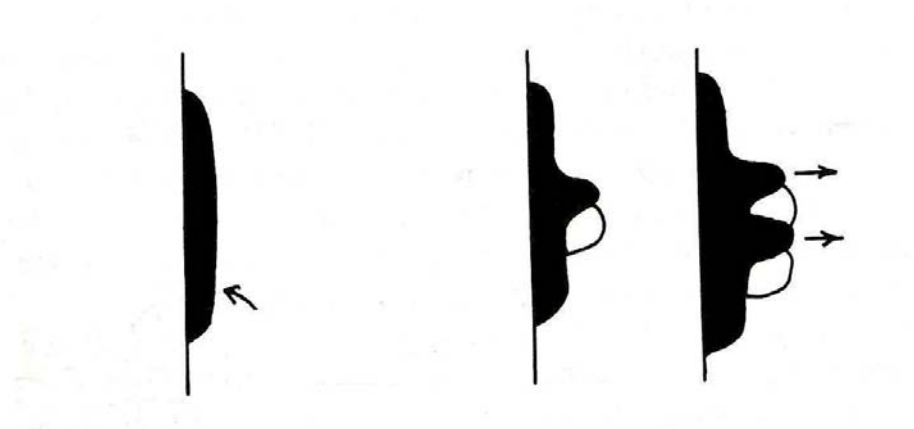

Figure 4-24: Schematic representation of hypoeutectoid phase nucleation before eutectoid reaction can proceed **[14]**

In studying the eutectoid reaction to greater extent using DSC, the effects of hold time on the measured enthalpy of this reaction (Table 3-2) were deduced. From the data of Table 3-2, a plot of measured enthalpy of eutectoid reaction versus hold time is constructed (Figure 4-26). From this plot, an inversely proportional relationship is observed between hold time at 900^{o}C, and measured enthalpy of the eutectoid reaction. This makes sense, as increased sintering time at peak temperature will allow more time for the diffusional

growth of the phases present within the microstructure (Ti_2Ni, TiNi and $TiNi_3$). The growth of these phases will consume the β-Ti in the microstructure while holding at peak temperature, which will affect the amount of β-Ti present that can undergo the eutectoid reaction. Also shown in Figure 4-26 is the eutectoid enthalpy data obtained for the coarse Ni samples heated to 850°C and 950°C (according to Table 3-1). As can be seen, when the peak sintering temperature is above 883°C such that only β-Ti will be present during the hold segment, the trend obtained in the β-Ti removal for 900°C and 950°C are similar. However, for the 850°C sample, which represents the case when α-Ti may also be present in the microstructure during the hold segment, the trend obtained is quite different, and indicates and optimum time to maximize the amount of β-Ti in the microstructure (as evidenced by the eutectoid enthalpies observed for this sample upon cooling).

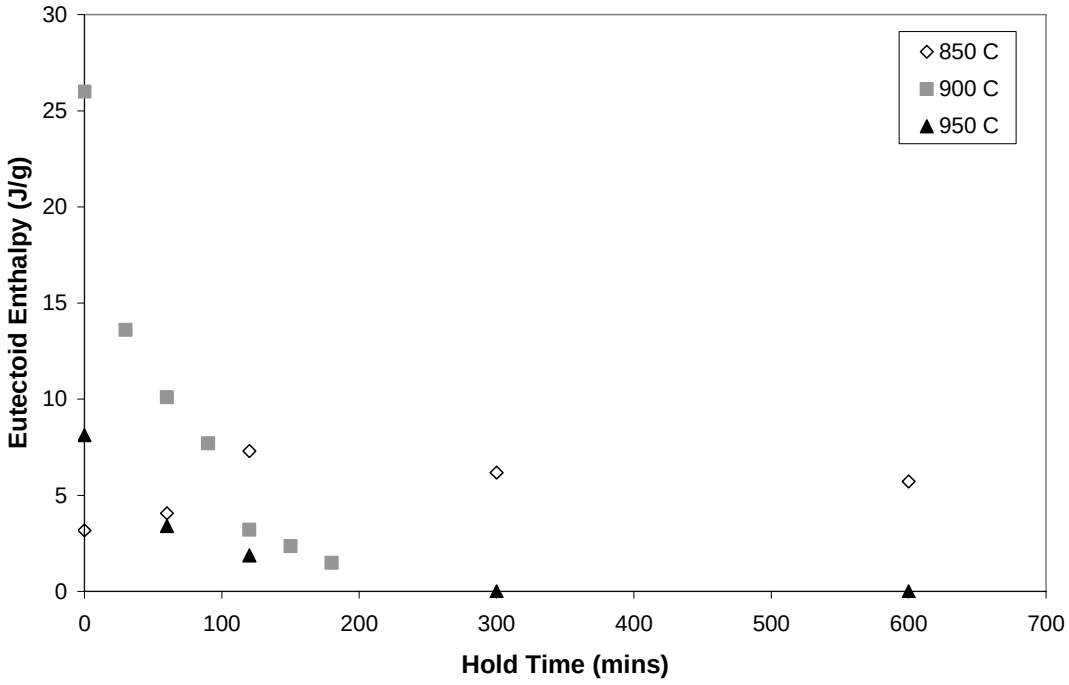

Figure 4-25: Measured eutectoid enthalpy versus hold time at 900°C for coarse Ti samples, and at 850°C and 950°C for medium Ti samples

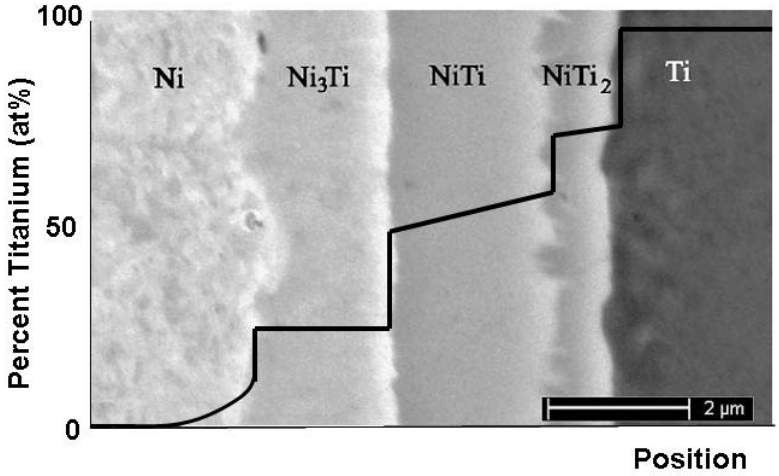

Figure 4-26: Representative Ni-Ti diffusion couple with overlaid concentration profile **[41]**

From the Ni-Ti phase diagram, it is evident that any β-Ti present within the microstructure should be in contact with the Ti_2Ni intermetallic. To understand how the growth of the Ti_2Ni phase can consume β-Ti with increased sintering time, the motion of the Ti_2Ni/β-Ti interface is examined. The concentration profile across the representative diffusion couple of Figure 4-27 can aid in determining the instantaneous Ti_2Ni/β-Ti interface velocity, which will give an indication as to the mobility of the interface. From the equation for instantaneous interface velocity given by [44], the instantaneous velocity of the Ti_2Ni/β-Ti interface can be represented as:

$$v_{\mathrm{Ti_2Ni}/\beta-\mathrm{Ti}} = \frac{1}{C_{\beta-Ti} - C_{\mathrm{Ti_2Ni}}}\left\{ D(\mathrm{Ti_2Ni})\frac{\partial C_{\mathrm{Ti_2Ni}}}{\partial x} - D(\beta - Ti)\frac{\partial C_{\beta-Ti}}{\partial x} \right\} \qquad \textbf{(4-6)}$$

If the concentration profile across the β-Ti is uniform, then the concentration gradient term of the β-Ti phase tends to zero. In addition, since $C_{\beta\text{-Ti}} > C_{Ti2Ni}$, the instantaneous interface velocity equation will be a positive quantity. This indicates that the mobility of

the Ti_2Ni/β-Ti interface tends to the right (into the β-Ti phase). With this simple analysis, it is shown that the Ti_2Ni phase will indeed consume the β-Ti phase with prolonged sintering time. This result, of course, hinges on the assumption that the concentration profile across the β-Ti is uniform during sintering. Looking at the plot of Ni concentration across two different Ti particles sintered at 900°C for 0 and 60 minutes (Figure 4-28), it can be seen that the composition remains fairly uniform across the particle. Moreover, since a relatively uniform composition is reached across the Ti particle even with no hold time at peak sintering temperature, it can be concluded that the diffusion of Nickel into the β-Ti is fast enough to attain the bulk composition as predicted by the phase diagram in short time. Analysis of the diffusivity of Ni in β-Ti solid solutions supports this conclusion (Figure 4-29). In this analysis, it is shown that Ni diffusion in β-Ti is faster than even the self diffusion of Ti.

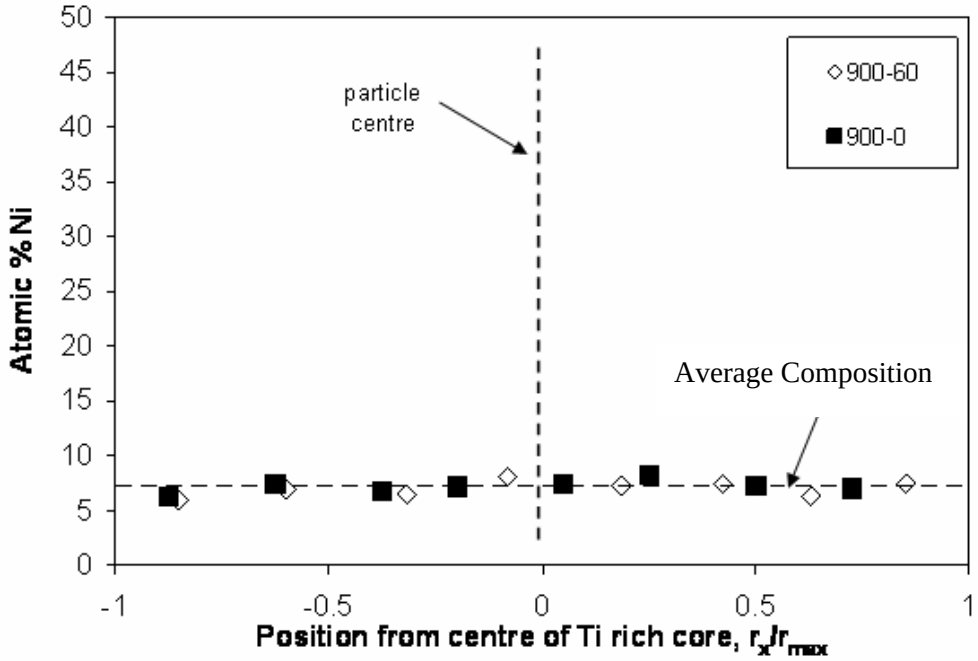

Figure 4-27: EDS composition profile across Ti-rich cores from samples heated to and held at 900°C for 0 and 60 minutes and then cooled to room temperature

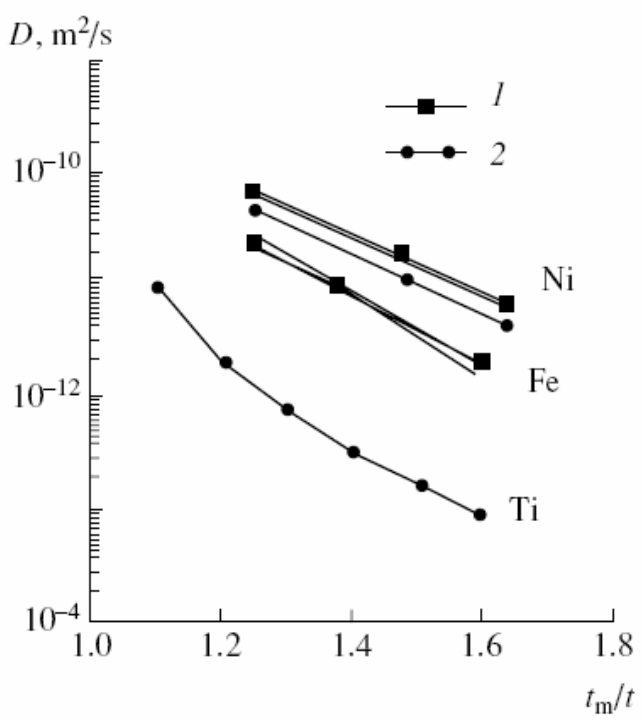

Figure 4-28: Diffusivity as a function of temperature for Fe and Ni diffusion in Ti and Ti self-diffusion (t_m is the melting temperature of Ti): (1) Shevchuk [68], (2) earlier results**.**

Using optical microscopy and Image Pro 4.0 image analysis software, the area fraction of eutectoid phase corresponding to each hold time at 900°C was measured. Combining the eutectoid enthalpy data with the area fraction of eutectoid phase measured for samples held at 900°C for varying time (Table 4-1), a plot of eutectoid area fraction versus enthalpy can be constructed (Figure 4-30).

Table 4-1: Measured eutectoid enthalpy and area fraction for each corresponding hold time at 900°C

Time at 900°C (min)	**Eutectoid Enthalpy** (J/g)	**Eutectoid Area Fraction**
0	26	0.399
30	13.6	0.205
60	10.1	0.166
90	7.7	0.114
120	3.2	0.057
150	2.35	0.041
180	1.48	0.028

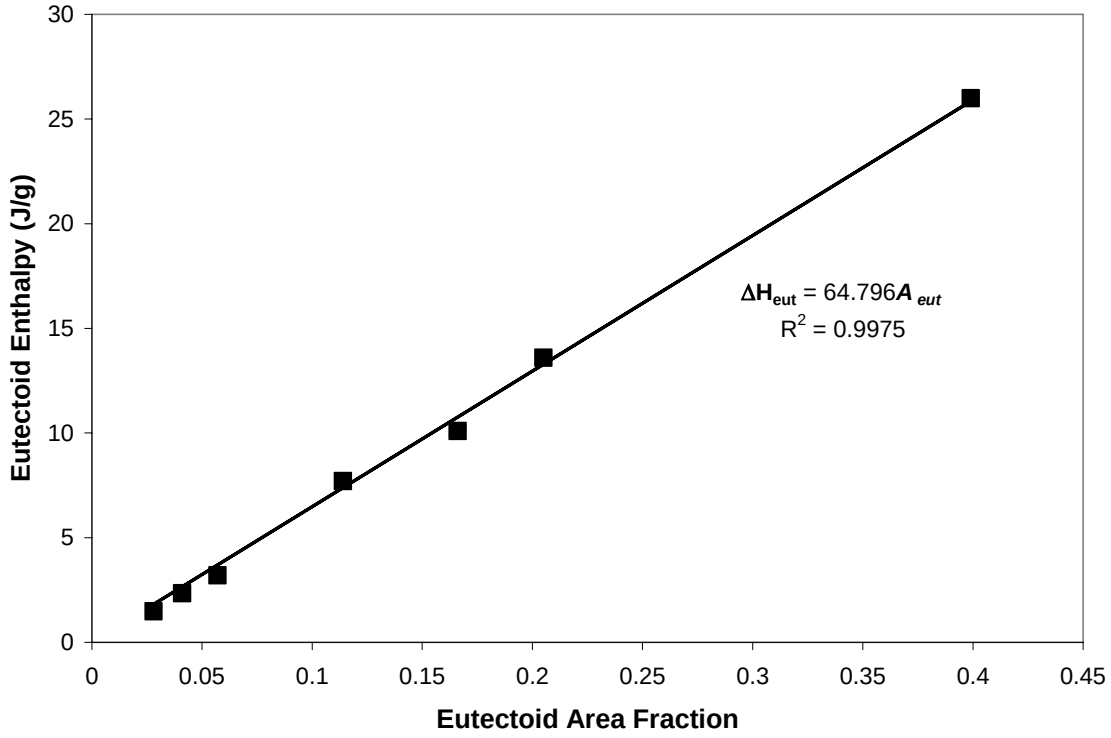

Figure 4-29: Enthalpy of eutectoid reaction versus measured eutectoid area fraction

A linear trend between is observed between eutectoid enthalpy (ΔH_{eut}) to measured eutectoid area fraction (A_{eut}), and from this trend, the following trend line equation can be developed through linear regression:

$$\Delta H_{eut} = 64.796 A_{eut} \quad \textbf{(4-7)}$$

According to the above equation, if the entire sample were to undergo the eutectoid reaction, which corresponds to a value of A_{eut} = 1, then the measured enthalpy for this reaction would be ΔH_f = 64.8 J/g. Knowing this, it is possible to determine the weight fraction that has undergone the eutectoid reaction for any sample:

$$f_{eut} = \frac{\Delta H_{eut}}{\Delta H_f} \quad \textbf{(4-8)}$$

This is an important result, as it allows for the determination of the quantity of β-Ti present within the microstructure during sintering at 900^{o}C, through quantitative analysis

of the eutectoid reaction using DSC. It must be assumed that the eutectoid and T_2Ni phases, derived from the hypereutectoid transformations of β-Ti during cooling from 900 °C, are present according to their fractions calculated using tie line and lever rule calculations from the equilibrium phase diagram. In this case, the fraction of β-Ti equals;

$$f_{\beta-Ti} = \left[\frac{\left(X_{Ti_2Ni} - X_{eut}\right)}{\left(X_{Ti_2Ni} - X_{\beta-Ti}\right)} \right] f_{eut} \qquad \textbf{(4-9)}$$

where $f_{\beta-Ti}$ and f_{eut} are the weight fractions of the β-Ti and eutectoid phases respectively and X_{Ti2Ni}, X_{eut} and $X_{\beta-Ti}$ are the concentrations of Ni (in wt. %) in the Ti_2Ni, eutectoid, and β-Ti phases respectively. Figure 4-31 shows the results obtained from calculating the weight fraction of β-Ti from the weight fractions of eutectoid reaction, and plotting this versus hold time at 900°C. It can be seen that the β-Ti phase is removed from the microstructure in an approximately parabolic rate. When the data is re-plotted as a function of the square root of time (Figure 4-32), it is clear that the β-Ti removal follows a two stage parabolic decay. In both stages the correlation coefficient is $R^2 = 0.99$. The rate constant for stage I is $k_I = -0.0347\ f_\beta / (mins)^{1/2}$ and that for stage II is $k_{II} = -0.0123\ f_\beta / (mins)^{1/2}$ This two stage process can be understood by referring back to the microstructures of Figure 3-15. While the coarse Ti particles have a relatively narrow size distribution they are not monosized spheres. As a result, the removal of the β-Ti cores will be more rapid in smaller particles than in larger ones. After 120 minutes at 900°C, Figure 3-15c indicates that only the largest Ti particles have residual β-Ti at their core. The slower kinetics indicated in Figure 4-32 at times greater than 120 minutes are a result of the presence of large Ti particles in the powder compact.

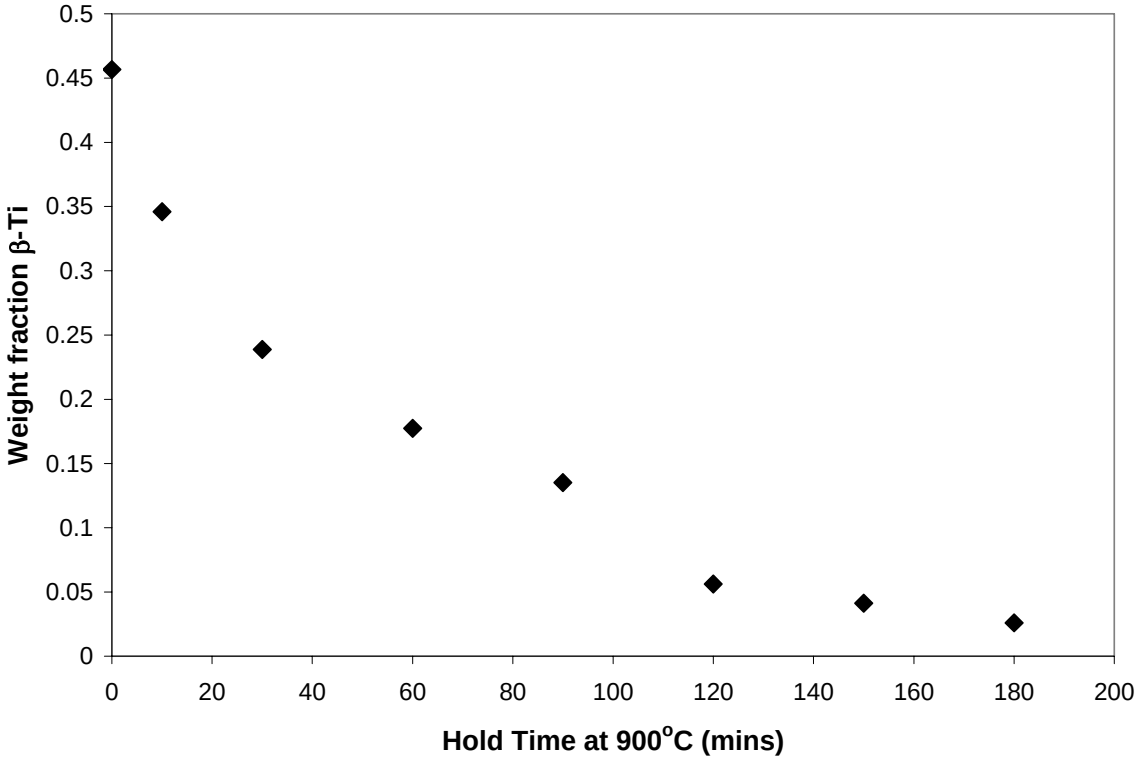

Figure 4-30: Weight fraction β-Ti versus hold time at 900°C

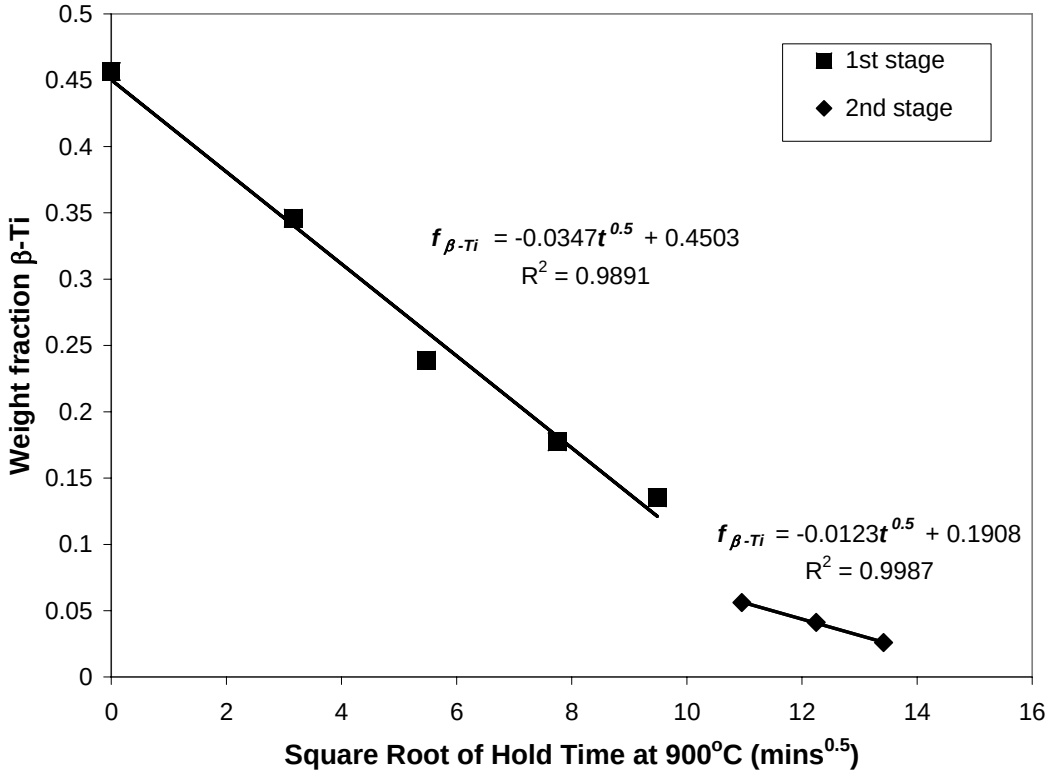

Figure 4-31: Weight fraction β-Ti versus square root of hold time at 900°C

4.6 Growth of Ti_2Ni During Cooling

As indicated in Figure 4-28, the overall bulk composition of the Titanium particles is above that of the eutectoid composition (>5 at%), even with no hold time at 900°C. This is attributed to the relatively fast diffusion of Ni in β-Ti (Figure 4-22), and indicates that the Ti particles quickly achieve a Ni composition according to what the phase diagram predicts at 900°C (~7-8 at% Ni). Since the composition of the Titanium particles is hypereutectoid, Ti_2Ni should begin to grow immediately upon cooling from peak sintering temperature. This is evidenced by the DSC cooling curves of Figure 4-33.

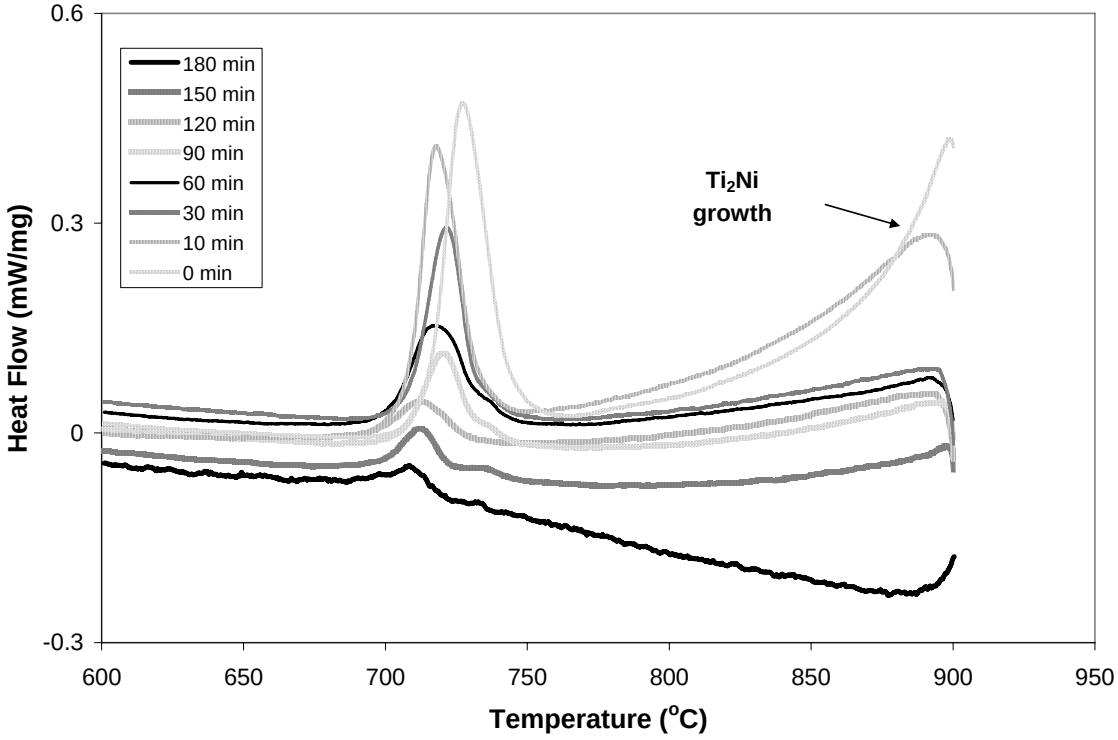

Figure 4-32: DSC cooling curves showing Ti_2Ni nucleation immediately upon cooling from 900 °C

It can be seen immediately upon cooling, that an exothermic peak is observed which gradually diminishes until the eutectoid reaction initiates. This peak represents the nucleation of the Ti_2Ni intermetallic, which occurs immediately upon cooling. Since there is already Ti_2Ni present within the microstructure in contact with β-Ti, there is no

need for undercooling to initiate this reaction, as Ti_2Ni can grow on the existing Ti_2Ni/β-Ti interface.

Since a relationship between the weight fractions of β-Ti and eutectoid (Eq. 4-9) is known, it is possible to determine the weight fraction of Ti_2Ni that has epitaxially grown during cooling from 900°C until the eutectoid temperature. This growth of Ti_2Ni is explained schematically in Figure 4-34 and 4-35, which shows the concentration profile across a Titanium particle at 900°C, and after the eutectoid reaction has occurred. Figure 4-27 represents the case when a β-Ti core is surrounded by Ti_2Ni at 900°C. The concentration profile in this case shows the β-Ti composition to be uniform across the Ti particle at the maximum solid solubility of Ni in β-Ti as predicted by the Ni-Ti phase diagram at a temperature of 900°C. This uniformity in Ni composition throughout the Ti particles results from the fast diffusion of Ni in β-Ti. While cooling into the hypereutectoid two-phase region from 900°C to below the eutectoid reaction temperature; the Ti_2Ni will grow into the β-Ti as predicted by the instantaneous interface velocity of equation (4-6). The dashed circle in the Ti_2Ni phase of Figure 4-35 represents the original Ti_2Ni/β-Ti interface before cooling from 900°C. The quantity of Ti_2Ni that grows epitaxially as a result of cooling into the two-phase region is represented by the region between the dashed circle and the α-Ti, which is represented by the black circle. Thus, the α-Ti that nucleates at the present Ti_2Ni/β-Ti interface does so to allow for cooperative growth between the two eutectoid phases. The nucleation of this α-Ti causes the observed undercooling of the eutectoid reaction on the DSC.

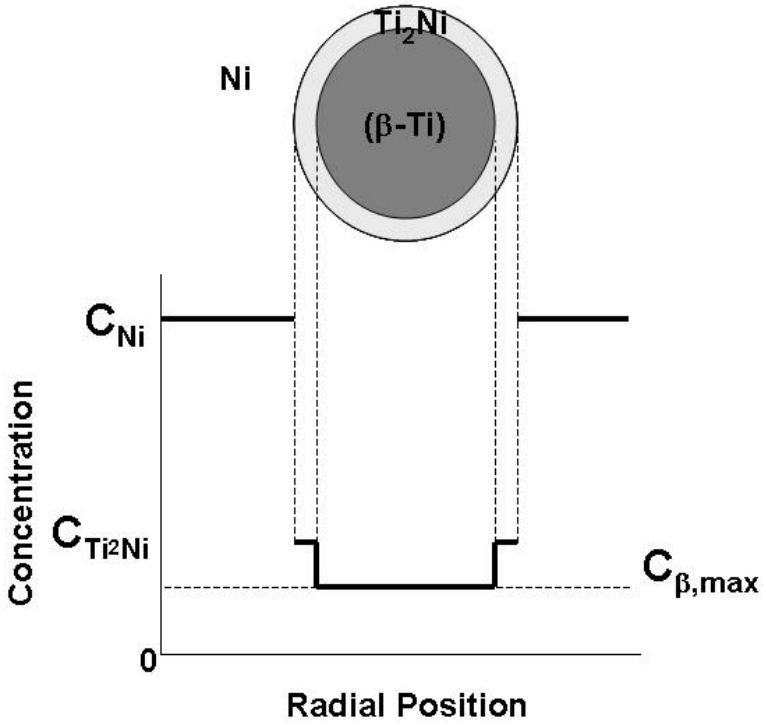

Figure 4-33: Schematic of β-Ti core surrounded by Ti_2Ni at 900 ^oC

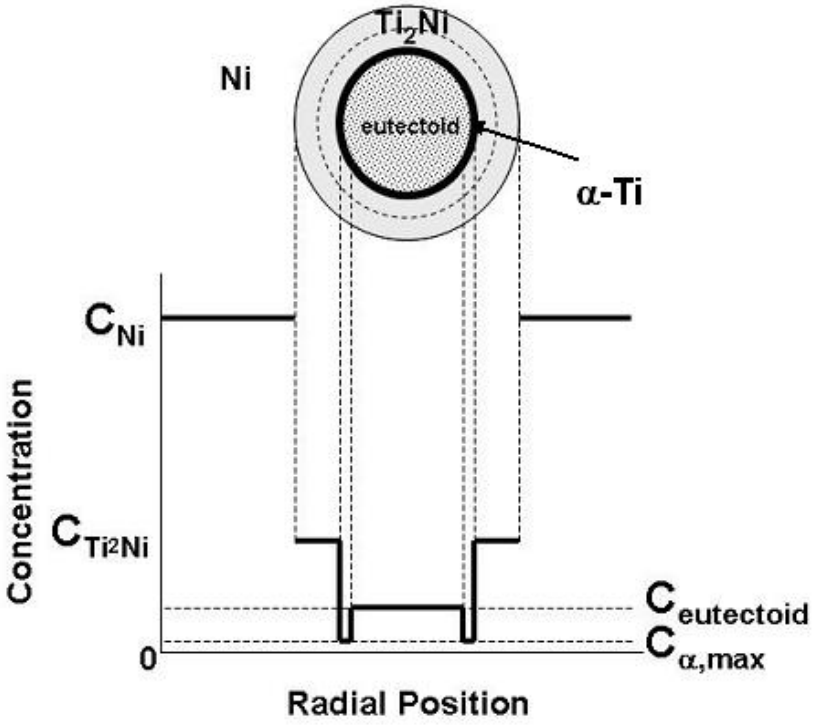

Figure 4-34: Schematic showing eutectoid core, α-Ti nucleation, and Ti_2Ni nucleation on existing Ti_2Ni/β-Ti interface (represented by dashed circle)

If it is assumed that all of the (β-Ti) available at 900°C is accounted for by the formation of Ti_2Ni and the eutectoid, then the following equation holds true:

$$f_{\beta-Ti} = f_{Ti_2Ni} + f_{eut} \tag{4-10}$$

Substitution of equation (4-9) into the above relationship yields:

$$\begin{aligned} \left[\frac{\left(X_{Ti_2Ni} - X_{eut}\right)}{\left(X_{Ti_2Ni} - X_{\beta-Ti}\right)}\right] f_{eut} &= f_{Ti_2Ni} + f_{eut} \\ f_{Ti_2Ni} &= \left[\frac{\left(X_{Ti_2Ni} - X_{eut}\right)}{\left(X_{Ti_2Ni} - X_{\beta-Ti}\right)} - 1\right] f_{eut} \end{aligned} \tag{4-11}$$

Substitution of Equation (4-8) into the rearranged expression for f_{Ti2Ni} yields:

$$f_{Ti_2Ni} = \left[\frac{\left(X_{\beta-Ti} - X_{eut}\right)}{\left(X_{Ti_2Ni} - X_{\beta-Ti}\right)}\right] \frac{\Delta H_{eut}}{\Delta H_f} \tag{4-12}$$

Where X_{Ti2Ni}, X_{eut} and ΔH_f are known quantities, the value $X_{\beta\text{-}Ti}$ is dependant on the peak sintering temperature from which cooling begins, and ΔH_{eut} is the measured enthalpy of the eutectoid reaction on the DSC.

With the development of Equations 4-10 through 4-12, it is now possible to determine the following: (i) the weight fraction of β-Ti within the microstructure at peak sintering temperature, (ii) the weight fraction of Ti_2Ni that grows immediately upon cooling from peak sintering temperature and (iii) the weight fraction of β-Ti that undergoes the eutectoid reaction. Conveniently, all of this information can be determined with only the enthalpy of the eutectoid reaction measured by the DSC during cooling. It should be

noted that the peak sintering temperature is not required to be 900°C for these calculations, as a different peak sintering temperature will just affect the quantity $X_{\beta\text{-}Ti}$ (as per the phase diagram) used in the calculation of weight fractions of β-Ti, Ti_2Ni and eutectoid.

From Figure 4-33 there appears to be a relationship between the hold time at peak temperature, and the prevalence of Ti_2Ni epitaxial growth immediately upon cooling. This trend would indicate that there is greater growth of this phase at low hold times, and that this growth immediately upon cooling decreases with an increase in sintering time at 900°C. From the lever rule, the fraction of Ti_2Ni growth immediately upon cooling is related to ΔH_{eut} through equation 4-12. Therefore, as ΔH_{eut} decreases with sintering time at 900°C, so too should ΔH_{Ti2Ni} (which is proportional to f_{Ti2Ni}). This can explain the decrease in the magnitude of the exothermic peaks observed immediately upon cooling in Figure 4-33.

4.7 Combustion Reaction during Heating (Heating Condition VI)

As discussed previously, the combustion reaction is initiated upon first liquid formation within the microstructure, which typically falls near the lowest eutectic temperature [8]. Observing the Ni-Ti phase diagram, the first instance of possible liquid formation can occur at a temperature of 942°C, which represents eutectic melting according to (4-2).

This melting event will initiate at the β-Ti/Ti_2Ni interface (Figure 4-36), and is clearly seen in the DSC traces of Figure 4-38, onsetting at 944°C. As previously described for

samples containing coarse Ti, the β-Ti core attains a uniform composition close to the maximum solubility while heating and holding at 900°C. Therefore it is expected that this phase would completely melt at or near the eutectic temperature leaving a pore (Figure 4-37).

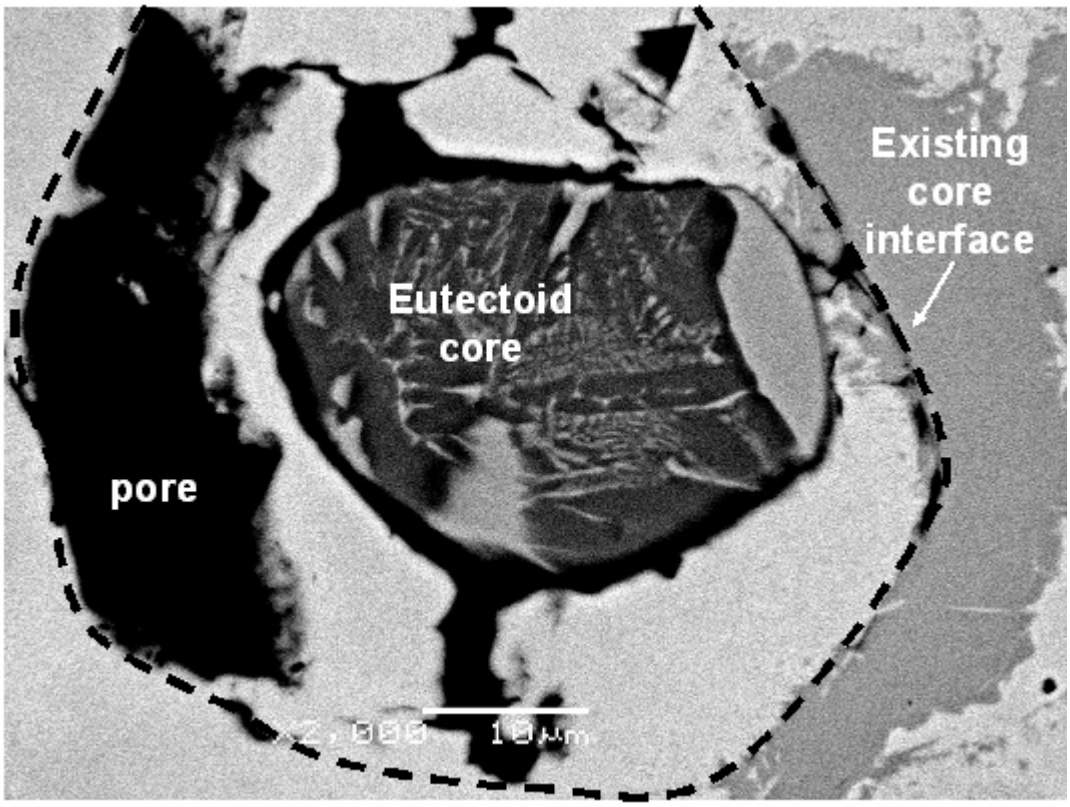

Figure 4-35: SEM backscatter image of interface melting between β-Ti and Ti_2Ni

Once this Ti-rich phase is produced it will rapidly spread throughout the powder compact by capillary action and come into contact with Ni rich regions of the sample. As the DSC trace indicates this ignites an exothermic reaction, with the subsequent formation of intermetallics including TiNi.

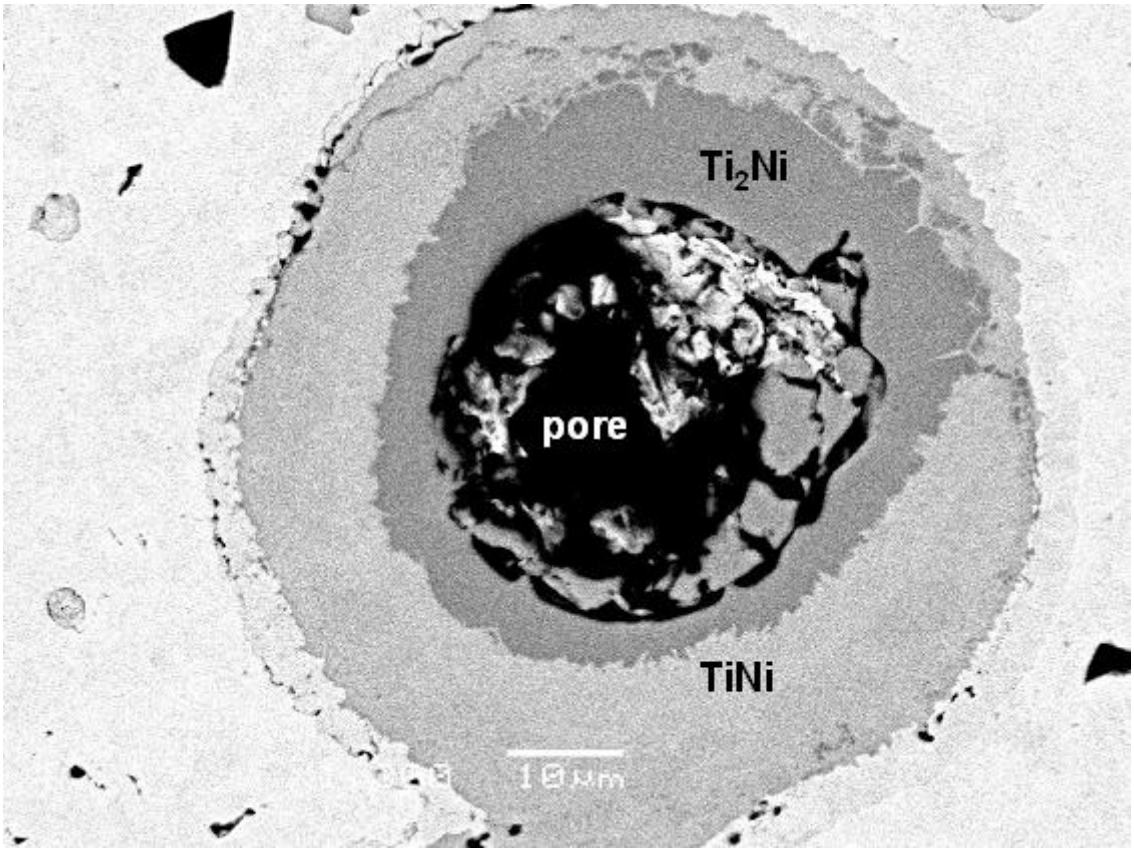

Figure 4-36: SEM backscatter image of a β-Ti core that has melted

Since the combustion reaction is initiated by melting at the β-Ti/Ti_2Ni interface, and the entire β-Ti core attains a uniform composition equal to the maximum solubility, the combustion reaction must therefore have a dependence on the β-Ti content of the microstructure. Studying the effects of β-Ti content on the combustion reaction was performed using heating profiles similar to those used to study the eutectoid reaction, the only difference being that the samples were further heated to 1020^{o}C to initiate the combustion reaction after any hold segment at 900^{o}C. Figure 4-38 shows the effects that imposing a hold segment at 900^{o}C has on the subsequent combustion reaction during heating to 1020^{o}C.

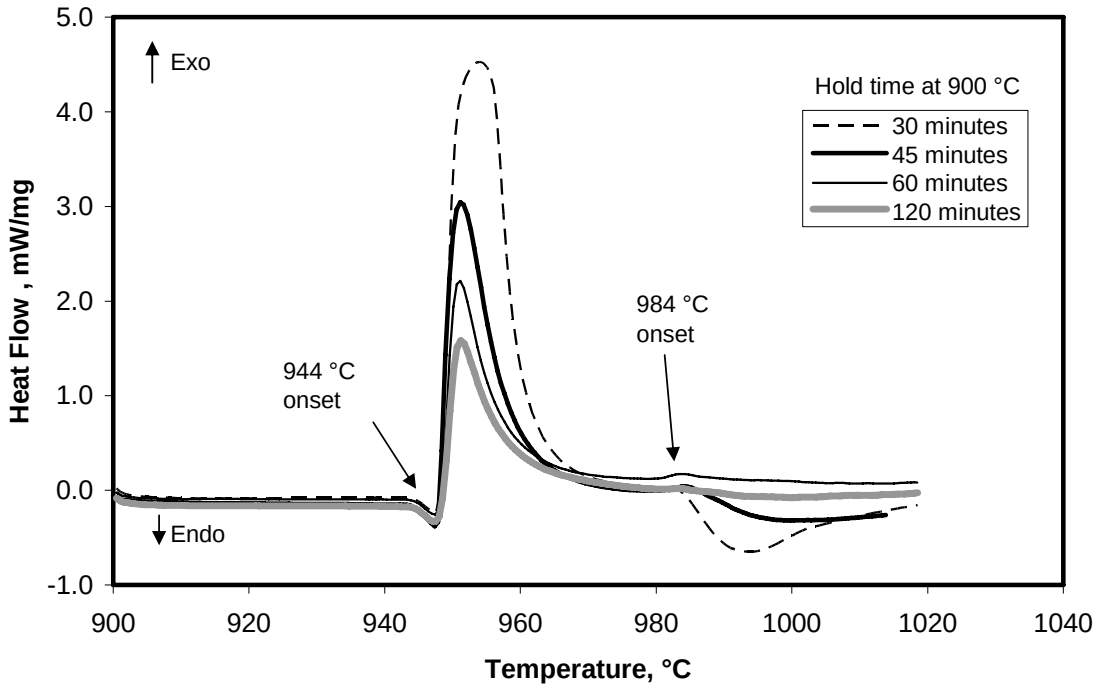

Figure 4-37: Observed exotherms due to combustion for coarse Ti samples heated to 900°C and held for varying time

Clearly there is an effect of hold time at 900°C, which appears to diminish the energy released by combustion with increased hold time. If the combustion reaction is indeed dependant on the β-Ti content of the microstructure, then this result makes sense, as increasing the hold time at 900°C effectively decreases the β-Ti content available to contribute towards combustion. Figure 4-39 plots the combustion energy (ΔH_{comb}) versus the weight fraction of β-Ti at 900°C, and regression of ΔH_{comb} versus $f_{\beta\text{-}Ti}$ indicates the relationship:

$$\Delta H_{comb} = 504.84\, f_{\beta - Ti} \qquad \textbf{[4-13]}$$

The $R^2 = 0.9775$ value for Eq. 4-13 indicates that the linearity of ΔH_{comb}, vs. $f_{\beta\text{-}Ti}$ is not as good as for ΔH_{eut}. This may be due to the compound nature of this peak. In particular the endothermic event of melting of the Ti-rich core is immediately followed by the

exothermic reaction. These two reactions are nearly simultaneous and their peaks will overlap on the DSC trace. As a further complication, the exothermic reaction causes the sample temperature to spike up above the ambient furnace temperature for a short time. According to the phase diagram this could cause additional melting of more Ni rich phases including Ti_2Ni and partial dissolution of TiNi. In addition, following the thermal spike the sample cools back to the ambient temperature and any phases that melted during the thermal spike may re-solidify. Consequently the large exotherm on the DSC trace may consist of a number of thermal events including initial melting of the Ti-rich core, exothermic reactions, additional melting as the sample temperature spikes and re-solidification upon cooling. Figure 4-39 clearly indicates that the sum of all these events, as measured under the area of the exothermic peak, is dependent on the weight fraction of the Ti –rich core of the sample developed at 900 °C in an approximately linear way.

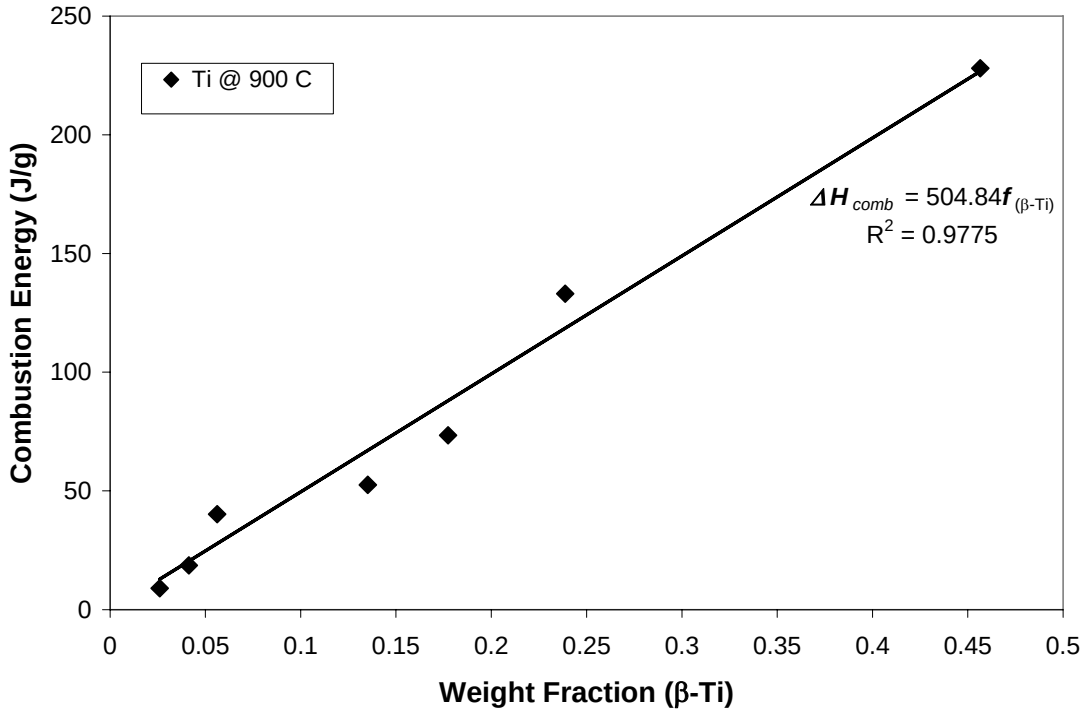

Figure 4-38: Plot of combustion energy (J/g) versus weigh fraction of β-Ti present at 900°C

If it is assumed that the rate at which β-Ti disappears from the microstructure at 900°C remains constant while heating to the ignition temperature of 944°C, then it is possible to correct Fig. 4-32 to account for the loss of β-Ti while heating from 900°C to 944°C. The rate of removal of β-Ti from the microstructure for hold times from 0 to 90 minutes is $k_I = -0.0347\ f_\beta / (mins)^{1/2}$ and that for 120 to 180 minutes is $k_{II} = -0.0123\ f_\beta / (mins)^{1/2}$. The amount of time to heat from 900°C to the ignition temperature of 944°C at a heating rate of 20 K/min is 2.2 minutes. Table 4-2 shows the results of multiplying the respective β-Ti removal rate by the square root of 2.2 minutes and adding it to the fraction of β-Ti at 900°C, while Fig. 4-40 compares these results showing the effect on the trendline equation obtained.

Table 4-2: Weight fraction of β-Ti at 900°C, and corrected to 944°C, after the given hold times at 900°C.

Time at 900 °C (min)	$f_{\beta\text{-}Ti}$ @900 °C	$f_{\beta\text{-}Ti}$ @944 °C
0	0.4566	0.4335
30	0.2388	0.2268
60	0.1774	0.1684
90	0.1352	0.1284
120	0.0562	0.0552
150	0.0413	0.0405
180	0.0260	0.0255

The linearity of ΔH_{comb}, vs. $f_{\beta\text{-}Ti}$ does not change as a result of this correction, but the slope of the regression equation does, where

$$\Delta H_{comb} = 531.74\, f_{\beta - Ti} \qquad \textbf{[4-15]}$$

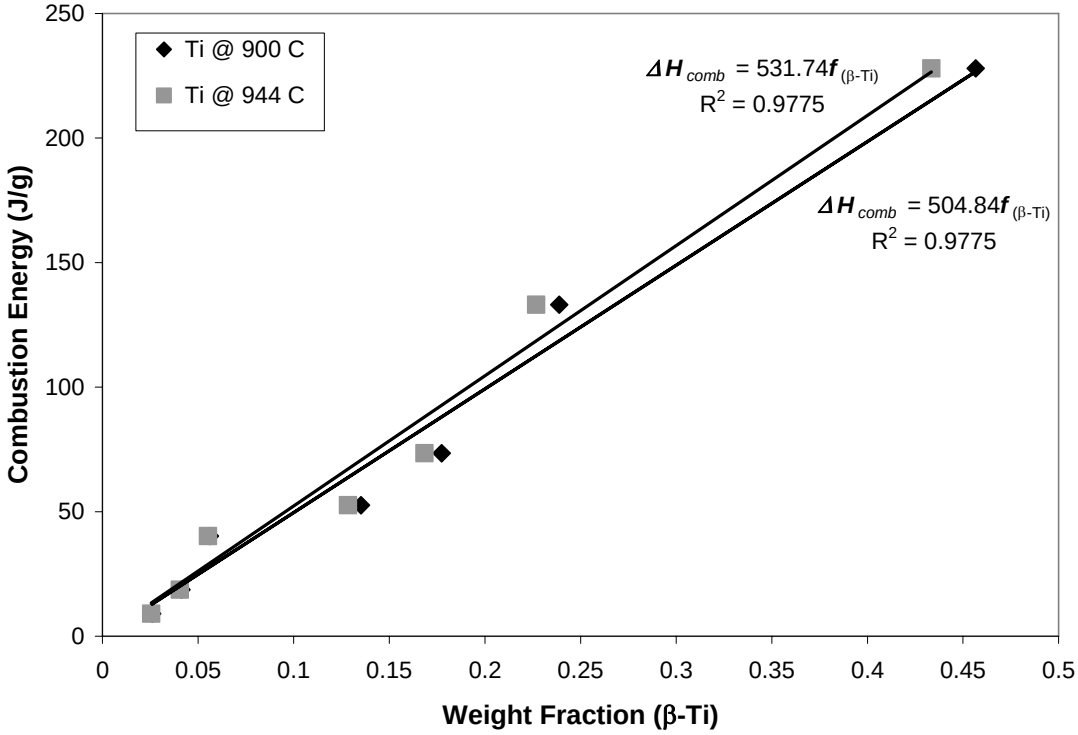

Figure 4-39: Compares corrected weight fraction of β-Ti at 944°C to that at 900°C

Since the β-Ti core attains a uniform composition quite readily, it can be assumed that the entire β-Ti core participates in the combustion reaction once initiated. This means that the corrected weight fractions of β-Ti can be considered the sample fraction undergoing combustion on a g Ti / g sample basis. The sample fraction undergoing combustion can also be determined by dividing the measured combustion exotherms by the theoretical energy value for combustion of ΔH_{comb} = 67 kJ/mol [69], or in terms of J / g Ti consumed, ΔH_{comb} = 1399 J / g Ti. Table 4-3 shows the results of this comparison. It can be seen that the values predicted for the fraction of sample undergoing combustion are significantly smaller when using the measured TE-SHS exotherms to calculate them (as shown by the percentage predicted column). In addition, Figure 4-41 shows that the error associated with using the TE-SHS exotherms to calculate the fraction of Ti that has

undergone combustion decreases with increased hold time at 900°C. This is a result of less Ti available to melt during to combustion, which results in a smaller melting endotherm opposing the observed combustion exotherm.

Table 4-3: Weight fractions of Ti undergoing combustion

$f_{(\beta\text{-Ti})}$ @ 944 °C (g Ti / g sample)	f_{comb} (g Ti / g sample)	% predicted by comb. Exo.
0.4335	0.1630	37.6
0.2268	0.0951	42.0
0.1684	0.0525	31.2
0.1284	0.0376	29.3
0.0534	0.0287	53.9
0.0392	0.0134	34.1
0.0247	0.0064	26.1

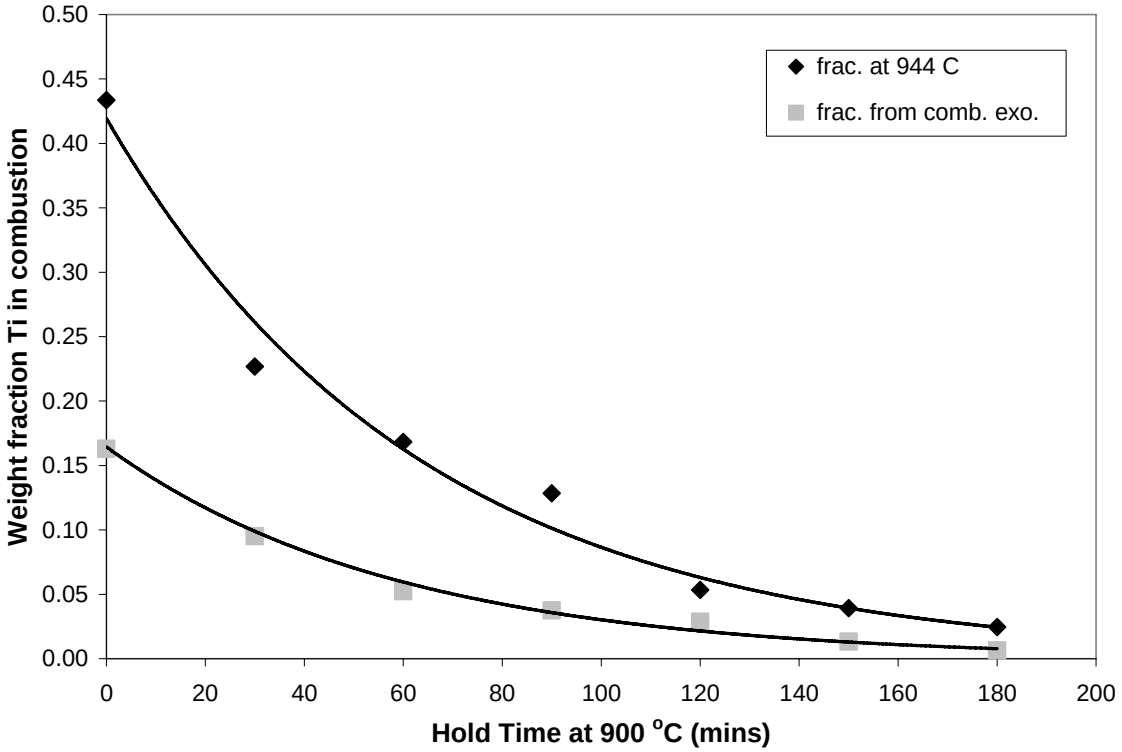

Figure 4-40: Differences between β-Ti weight fractions participating in combustion as predicted by Eq 4-9 corrected to 944 °C, and those predicted from the measured combustion exotherms

What this ultimately means is that only a percentage of the energy released as a result of the combustion reaction is observed on the DSC. As aforementioned, this is due to the

compound nature of the combustion event, which can include a number of melting events superimposed in the measured exotherm. Since melting is endothermic, such events will act to decrease the observed exotherm for combustion. Therefore, using the DSC to monitor the combustion reaction can be beneficial in determining qualitative relationships, but not quantitative ones.

Following the highly exothermic combustion reaction during heating to 1020^{o}C, when the temperature reaches 984^{o}C it is expected that any solid Ti_2Ni intermetallic present within the microstructure will melt. This is confirmed by a distinct endothermic peak occurring at 984°C on the DSC trace for some of the samples (see Fig. 4-38). Further heating up to 1020°C may cause some dissolution of the TiNi phase although no significant thermal event indicating this is visible on the DSC traces of Fig. 4-38.

The microstructure at the peak temperature of 1020°C is represented in Fig. 4-42b and consists of a solid network of (Ni), Ni_3Ti and TiNi with a Ti-rich liquid phase and large pores created by melting of the β-Ti core. Upon cooling the liquid phase will solidify. In the first stage one would expect solidification of a primary phase TiNi epitaxially growing from the TiNi solid surface due to cooling below the liquidus line (according to the Ni/Ti phase diagram). This is illustrated in Fig. 4-42c from the amount of solid TiNi pictured inside the dashed line. There is evidence for this solidification event from the exothermic peak immediately upon cooling in the DSC trace of Fig. 4-43. This peak is most notable for the sample held at 900°C for 60 minutes. According to the phase diagram further cooling will result in solidification according to the peritectic reaction of $TiNi + L \rightarrow Ti_2Ni$ at 984°C. A distinct exothermic peak at 984°C on the DSC trace

indicates that this solidification event does occur. The magnitude of the solidification clearly decreases with an increase in hold time at 900°C. This indicates that the reduction in the β-Ti phase at 900°C leads to less liquid formation and therefore less re-solidification from 1020°C.

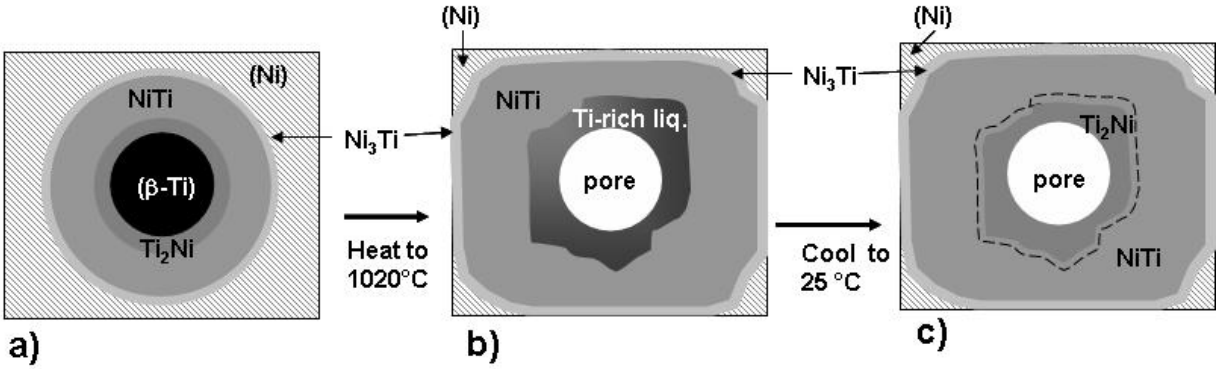

Figure 4-41: Schematic illustration of microstructure at: a) while holding at 900°C, b) after combustion upon heating to 1020°C, and c) after cooling to room temperature

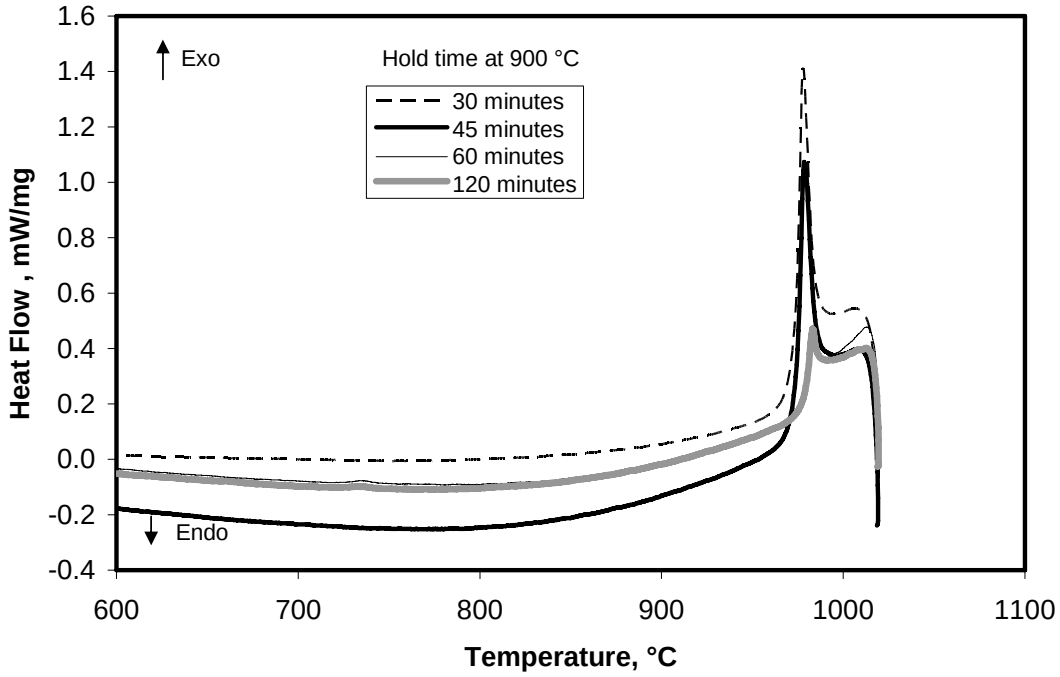

Figure 4-42: DSC cooling curves for combusted samples after heating to 1020 °C

Upon further cooling, any liquid remaining in the structure could solidify according to the eutectic reaction L → (β-Ti) + Ti_2Ni. With yet further cooling there is also the possibility of the eutectoid reaction occurring at 765°C. Neither of these reactions is detected on the DSC which indicates that no β-Ti remains in the sample after heating to the combustion temperature of 1020°C. This is consistent with the microstructural results of Fig. 4-44, where no α-Ti phase (which would have formed from the higher temperature β-Ti) was found at room temperature. Therefore, the microstructure present at room temperature after cooling from 1020°C is depicted in Fig. 4-42c. This consists of unreacted Ni solid solution, the three intermetallics and porosity.

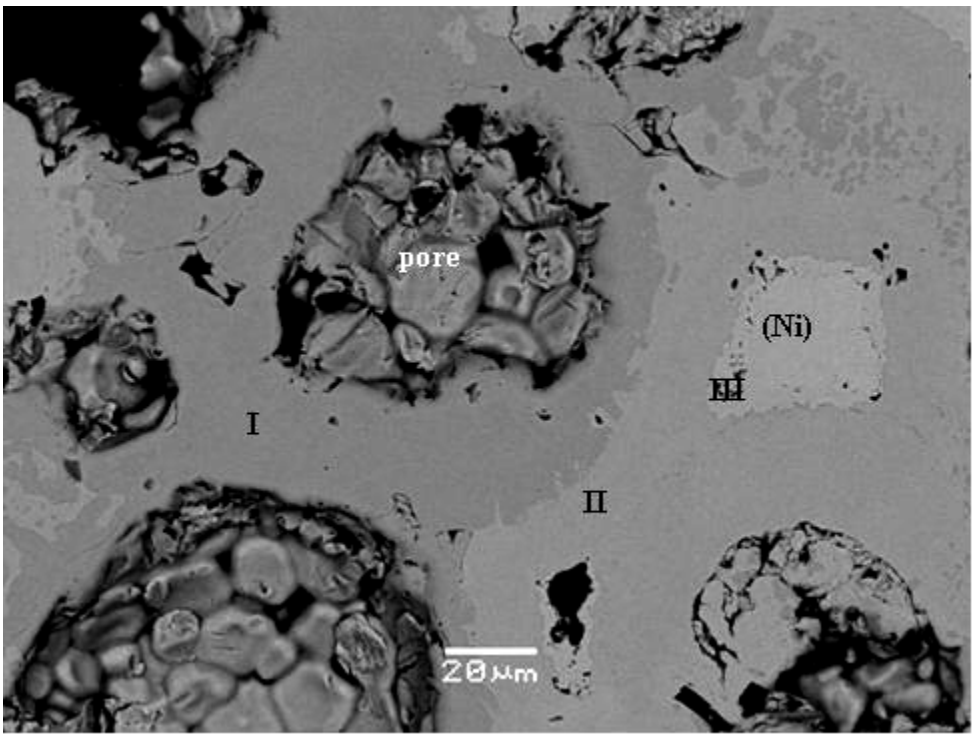

Figure 4-43: SEM backscatter image of a Ni-Ti compact sintered at 900 °C for 60 minutes, heated to 1020 °C and then cooled to room temperature. EDS analysis predicts that phase I, II, and III are Ti_2Ni, TiNi, and $TiNi_3$ respectively.

5 TiNi Formation and the Shape Memory Effect

The evidence thus far clearly demonstrates the effects of a hold time at 900°C. For example, as time at 900 °C increases the amount of β-Ti decreases. This is strongly supported by the DSC and microstructural evidence. The β-Ti content also directly determines the extent of the exothermic reaction taking place during the combustion stage at 1020°C. The micrographs of Figs. 3-16 and 3-17 indicate that an increased hold time at 900°C also increases intermetallic growth. Figure 3-20b also indicates that the combustion step at 1020°C increases intermetallic formation. Quantitative image analysis is unable to distinguish how much of this growth is TiNi due to the relatively low contrast between the three intermetallic phases and their more complex morphologies within the microstructure. However, the DSC can again be used to measure the shape memory transformation due to the presence of TiNi and therefore indicate its content in the microstructure.

As previously discussed in Chapter 1, the shape memory effect is most commonly characterized by the temperature at which martensite transforms to austenite during heating (i.e. A_s), the temperature at which austenite transforms to martensite during cooling (i.e. M_s) and the enthalpy of transformation, ΔH (i.e. the area under the transformation peak, divided by the heating or cooling rate, in J/g) [42, 54]. These measurements were made for a selection of samples after heat treatment at 900°C for various times followed by heating and cooling from 1020°C and for one sample heated to 900°C only, held for 180 minutes and then cooled. Two representative DSC traces are shown in Fig. 5-1. The transformation peaks during heating (martensite to austenite) and

cooling (austenite to martensite) are clearly visible. The transformation peaks during cooling show no evidence of a two-stage martensitic transformation (which would manifest itself as a double peak). This could indicate that either there is no R-phase transformation during cooling, or that the B2 → R-phase transformation is what is observed, and the R → B19' transformation occurs below room temperature (and is thus not observable without a low temperature DSC). The transformation enthalpy is significantly higher for a sample combusted after a 180 minute hold time at 900°C compared to a sample directly heated to 1020°C (i.e. 0 hold at 900°C). Figure 5-2 summarizes the enthalpy of transformation of martensite to austenite as a function of hold time at 900°C followed by combustion at 1020°C. This data confirms that increased hold time at 900°C does result in increased TiNi content. Figure 5-2 also includes a sample heated to 900°C and held for 180 minutes but not combusted. Comparison of this data with the equivalent sample heated to 1020°C indicates that combustion increases the TiNi content.

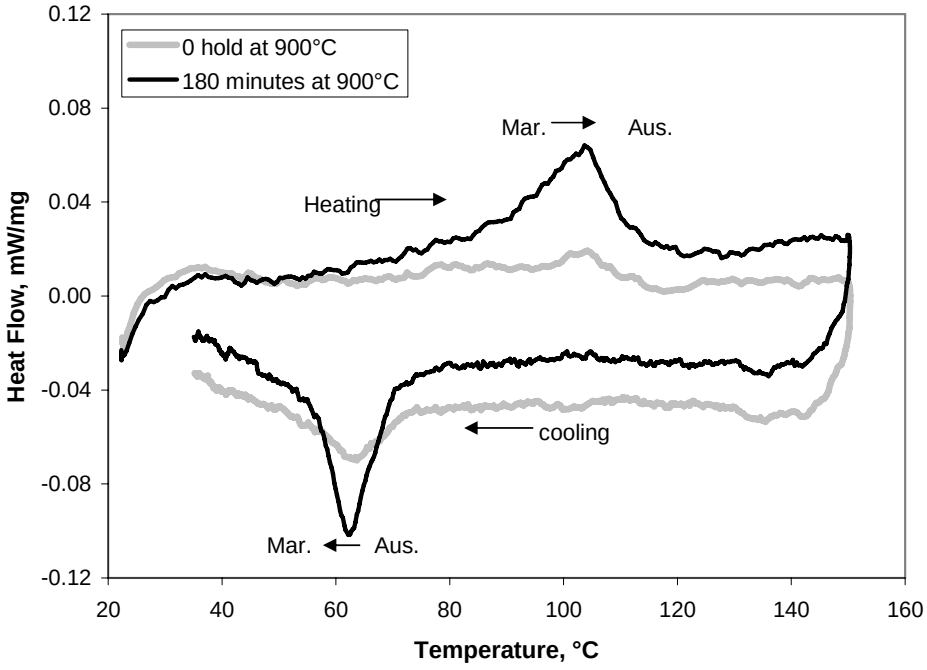

Figure 5-1: The shape memory transformation for two sintered and combusted TiNi samples

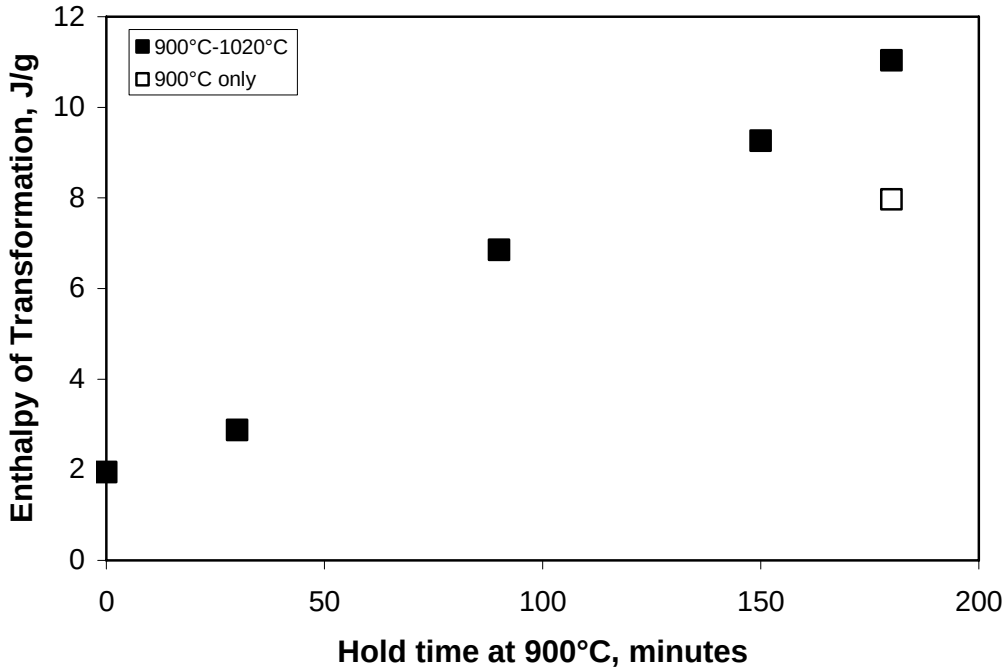

Figure 5-2: The shape memory enthalpy of transformation for martensite to austensite during heating, of TiNi samples as a function of hold time at 900°C

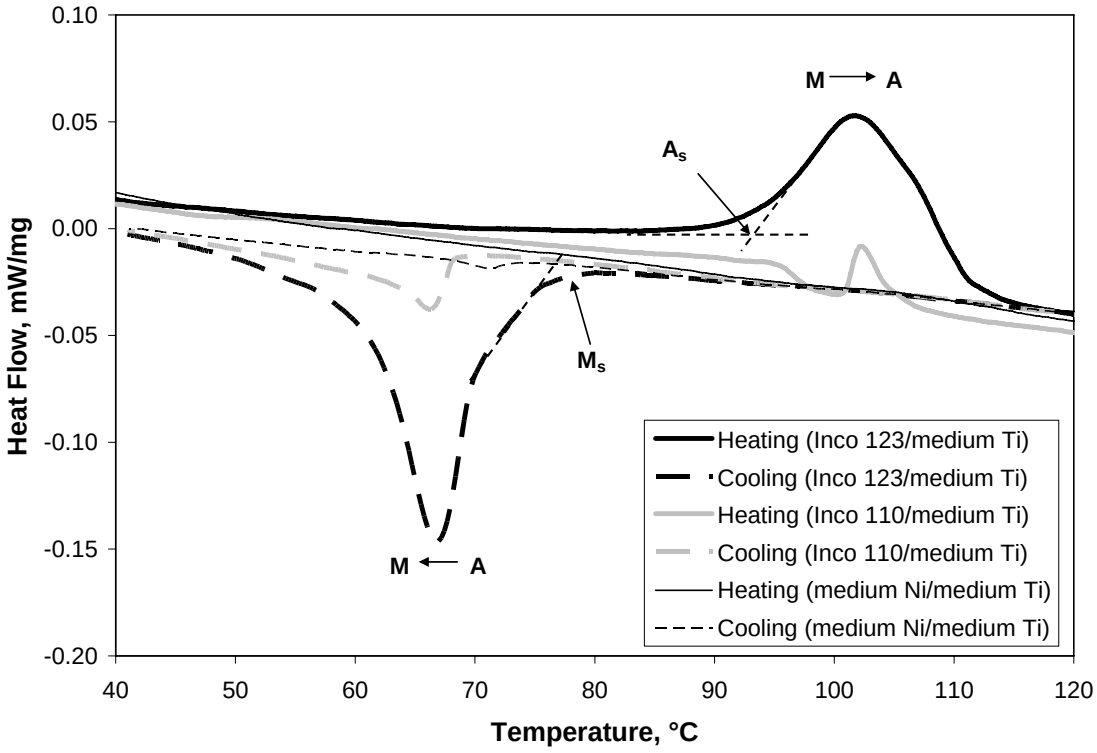

Figure 5-3: Shape memory effect for samples sintered at 950°C for 5 hours, consisting of differently sized Ni powder and medium Ti

Figure 5-3 shows the DSC heating and cooling curves obtained in studying the shape memory effect for samples consisting of differently sized Ni powders with medium (-325 mesh) Ti powder. These samples were sintered to a peak temperature of 950^{o}C and held for 5 hours. This figure shows a clear effect of powder size on both TiNi formation during sintering, and the subsequent SME displayed after sintering. The sample consisting of Inconel 123 Ni powder displays the largest SME, with the Inconel 110 Ni sample displaying a smaller, yet still apparent, SME. The sample sintered with -325 mesh Ni shows little evidence of a shape memory effect, but this does not mean that there is no TiNi present within the microstructure of this sample. This could just mean that the bulk of the TiNi phase in the -325 mesh Ni sample could have a composition such that a majority of it is present as austenite at room temperature.

This compositional effect of the SME (and on the formation of martensite during cooling) can be further understood from the sample of Figure 5-4, which shows a transition zone (dashed white curve) in which the martensite variants of the TiNi phase diminish, as the microstructure changes from predominantly martensitic TiNi to predominantly austenitic TiNi. SEM-EDS analysis of the microstructure in Figure 5-4 indicates that the Ni concentration ranges from approximately 51.5 at% in the austenite (left side) to 50.5 at% in the martensite (right side).

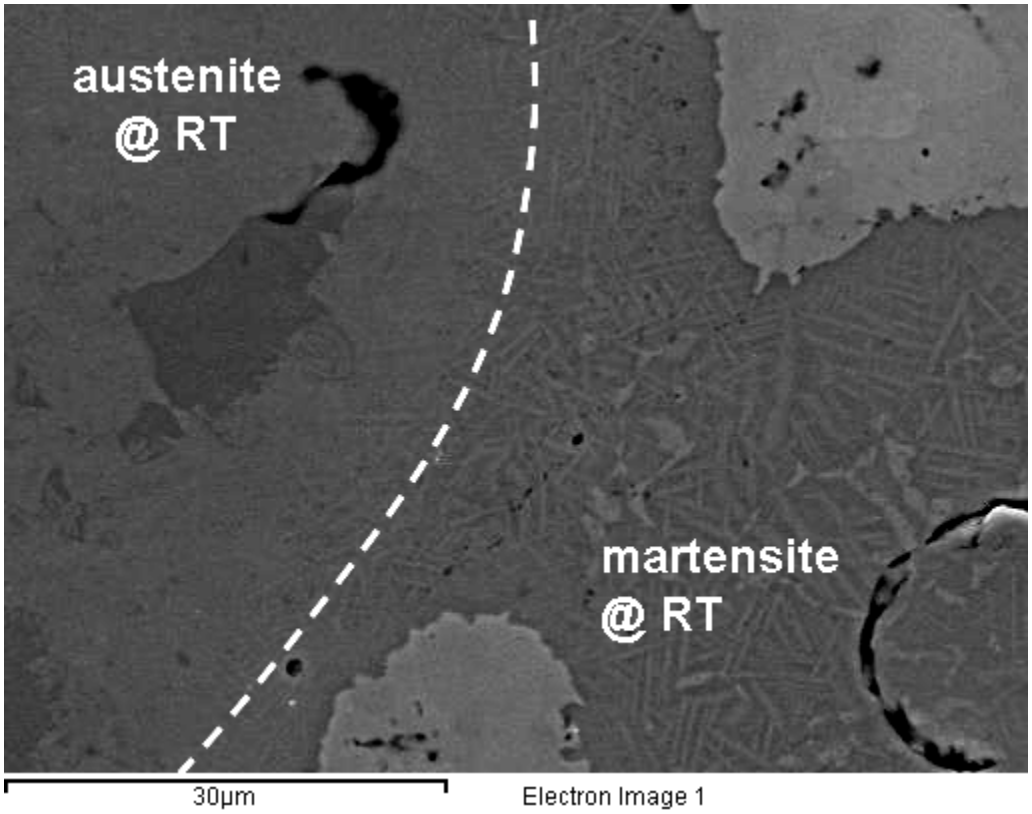

Figure 5-4: SEM backscatter image highlighting the transition from martensite to austenite as a result of compositional variations within the TiNi phase

6 Conclusions

As previously discussed, a primary purpose of the present work was to develop an experimental technique using Differential Scanning Calorimetry (DSC) capable of elucidating phase formation during sintering of a Ni and Ti powder compact in order to increase the understanding of the sintering mechanisms that take place during solid state and reactive sintering.

With aid of the DSC, qualitative relationships between powder size and phase (intermetallic) formation during sintering to elevated temperatures were deduced. As shown in Chapter 1, the formation of intermetallics is exothermic by nature. Thus, the formation of these intermetallics was observed on the DSC as *weak* exothermic reactions, and not sharp peaks (which would be indicative of chemical reactions or a change of state). This indicates that Ti_2Ni, TiNi and $TiNi_3$ can form by slow diffusion-controlled growth during heating up to 950^oC. These weak exothermic reactions were observed to occur to a greater extent with finer powders. It can be concluded that a mixture containing finer powders results in a greater degree of intermetallic formation. This makes sense, as finer powders possess a larger surface area (for a given mass of powder) to promote solid state reactions.

In addition to intermetallic formation, the highly exothermic combustion reaction was observed on the DSC, which is a chemical reaction between Ni and Ti. As a chemical reaction, it should appear on the DSC as a relatively sharp peak, which was the case.

This reaction was found to be sensitive to particle size of the constituent powders, the finer of which could be used to suppress this reaction.

The ignition temperature for the combustion reaction was found to occur between 942^{o}C and 984^{o}C, depending on the powder sizes used. For the case where coarse Ni and medium Ti powder were used, the ignition temperature tended to the higher end of the range, with onsets close, or equal to, 984^{o}C (ie. the melting point of Ti_2Ni). When coarse Ti and fine Ni were used, the onset temperature for this reaction occurred at 942^{o}C, which represents the temperature at which incipient melting can occur between β-Ti and Ti_2Ni. Further study is required to determine the reason for the dependence of the ignition temperature on the constituent powder sizes.

In studying the eutectoid decomposition of β-Ti on the DSC, a simple model was developed to relate the measured enthalpy of this reaction to the area fraction observed microstructurally (4-7). This allowed for the determination of the standard enthalpy for the β-Ti eutectoid decomposition, which was found to be ΔH_f = 64.8 J/g. This value, coupled with the measured eutectoid enthalpy, allowed for the determination of the weight fraction of β-Ti present as a function of hold time at 900^{o}C. It was found that the β-Ti removal followed a two stage parabolic decay. The rate constant for stage I was found to be $k_I = -0.0347\ f_\beta / (mins)^{1/2}$ and that for stage II, $k_{II} = -0.0123\ f_\beta / (mins)^{1/2}$.

With the weight fraction of β-Ti known as a function of hold time, it also became possible to determine the weight fraction of Ti_2Ni phase that grew upon cooling from a

peak temperature of 900°C. Using qualitative DSC results, it was shown that the amount of Ti_2Ni growth decreased with increasing hold time at 900°C. This was attributed to a decrease in the β-Ti/Ti_2Ni interfacial area with hold time, which is the site for Ti_2Ni nucleation during cooling.

Since it is presupposed that the combustion reaction is initiated by the melting of a Ti-rich eutectic phase, the effect of Ti content on this reaction was studied. This presupposition was validated when melting at 944°C was observed on the DSC, which immediately initiated the highly exothermic combustion reaction. A relationship between the enthalpy observed for the combustion reaction versus the fraction of β-Ti present at the time of combustion was developed (Eq. 4-15). This represents the first published evidence that combustion actually depends on the β-Ti content, which in turn precipitates a melting event significant enough to initiate combustion. If β-Ti is removed prior to heating to ~ 950°C (either by a low temperature heat treatment or the use of fine powders), then the combustion reaction can be prevented.

It was found that only a percentage of the energy released as a result of the combustion reaction was observed by the DSC due to the compound nature of the combustion event, which can include a number of melting events superimposed in the measured exotherm. Since melting is endothermic, such events act to decrease the observed exotherm for combustion. As previously concluded, the use of DSC to monitor the combustion reaction can be beneficial in determining qualitative relationships, but not quantitative ones.

In studying the shape memory effect using the DSC, it was found that the prevalence of the SME displayed increased with an increased hold time at 900^{o}C for the coarse Ti samples. This was attributed to increased TiNi phase formation with increased sintering time at 900^{o}C. Figure 5-2 also indicates that the combustion reaction improves the SME observed for the coarse Ti samples, when compared with a sample of similar sintering profile that had not been through combustion. Ni powder size was also shown to have an effect on the SME, with a stronger effect being displayed by samples sintered with finer Ni powders. This can be attributed to increased TiNi formation as a result of faster kinetics for finer constituent powders.

References

[1] T.B. Massalski. *Binary Alloy Phase Diagrams*, Am Soc Metals, Metals Park, OH, 1986.
[2] Oulu University - http://herkules.oulu.fi/isbn9514252217/html/x317.html
[3] S. Saito, T. Wachi, S. Hanada. *Materials Science and Engineering*, 1993, **A161**, 91.
[4] Y. Furuya, A. Sasaki, M. Taya. *Materials Transactions: Japan Institute of Metals*, 1993, **34**, 224.
[5] M. Taya, Y. Furuya, Y. Yamamda, R. Watanabe, S. Shibata, T. Mori. *Society of Photographic Instrumentation Engineers*, 1993, **1916**, 373.
[6] F.E. Wang, W.J. Buehler, and S.J. Pickart. *Journal of Applied Physics*, 1965, **36**, 3232.
[7] Alfa Aesar: Research Chemicals, Metals and Materials, www.alfa.com.
[8] R.M. German, "*Sintering Theory and Practice*", John Wiley & Sons, Inc., Toronto, 1996
[9] K.S. Suslick, *The Chemistry of Ultrasound*, The Yearbook of Science & the Future 1994, Encyclopaedia Britannica. Chicago, 1994; 138. (http://www.scs.uiuc.edu/suslick/britannica.html)
[10] C. Herring. *Journal of Applied Physics*, 1950, **21**, 301.
[11] R.M. German. *Metallurgical Transactions*, 1992, **23A**, 1455.
[12] R.M. German, M. Bulger. *International Journal of Powder Metallurgy*, 1992, **28**, 301.
[13] A.P. Savitskii, "*Liquid Phase Sintering of Systems with Interacting Components*", Russian Academy of Sciences, Tomsk, Russia, 1993.
[14] D.A. Porter, K.E. Easterling, *Phase Transformations in Metals and Alloys: 2nd Edition*, Chapman & Hall USA, New York, NY, (1992).
[15] D.J. Lee, R.M. German, *International Journal of Powder Metallurgy and Powder Technology*, 1985, **28**, 131.
[16] G.F. Bastin,G.D. Rieck, *Metallurgical Transactions*, 1974, **5**, 1827.
[17] Z.A. Munir, *Ceramics Bulletin*, 1988, **67**, 342.
[18] R.L. Coble, "Reactive Sintering," *Sintering: Theory and Practice*, D. Kolar, S. Pejovnik, and M.M. Ristic (eds.), Elsevier Scientific, Amsterdam, 1982, 145.
[19] A. Bose, B.H. Rabin, and R.M. German. *Powder Metallurgy International*, 1988, **20/3**, 25.
[20] Z.A. Munir. *Metallurgical Transactions*, 1992, **23A**, 7.
[21] Z.A. Munir, J.B. Holt. *Combustion and Plasma Synthesis of High-Temperature Materials*, VCH, New York, 1990.
[22] W.L Frankhouser, K.W. Brendley, M.C. Kieszek, and S.T. Sullivan. *Gasless Combustion Synthesis of Refractory Compounds*, Noyes, Park Ridge, NJ, 1985.
[23] L.A. Wenning, J.P. Lebrat, and A. Varma. *Journal of Materials Synthesis Processes*, 1994, **2**, 125.
[24] S.C. Deevi. *Materials Science and Engineering*, 1992, **A149**, 241.
[25] V.I. Itin, Y.S. Naiborodenko, A.D. Bratchikov, N.P. Butkevich, S.V. Korostelev, and L.V. Sholokhova. *Russian Physics Journal*, 1975, **3**, 133.

[26] V.I. Itin, V.N. Khachin, A.D. Bratchikov, V.E. Gyunter, E.F. Dudarev, T.V. Monasevich, D.B. Chernov, G.D. Timonin, and A.P. Paperskii. *Soviet Physics Journal*, 1977, **12**, 117.
[27] A.D. Bratchikov, A.G. Merzhanov, V.I. Itin, V.N. Khachin, E.F. Dudarev, V.E. Gyunter, V.M. Maslov, and D.B. Chernov. *Soviet Powder Metallurgy and Metal Ceramics*, 1980, **19/1**, 5.
[28] V.I. Itin, A.D. Bratchikov, A.G. Merzhanov, and V.M. Maslov. *Combustion, Explosion, and Shock Waves*, 1981, **17/3**, 293.
[29] I.F Martynova, V.Y. Petrishchev, and V.V. Skorokhod. *Soviet Powder Metallurgy and Metal Ceramics*, 1983, **22/11**, 895.
[30] G.I. Aksenov, I.A. Drozdov, D.B.Chernov, A.A. Uvarov, and Y.A. Atyakshev. *Soviet Powder Metallurgy and Metal Ceramics*, 1983, **22/12**, 997.
[31] I.F Martynova, V.Y. Petrishchev, and V.V. Skorokhod. *Soviet Powder Metallurgy and Metal Ceramics*, 1983, **22/12**, 979.
[32] M. Igharo, J.V. Wood. *Powder Metallurgy*, 1985, **28/3**, 131.
[33] M. Igharo, J.V. Wood. *Powder Metallurgy*, 1986, **29/1**, 37.
[34] D.G. Morris, M.A. Morris. *Materials Science and Engineering*, 1989, **A110**, 139.
[35] N. Zhang, P.B. Khosrovabadi, J.H. Lindenhovius, and B.H. Kolster. *Materials Science and Engineering*, 1992, **A150**, 263.
[36] J.C. Hey, A.P. Jardine. *Materials Science and Engineering*, 1994, **A188**, 291.
[37] S.M. Green, D.M. Grant, and N.R. Kelly. *Powder Metallurgy*, 1997, **40/1**, 43.
[38] M.D. McNeese, D.C. Lagoudas, and T.C Pollock. *Materials Science and Engineering*, 2000, **A280**, 334.
[39] M. Bram, A. Ahmad-Khanlou, A. Heckmann, B. Fuchs, H.P. Buchkremer, D. Stöver. *Materials Science and Engineering*, 2002, **A337**, 254.
[40] E. Schüller, O.A. Hamed, M. Bram, D. Sebold, H.P. Bechkremer, and D. Stöver. *Advanced Engineering Materials*, 2003, **5/12,** 918.
[41] A.M. Locci, R. Orru, G. Cao, Z.A. Munir. *Intermetallics*, 2003, **11**, 555.
[42] G.K. Dey. *Acta Materialia*, 2003, **51**, 2549.
[43] B.Y. Li, L.J. Rong, Y.Y. Li, and V.E. Gjunter. *Acta Materialia*, 2000, **48**, 3895.
[44] B.Y. Li, L.J. Rong, Y.Y. Li, and V.E. Gjunter. *Intermetallics*, 2000, **8**, 881.
[45] Y. Li, L.J. Rong, Y.Y. Li. *Journal of Alloys and Compounds*, 2001, **325**, 259.
[46] S.L. Zhu, X.J. Yang, F. Hu, S.H. Deng, Z.D. Cui. *Materials Letters*, 2004, **58**, 2369.
[47] A. Biswas. *Acta Materialia*, 2005, **53**, 1415.
[48] E. Schüller, L. Krone, M. Bram, H.P. Buchkremer, D. Stöver. *Journal of Materials Science*, 2005, **40**, 4231.
[49] J.E. Garay, U. Anselmi-Tamburini, Z.A. Munir. *Acta Materialia*, 2003, **51**, 4487.
[50] B. Bertheville, J.E. Bidaux. *Journal of Alloys and Compounds*, 2005, **387**, 211.
[51] B. Bertheville, J.E. Bidaux. *Scripta Metallurgica*, 2005, **52**, 507.
[52] Y. Suzuki and H. Unuma, Method for the preparation of an alloy of nickel and titanium, US Patent 4,719,077 (1988).
[53] H.C. Yi, J.J. Moore. *Scripta Metallurgica*, 1988, **22/12**, 1889.
[54] S.H. Lee, J.H. Lee, Y.H. Lee, D.H. Shin and Y.S. Kim. *Materials Science and Engineering*, 2000, **A281**, 275.
[55] C.L. Yeh, W.Y. Sung. *Journal of Alloys and Compounds*, 2004, **376**, 79.
[56] B. Li., L. Rong and Yi. Li. *Journal of Materials Results*, 1998, **13/10**, 2847.
[57] B. Li., L. Rong and Yi. Li. *Materials Science and Engineering*, 1998, **A255**, 70.

[58] http://www.incosp.com/products/
[59] J.A. McGurty, Austenitic iron alloys having yttrium, US Patent 4,385,934 (1983).
[60] C. Zanotti. *Intermetallics* , 2007, **15**, 404-412.
[61] Instrument Manual for Netzsch Thermal Analysis Software, Netzsch Group, Germany.
[62] E.A. Brandes, G.B. Brook. *Smithells Metals Reference Book, Table 8-10*. Elsevier Butterworth-Heinemann. Massachusettes, 1998, 841.
[63] Serway, Raymond A., and Robert J. Beichner. *Physics: For Scientists and Engineers with Modern Physics (5th Edition)*, Table 30.3: Curie Temperatures for Several Ferromagnetic Substances. Saunders College Publishing. New York, 2000, 936.
[64] Grew, K.E. *Proceedings of the Royal Society of London. Series A, Containing Papers of a Mathematical and Physical Character*, Vol. 145, No. 855. (Jul. 2, 1934), pp. 509.
[65] J.L. Murray, "The Ni-Ti (Nickel-Titanium) System", *Phase Diagrams of Binary Titanium Alloys*, ASM International, Metals Park, OH, © 1987.
[66] G.F. Basten, G.D. Rieck, *Metallurgical Transactions*, 1974, **5**, 1827.
[67] P.G. Wahlbeck, P.W. Gilles. *Journal of the Ceramic Society*, 1966, **49**/**4**, 180.
[68] Y.A. Shevchuk, *Inorganic Materials*, 2004, **4**, 445.
[69] Li BY, Rong LJ, Li YY, Gjunter VE, Li YY. *Z Metallkd*, 2000, **91**, 291.